Study on Impacts of Geomagnetic Disturbances on Power Systems

ZHANG TIAN

Study on Impacts of Geomagnetic Disturbances on Power Systems

ZHANG TIAN

Supervisor: Prof. Yusuke Ebihara

Department of Electrical Engineering

Kyoto University

This dissertation is submitted for the degree of

Doctor of Philosophy

August 2024

Declaration

I hereby declare that except where specific reference is made to the work of others, the contents of this dissertation are original and have not been submitted in whole or in part for consideration for any other degree or qualification in this, or any other University. This dissertation is the result of my own work and includes nothing which is the outcome of work done in collaboration, except where specifically indicated in the text. This dissertation contains about 31,000 words including appendices, bibliography, footnotes, tables and equations and has less than 40 figures.

ZHANG TIAN

August 2024

Acknowledgements

I sincerely thank my advisor, Professor Yusuke Ebihara, for his meticulous care and guidance over the past four years. I have learned a lot of valuable knowledge and experience from my admired sensei, whether in scientific fields or in my life. Until the final stage of writing my doctoral thesis, sensei is still leading my way and gave me a lot of constructive suggestions and comments. Thank you for your selfless dedication, which made me carry on my persistent pursuit of academics. Sensei's kindness will never be forgotten in my heart!

Of course, I also thank Prof. Omura, Prof. Matsuo, Prof. Kojima, and all the Professors in space group for their assistance in my study. Moreover, the old boys and girls in the group, Dr. Yikai Hsieh, and Dr. Bo Yang, I really appreciate that they offer me selfless help in my study and life from the first day, which makes me adapt to studying abroad. And many thanks to the researchers and students from the lab I belong to (Ebihara's lab), including Megha Pandya, Yuta Mizuno-kun, Yukito Taniguchi-kun, Kotono Kaneda-san and so on, we enjoyed a great time of playing and studying together!

Finally, I need to thank my beloved parents the most. Thank you for the most selfless love and the endless support. As a saying goes, companionship is the longest confession. Although your love for me is silent sometimes, it has penetrated deep into every piece of the land I have walked on in the world. This earth will eventually bloom enviable flowers along the way in return!

Above, I am grateful to all the people and things that deserve thanks. Thank you very much!

Abstract

This study is started from the analysis of geomagnetic/geoelectric field data measured at a geomagnetic observatory (Kakioka Observatory) in Japan to acquire a quantitative relationship between them for different types of geomagnetic disturbance (GMD) events, whose purpose is to establish a fast way of calculating the geomagnetically induced currents (GICs) induced correspondingly in Japanese power grids. First, the geomagnetically induced electric field (GIE) near Kakioka station is estimated according to our regression equations by examining the corresponding observed geoelectric field variations for 213 sudden commencements (SCs), 36 magnetic storms and 325 bay disturbances; then the GICs flowing in three power substations around the observatory are calculated by using the empirical model in the previous study for a certain power network (topology and parameters) based on the estimated GIEs. The underlying maximum GICs for extreme GMD events are also predicted through the generalized extreme value distribution (GEVD) method, which is useful for evaluating the possible GIC risks against extreme GMD events and forecasting the maximum GICs in a real-time manner.

The sudden commencement (SC) events and magnetic storms (main phase) are proved almost equally important for large-amplitude disturbances of geoelectric field at low-latitude. The geomagnetic response associated with SCs at high latitudes is investigated further with great interest that the known Québec blackout just took4 place during a SC event at night. SCs are impulse responses of the magnetosphere–ionosphere system caused by a sudden change in solar wind dynamic pressure. To understand the correspondence, global MHD simulations with different solar wind conditions (jumps of solar wind velocity and density employed) are performed to get the nighttime geomagnetic response, and the results are compared with the observed geomagnetic data provided by 12 magnetic observatories in Canada and IMAGE magnetometer network. Contributions from FACs, ionospheric Hall and Pedersen currents to the geomagnetic disturbances at different locations on the ground are calculated by Biot-Savart's law. The results identify that the ionospheric Hall current during main impulse (MI)

phase of the SC is the principal contributor that presumably resulted in the known Québec blackout in 1989. It reminds us of the attention should be paid to SC events as well when handling the GIC issues in power systems. This study also helps to establish a global map of geomagnetic response to both FACs and ionospheric currents, which is favorable to the prediction of GICs in the power system combined with the information of ground conductivity structure and power network topology.

According to the previous result, large geomagnetic disturbances do take place during SCs. The disturbances are closely related with the FAC system associated with SCs, and thus it is needed to understand firstly the generation of the FACs during preliminary impulse (PI) and main impulse (MI) phases of SCs. A newly developed method of tracing an Alfvén wave packet is applied in the global MHD simulation to collect the generation information of FACs. New criteria of identifying the generation of FACs are also employed. These help to make clear the generation and mechanism of SC-associated FACs. The results show that FACs during two phases (PI and MI) of SCs are generated in different regions and associated with different motions of plasma affected by Lorentz force (magnetic pressure force and magnetic tension force). The polarity of PI FACs is determined by vorticity of plasma flow, and that of MI FACs is determined by the dot product of current density and velocity. This study provides a deep understanding of the geomagnetic response to solar activities that may give rise to the solar wind dynamic pressure jumps, like coronal mass ejections (CMEs), which explains why power systems in high-latitude regions are more susceptible to GIC harm due to GMDs associated with the FAC system.

Contents

List of Figures

List of Tables

Acronyms

CME	coronal mass ejection
FAC	field-aligned current
GEVD	generalized extreme value distribution
GIC	geomagnetically induced current
GIE	geomagnetically induce electric field
GMD	geomagnetic disturbance
IMF	interplanetary magnetic field
MHD	magnetohydrodynamic
MI	main pulse
MLAT	magnetic latitude
MLT	magnetic local time
PI	preliminary impulse
SC	sudden commencement
SI	sudden impulse
SSC	storm sudden commencement

Chapter 1 Introduction

1.1 Background

Geomagnetically induced currents (GICs) are regarded as the direct result of geomagnetic disturbance (GMD) effects on power networks, especially on neutral-grounded transformers. The geomagnetic disturbance is caused by current systems flowing in the magnetosphere and the ionosphere. The changes in the Earth's magnetic field induce currents, namely GICs, flowing in grounded conductors according to Faraday's law. Of course, the origin of these changes is the Sun, more specifically, is the solar wind (the continuous super-sonic flow of charged particles from the Sun), interacting with the magnetosphere of the Earth. Major GMD events are usually caused by coronal mass ejections (CMEs), which are eruptions of solar wind with large clouds of plasma and magnetic field from the Sun's corona.

GIC problems in power grids (e.g., half-cycle saturation of transformers, increase of harmonics, reactive power fluctuations, overheating and noise) are well studied during last decades since the largest magnetic storm caused world-widespread impacts on power systems in 1989, including the known Québec blackout in Canada. Further discussions from the engineering side are concentrated on monitoring and modelling GICs in power networks (as well as in other long-length conductors), the mitigation method of GIC risks, and the ground conductivity models in magnetotelluric (MT) community.

More efforts are made to understand the physics behind the phenomenon, that is, what is the key point for generating strong GMDs and resultant large-amplitude GICs from the view of solar and space physics. As is known that the geomagnetic disturbances are dominated by varied magnetospheric and/or ionospheric currents. Each specific space current and corresponding geomagnetic response are differently influenced by solar wind conditions. The geomagnetic response and the correspondence could be calculated and investigated through global magnetohydrodynamic (MHD) simulations. Geomagnetic observations are used to verify the simulation result for a particular GMD event.

1.2 Solar Wind and Space Weather

The universe space is probably the emptiest environment compared to the vacuum created by any laboratory on the Earth. However, it is not entirely devoid of matter. The space is filled with particles, fields, and plasma that are continuously blown out from the Sun, which is called solar wind. This solar wind as shown in Figure 1.1, and sometimes solar activities cause huge explosions. The significant ejection is called coronal mass ejections (CMEs), which influences the interplanetary space, and interacts with the magnetic systems of the Earth and other planets. Such space weather is capable of affecting the electronics of satellites, spacecraft orbits, radio communications, railway transportation and power grids on the ground, and even underground pipelines. Space weather is present all the time, but can be extreme occasionally, like the storm weather in the atmosphere from time to time. The term "space weather" was originated in the 1950s and became popular in the 1990s. After that, "space climate" referred to the large-scale and long-term patterns of space weather attracted more attention. Both ground-based and satellite-based observation of space weather are applied in the scientific research, which makes the prediction of space weather possible based on the established models for simulating the space weather environment.

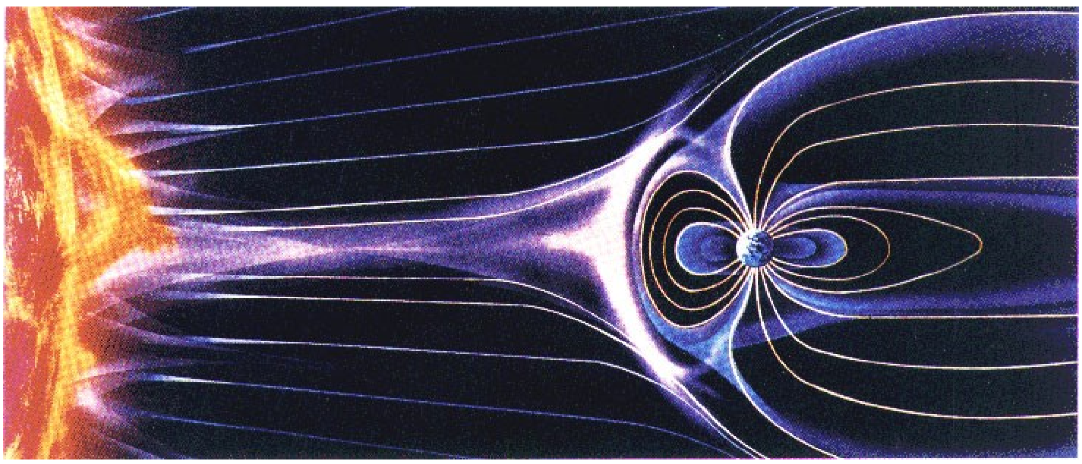

Figure 1.1 Solar wind between Sun and Earth. **Credit:** NCAR

1.3 Earth's Magnetosphere and Space Current Systems

Around a planet is a region controlled by the planet's magnetic field, which is thus called a magnetosphere. For example, the structure of the Earth's magnetosphere shown in Figure 1.2 below, is affected by the blast of solar wind. The solar wind emitted out from the Sun compresses the magnetosphere on the dayside to a distance of about 6 to 10 times the radius of the Earth (R_E), depending on the strength. A supersonic shock wave is created on this side, which is called bow shock. The bow shock heats and decelerates most of the solar wind particles that then moves around the Earth in the magnetosheath. The nightside magnetosphere extends to possibly 1000 R_E. This extended structure of the magnetosphere is known as the magnetotail. The magnetopause depicts the outer boundary of Earth's geomagnetic field cavity. Solar variations play a significant role in shaping the Earth's magnetosphere. The interactions of the Earth's magnetic field with the solar wind give rise to a multitude of space current systems as Figure 1.3 shows, flowing in a vast region ranged 2 to 20 R_E from the Earth.

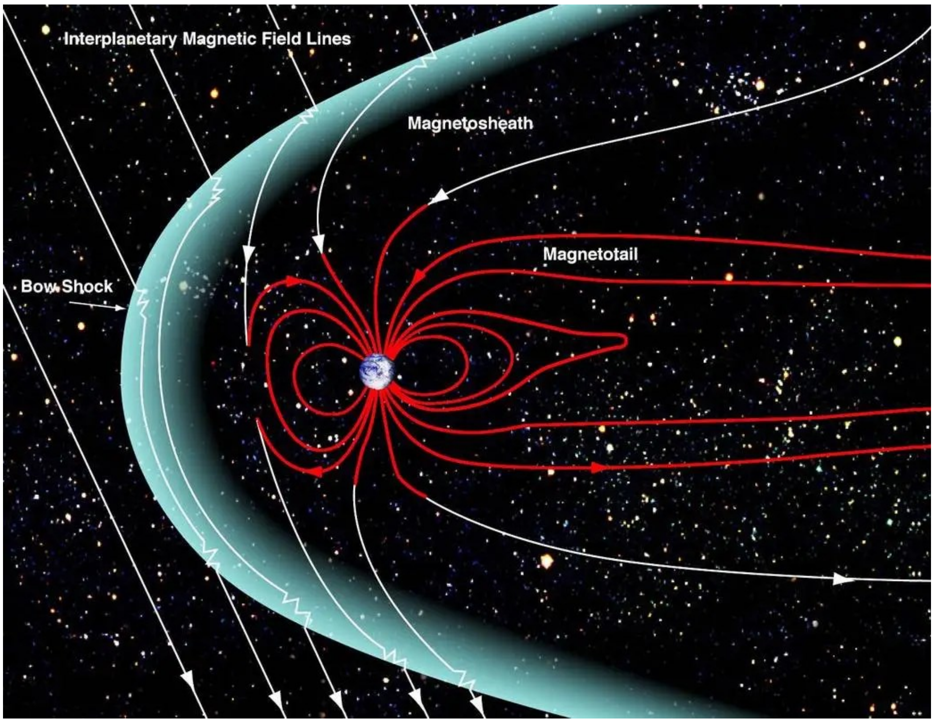

Figure 1.2 Earth's magnetosphere. **Credit:** NASA/Goddard/Aaron Kaase

The space current systems in the Earth's magnetosphere mainly includes: Chapman-Ferraro magnetopause currents, tail currents, Region 1 field-aligned currents (FACs), symmetric ring currents, partial ring current and Region-2 FACs. The specific structure of FACs is shown in Figure 1.4.

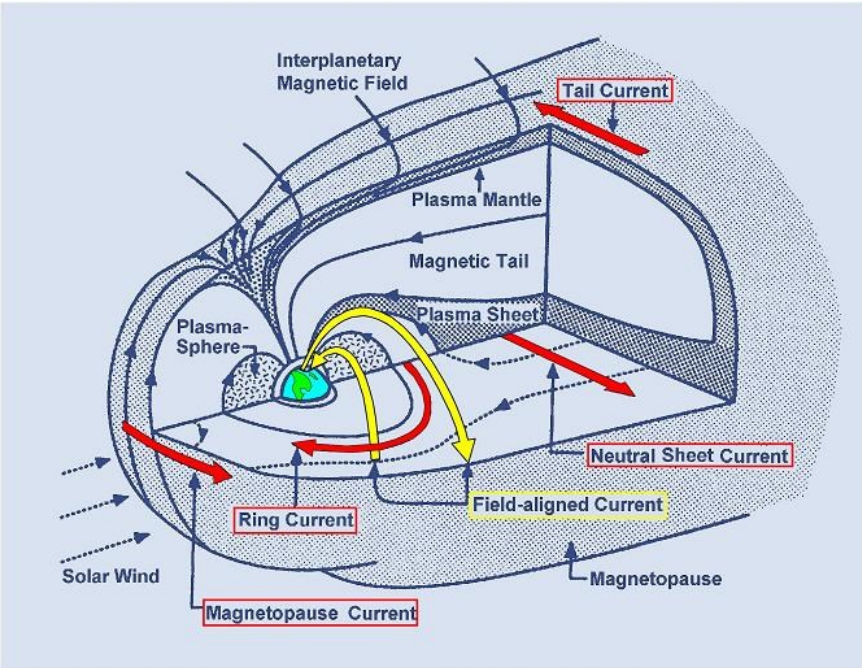

Figure 1.3 A sketch of current system in the magnetosphere modified from Kivelson & Russell (1995).

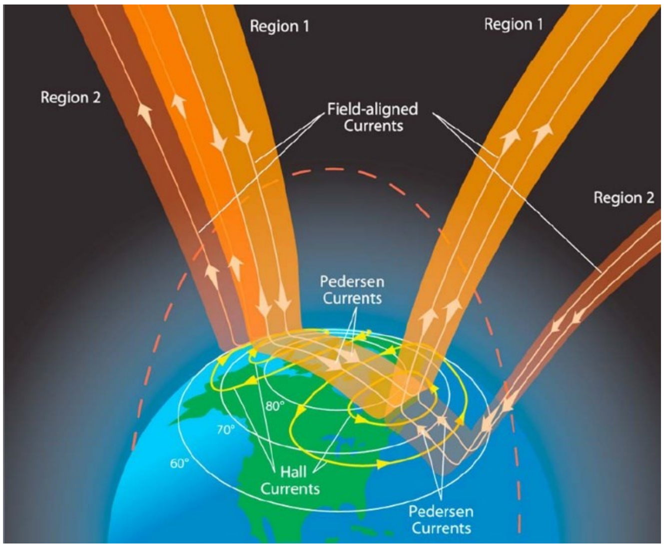

Figure 1.4 A schematic of field-aligned currents combined with ionospheric currents from Le et al. (2010).

1.4 Geomagnetic Disturbances (GMDs)

Geospace is closely related with solar activities. GMD events are caused by the interaction between the solar wind and the magnetosphere. The Earth's magnetic field is correspondingly disturbed and under extreme conditions the effects may cause damage to fundamental infrastructure, including power systems. The geomagnetic disturbances can be measured at geomagnetic observatories recording the three components of magnetic field. The intensity of geomagnetic activity (including different GMD events) is usually indicated by *Kp* index (values from 0 to 9), which was introduced by Julius Bartels to measure solar particle radiation from the magnetic effects. The mean value of the disturbance levels in the two horizontal field components, observed at 13 selected subauroral stations, is calculated as the result of the index. The name *Kp* is originated from "*planetarische Kennziffer*" (planetary index), and it is an improvement of previously used *K*-index (Bartels et al., 1939), which remains to locally describe disturbances in the vicinity of each observatory. Severe GMD events usually occur when *Kp* = 7 or higher.

There are many other geomagnetic indices that manifest the strength of different geomagnetic activities. The GMDs events that take place in different regions have different sources. Depending on the disturbance latitude, various magnetic indices are used. For example, the *AE* (auroral electrojet) index is designed to offer a global, quantitative measure of magnetic activity in the auroral zone due to enhanced ionospheric currents flowing beneath and inside the auroral oval. The magnetospheric substorm events can be characterized by this index, which is used to study the response of M-I coupling. The *Dst* (disturbance storm time) index is derived from a network of geomagnetic observatories near the equator that measures the strength of the globally symmetrical equatorial electrojet (the "ring current"), which indicates the geomagnetic activity. It is also affected by magnetopause currents and tail currents (Burton et al., 1975). The SYM-H (symmetric) index is introduced to describe the geomagnetic disturbance in mid-latitude region with high-time resolution, which is essentially the same as the *Dst* index. In this thesis, the GMDs involved are mainly sudden commencements (SCs), magnetic storms, and bay disturbances. The GMDs can be used to calculate the resulting electric fields on the ground by convolution method combined with ground conductivity (details explained in next chapter).

1.5 Geomagnetically Induced Electric Fields and Currents

The GMDs on the ground induce the electric field according to Faraday's law. When this induced electric field is applied to a long conductor, e.g. a power grid, currents will be generated in the power lines, flowing between the ground points in the system, which is called geomagnetically induced currents (GICs) as shown in Figure 1.5. The GMD impacts on power systems through this current, causing the problems including core saturation of power transformers, harmonics of generators, tripping of capacitor bank and system voltage instability due to the increased absorb of reactive power. Protection systems of the power grid are also under challenge when GIC level is high.

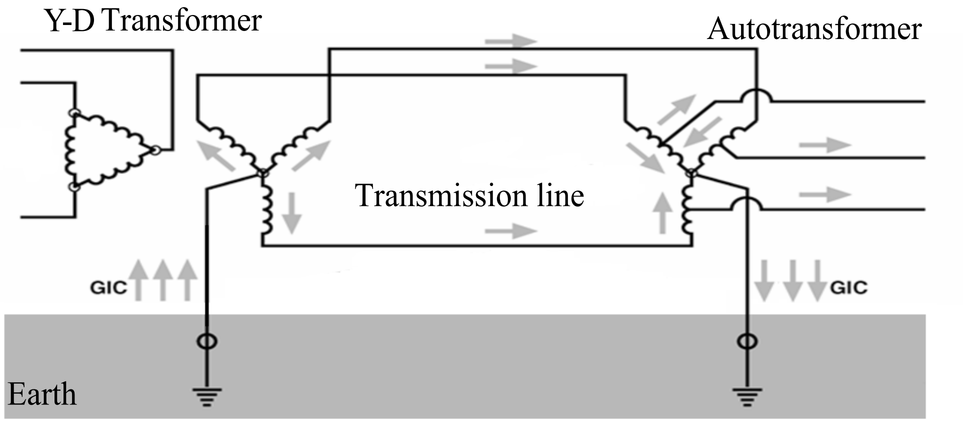

Figure 1.5 Flow of GIC in power grid adapted from Molinski (2002)

Different with the traditional work of modelling GIC based on geomagnetic field measurement, the real-time estimation of potential GICs aroused in the power system according to instantaneous observation of solar wind condition seems to be a better strategy for preventing the potential harm. The engineering step of this work is monitoring the GICs in a particular power network, and then obtaining an empirical relationship between the measure of GICs and the information of the network by a linear combination of horizontal component of induced electric fields (see details in Section 2.1). The more simplified method of predicting GICs under extreme solar conditions in power systems is to set an upper-limit of the induced geoelectric field values as done in the benchmark GMD event, which defines a regional geoelectric field peak amplitude (E_{peak}) in calculating GICs through statistical analysis of a reference geoelectric field amplitude, and two scaling factors accounting for local geomagnetic latitude and earth conductivity structure, separately. The demanding work is the geophysical step, which aims for understanding the geomagnetic response under varied solar wind conditions and establishing a global map of the response to space current systems.

1.6 Summary

Three main topics are thoroughly investigated in the thesis, including geoelectric field variations in response to different GMD events, nighttime geomagnetic response to jumps of solar wind dynamic pressure, and generation of FACs in response to sudden enhancement of solar wind dynamic pressure. It is believed that this thesis will bring a comprehensive understanding of how electric field on the ground reacts to sudden commencements (SCs), magnetic storms, and substorms. The statistical analysis of the relationship between GMDs and geomagnetically induce electric field (GIE) will enable to predict the GICs flowing in power networks based on the corresponding empirical models obtained, which favors the prevention of GIC problems in power grids. Furthermore, a preliminary global map of geomagnetic response to solar wind pressure pulse from the equator to the pole is expected to be drawn according to the MHD simulation results, which is useful to distinguish the sensitive region where power systems may suffer from GIC risks and provide time for avoiding GIC harm on power grids when the solar wind condition is available.

Chapter 2 Geoelectric Field Disturbances in Japan in Response to Different GMDs

2.1 Introduction

Geomagnetically induced current (GIC) is a major concern at high latitudes, in particular, geomagnetic latitudes larger than 50° (Pulkkinen et al., 2012; Ngwira et al., 2013). Observations have shown that large-amplitude GICs also flow at geomagnetically low latitudes. For example, 55.8 A of GIC was observed in the Chinese power grid during the 9 November 2004 magnetic storm (Liu et al., 2009). During the 28-30 October 2003 magnetic storm, 129 A of GIC was recorded in the Japanese power grid (Ministry of Economy, Trade and Industry of Japan, 2015). Ebihara et al., (2021) estimated that 89 ± 30 A of GIC flows at a particular substation in the Japanese power grid if the Carrington-class event occurs again. Note that the estimated value is the lower limit, so that larger GICs may flow at other substations in Japan. These observations and estimation suggest that the power grids at low latitudes may also face the risk against the GICs. While technical efforts have been conducted to prevent potential risk (e.g., Guo et al., 2015; Etemadi & Rezaei-Zare, 2014; Lu et al., 2018; Lesher et al., 1994; Overbye et al., 2013), quantitative estimation of the largest GICs is awaited to design the technical system and conduct a proper operation of the power grid.

GICs flow in long, low-resistivity conducting lines connecting to the Earth. According to Faraday's law, the change in the magnetic field (B) induces the electric field (E) in the conducting lines and in the Earth, driving the current. The time derivative of the geomagnetic field ($\partial B/\partial t$) is often used to evaluate the GIEs and the GICs (e.g., Pulkkinen et al., 2012; Dimmock et al., 2020; Groom & Bailey, 1989; Ngwira et al., 2018; Kataoka & Ngwira, 2016; Piersanti & Villante, 2016; Piersanti et al., 2019; Engebretson et al., 2021). On the basis of a theory by Cagniard (1953), time-series variations of GIEs have also been calculated by taking the convolutions of $\partial B/\partial t$ with assumed ground conductivities (Love & Swidinsky, 2014; Ebihara et al., 2021). These authors calculated the GIEs in the time domain with the observed geomagnetic data collected at Kakioka under the plane-wave approximation. In fact, this relationship between B and E field corresponding to a certain kind of geomagnetic activity can be indicated by the Earth transfer function (K) in the frequency domain or time domain by the convolution, which contains not only the information of the Earth conductivity structure but also the driven source of GIEs/GICs (Boteler & Pirjola, 2017). They pointed out that K is related to the magnetotelluric surface impedance and the complex skin depth, and for modeling GIC there is a need to be able to include both large-scale and small-scale magnetic source fields due to distant (magnetospheric) and nearby (ionospheric) currents, respectively. All the efforts done by researchers mentioned above are aiming to acquire a more accurate electric field as an input to model the GIC. Although it is pointed out that for realistic E fields, only voltage sources in the transmission lines can accurately represent the E fields and hence give the correct GIC values (Boteler & Pirjola, 2017), the height of the power transmission line is much shorter than the horizontal length, the electric field integrated round the loop between the transmission line and the ground is very small. The electric field induced in the transmission line is suggested to be the same as the electric field induced in the Earth's surface. In that sense, GIC is directly related to the geomagnetically induced electric field (GIE). Besides, Love & Swidinsky, (2014) and Ebihara et al. (2021) both showed that the GIEs at the Kakioka observatory of the Japan Meteorological Agency (36.23°N, 140.19°E) can be reasonably reproduced by the convolution theory with proper electric conductivity of the ground and a galvanic tensor (K in different directions). In other words, direct measured E fields show a good consistency with the results getting from the B field data combined with the transfer function (see results of the comparison in (Love & Swidinsky, 2014; Ebihara et al., 2021)). For given GIEs (whether measured or modelled), the current flowing in the power grid can be determined from the requirement of the current continuity (Lehtinen & Pirjola, 1985). Thus, the electrical parameters of the power grid, such as transmission resistivity and topology of the grid, are needed to evaluate the GIC.

For a certain power grid, it is known that GICs can be reasonably expressed by a linear combination of the two components of the GIEs (Pulkkinen et al., 2007; Viljanen et al., 2004; Zhang et al., 2020; Ebihara et al., 2021) as

$$\mathrm{GIC}(t) = a + b\Delta E_x(t) + c\Delta E_y(t), \tag{2.1}$$

where ΔE_x and ΔE_y are the GIEs in the north-south and the east-west components, respectively, and *a*, *b* and *c* are parameters likely depending on the topology of the network and resistance of it. *a* refers to an offset, probably including noise (Pulkkinen et al., 2007). With known GIEs and parameters (*a*, *b* and *c*), one can calculate GICs with sufficient accuracy. Ebihara et al. (2021) derived the parameters for Shin-Fukushima (SFS), Shin-Tsukuba (STB), and Shin-Fuji (SFJ) substations. These substations are connected to the 500 kV power transmission lines, and located in a suburban area of Tokyo, Japan (27°-29° geomagnetic latitudes). The parameters are summarized in Table 2.1. With the parameters and the GIEs observed at the Kakioka observatory, the calculated GICs at the 3 substations are well correlated with the observed ones with correlation coefficients of 0.91, 0.91, and 0.81, respectively. Ebihara et al. (2021) focused on 3 magnetic storms. For example, the maximum GICs are expected to be 14.4, 3.3 and 16.7 A at SFS, STB and SFJ, respectively, during the 13 March 1989 magnetic storm.

Table 2.1 Coefficients, *a*, *b* and *c* for substations SFS, STB and SFJ Ebihara et al. (2021).

Substation	*a* (A)	*b* (A/(mV/km))	*c* (A/(mV/km))
Shin-Fukushima (SFS)	–0.80	–0.0892	0.0602
Shin-Tsukuba (STB)	0.02	0.0195	–0.0133
Shin-Fuji (SFJ)	–0.32	–0.303	0.0422

Watari et al. (2021) showed that the GICs at STB and SFJ increase in accordance with different types of geomagnetic variations, including (1) storm sudden commencements (SSCs) and sudden impulses (SIs), (2) storm main and recovery phases, (3) bay disturbances, and (4) solar flare effect (SFE). The ultimate source of these variations is the Sun, but the current systems involved and the physical processes differ from type to type.

1) SSCs and SIs are known to occur when the solar wind dynamic pressure rapidly increases. When the magnetosphere is compressed, the magnetopause current flowing eastward is intensified, resulting in a positive deflection of the horizontal component of the geomagnetic field *H*. This type of deflection is called a DL-field (Araki, 1994). The compression of the dayside magnetosphere also launches magnetohydrodynamics waves propagating anti-sunward. In the course of the propagation, field-aligned currents are excited, which are connected to the ionosphere. The resultant ionospheric current deflects *H*, called a DP field (Araki, 1994). The DL-field is significant at low-latitudes, whereas the DP-field is significant at auroral latitudes (Araki, 1994). The rise time of the SSCs/SIs ranges from ~1 to ~12 minutes, and the rate of change in the horizontal component of the geomagnetic variation increases with the peak amplitude of it (Araki et al., 2004). $\partial B/\partial t$ is shown to increase just after SSCs/SIs from high latitudes to the magnetic equator (Carter et al., 2015; Carter et al., 2016). Carter et al. (2016) discriminated between the magnetospheric contribution and the ionospheric contribution, and discussed the impact on GICs.

2) The negative deflection of *H* lasting for a few days is called a geomagnetic storm (Gonzalez et al., 1994). The variations are caused by the storm-time ring current (Burton et al., 1975; Ebihara & Ejiri, 2003 and references therein). The contribution from the tail current is also suggested (Ohtani et al., 2001). When the southward component of the interplanetary magnetic field (IMF) being less than −10 nT lasts for 3 hours, intense magnetic storms with minimum *Dst* less than −100 nT occur with a probability of 80% (Gonzalez et al., 1994).

3) At high latitudes, *H* rapidly decreases owing to the development of the westward auroral electrojet during the expansion phase of a substorm. At mid and low latitudes, the contribution from the auroral electrojet is small, but the contribution from the field-aligned current is thought to cause a positive excursion of *H*, known as a positive bay (Meng & Akasofu, 1969; Akasofu & Meng, 1969; McPherron et al., 1973). It has been believed that the field-aligned current is part of the substorm current wedge (Kepko et al., 2015), in which a large-amplitude field-aligned current flows into the ionosphere on the dawnside, and out of the ionosphere on the duskside. The mid-latitude positive bay rapidly rises to a peak in ~20 minutes, followed by a gradual decay (McPherron & Chu, 2018).

Woodroffe et al. (2016) presented the latitudinal distribution of ΔB, $\partial B/\partial t$ and E from 20° to 75° magnetic latitudes for different storm intensity in terms of Dst. The electric field E was calculated by using the 6-layer ground conductivity model (Boteler, 2015). They showed that the large-amplitude geomagnetic disturbances ($\partial B/\partial t$ > 5 nT/s) can occur as low as 45°-55° magnetic latitudes during severe and extreme storms. At magnetic latitudes of 45°-55°, 100-year geomagnetic disturbance ΔB is 738-1987 nT. The electric field E frequently exceeds 1 V/km during strong and severe storms at $\geq 50°$geomagnetic latitude.

The aims of this chapter are to understand the major causes of large-amplitude the electric fields and GICs and the occurrence distribution of them at low latitudes on the basis of the electric field observed the Kakioka observatory. Given that the magnetic latitude of the Kakioka observatory is about 27.8°, this research can illuminate the response of the electric fields (and GICs) to the geomagnetic disturbances at low latitudes where Woodroffe et al. (2016) did not discussed well. In this section, we focused on the first 3 types of the variations, that is, the SSCs/SIs, the main phase of storms, and the bay disturbances. We excluded the variation associated with the SFEs because the amplitude associated with the SFEs is relatively small. Knowing ΔE_x and ΔE_y, we calculated the GICs flowing at the substations in Japan with the aid of Equation (2.1) and the parameters summarized in Table 2.1.

2.2 Data source

2.2.1 Geoelectric field data

We used 1-min resolution data of the geoelectric field observed at Kakioka Magnetic Observatory (36.23°N, 140.19°E, 27.8° geomagnetic latitude). The x- and y-components refer to the geographical north and east components, respectively. The technical description of the measurement of the geoelectric field is given by Fujii et al., (2015). It is confirmed that the horizontal components of the geoelectric field are induced by variations in the geomagnetic field at periods below 10^5 s, which enables us to utilize the geoelectric field data as a proxy of GICs. The geoelectric field at periods below 10^2 s is suffered from artificial noise, but the coherence between the geoelectric field and the geomagnetic field is shown to increase for geomagnetic storms (Fujii et al., 2015). We focus on the variations with a period < 10^5 s, and believe that the observed electric field is induced by geomagnetic variations.

2.2.2 Sudden commencements (SCs)

We used 218 SSCs/SIs identified by Kakioka Magnetic Observatory (http://www.kakioka-jma.go.jp) from 1996 to 2004 (around the maximum of the 23th solar cycle). We excluded 5 SSCs/SIs for which the geoelectric data is missing. In total, 213 SSCs/SIs were used to perform the analyses, and the beginning of SSCs/SIs is referred to as the epoch time denoted by ep_1.

2.2.3 Magnetic storms (main phase)

We focused on intense magnetic storms having minimum *Dst* index being less than −100 nT from 1996 to 2004, which were collected by Kataoka & Miyoshi (2006). Only the magnetic storms driven by coronal mass ejections (CMEs) are used in this study because clear SSCs/SIs preceded the main storm. We excluded the 13 magnetic storms for which the duration from the SSCs/SIs to the end of the main phase is longer than 24 hours, or the geoelectric field data is missing. The original list (Kataoka & Miyoshi, 2006) provides the storm maximum in terms of 1-hour *Dst* index. We redefine the storm maximum at which the 1-minute SYM-H index reached the minimum, and referred it to as ep_2. The minimum SYM-H ranges from −490 nT to −106 nT.

We have repeated the same analyses for moderate magnetic storms (−100 nT < minimum Dst ≤ −50 nT) from 1996 to 2008 (Echer et al., 2013; Echer et al., 2011). However, the geoelectric field disturbances are smaller than those for the intense magnetic storms, and the qualitative results are almost the same as those for the intense magnetic storms. Thus, the results for the moderate magnetic storms are not shown here.

2.2.4 Bay disturbances

We used a list of the bay disturbances identified by Kakioka Magnetic Observatory (http://www.kakioka-jma.go.jp). In accordance with the amplitude, 3 classes are defined in the identification of the bays, A, B and C. We used all the classes, that is, the amplitudes of it exceeds 10 nT for quiet times and 25 nT for active times. In total, 325 bay disturbances that took place from 1996 to 2004 were used to analyze. The beginning of bay disturbances is referred to as the epoch time denoted by ep_3.

2.2.5 Data example

Figure 2.1 shows an example of the *y*-component of the geoelectric field E_y and H observed at Kakioka on 18-20 October 1998. During this interval, an SSC, an intense magnetic storm and a bay disturbance occurred. At 1951 UT on 18 October 1998, H started to increase rapidly, corresponding to an SSC. This moment is regarded as ep_1. At the same time, E_y started a negative excursion. Then, the main phase of the storm began at ~04 UT on 19 October 1998 as identified from a decrease in H. A negative SI-like disturbance took place during the storm main phase, along with H decreased by more than 100 nT (This event has been identified as a SI according to the latest data provided by Kakioka Magnetic Observatory). The SYM-H reached the minimum value at 1522 UT, which is regarded as ep_2. During the storm main phase, a positive bay disturbance commenced at 1320 UT on 19 October 1998, which is regarded as ep_3. The bay disturbance brought a great impact on the variations of the geoelectric field. E_y shows a negative excursion with an approximate amplitude of ~ 150 mV/km correspondingly. Later, we evaluate the contribution from the storm-time ring current to GIE. For this particular magnetic storm, we excluded the influence on the variations brought by SI disturbance (0455 UT on 19 October 1998) and the bay disturbance (1320 UT on 19 October 1998) through a smoothing process (explained in detail in Section 2.3.2), and obtained the maximum amplitude of geoelectric field disturbance E_y at 1110 UT on 19 October 1998.

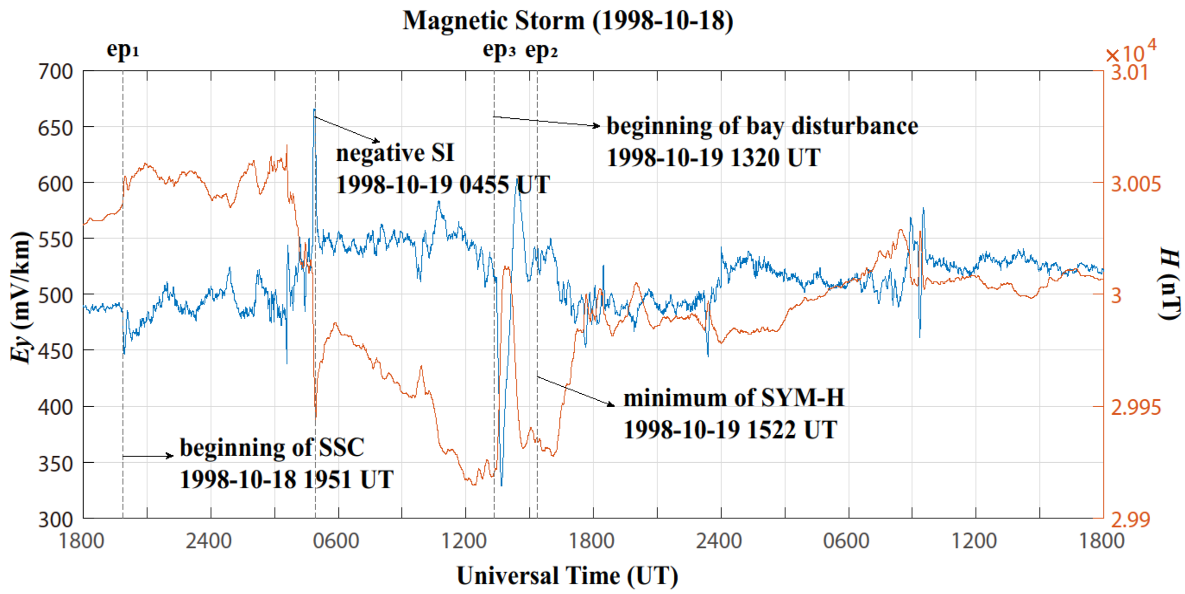

Figure 2.1 The blue line indicates the y-component of geoelectric field Ey and the orange line indicates the horizontal component of the geomagnetic field H at Kakioka on 18-20 Oct.1998.

2.3 Geoelectric Response to GMD Events

2.3.1 Sudden commencements

We calculated the disturbances of the magnetic field $\Delta\mathbf{B}_1$ and the electric field $\Delta\mathbf{E}_1$ as

$$\begin{aligned}\Delta\mathbf{B}_1(t) &\equiv \mathbf{B}(t) - \mathbf{B}(\mathrm{ep}_1),\\ \Delta\mathbf{E}_1(t) &\equiv \mathbf{E}(t) - \mathbf{E}(\mathrm{ep}_1).\end{aligned} \tag{2.2}$$

Figure 2.2 shows the superposed epoch averages of $\Delta\mathbf{B}_1$ and $\Delta\mathbf{E}_1$ for the epoch time ep$_1$. On average, $\Delta B_{1,x}$ shows a rapid increase after ep$_1$. This is a typical tendency for the geomagnetic disturbances associated with SSCs/SIs. That is, the sudden increase in the solar wind dynamic pressure enhances the dayside magnetopause current, resulting in the northward magnetic field disturbance on the ground (Gosling et al., 1967; Ogilvie et al., 1968). Negative changes in $\Delta B_{1,x}$ are also included in this figure, which are likely associated with a sudden decrease in the solar wind dynamic pressure (Nishida & Jacobs, 1962; Takeuchi et al., 2000). The averaged $\Delta B_{1,y}$ also shows an increase, but the magnitude is smaller than that of $\Delta B_{1,x}$. $\Delta E_{1,x}$ and $\Delta E_{1,y}$ show negative excursions. The averaged $\Delta E_{1,y}$ reaches −65 mV/km, whereas that of $\Delta E_{1,x}$ reaches −11 mV/km about 3 minutes after ep_1. At Kakioka, the northward magnetic disturbances are known to cause the induced electric field primarily in the westward direction (Love & Swidinsky, 2014).

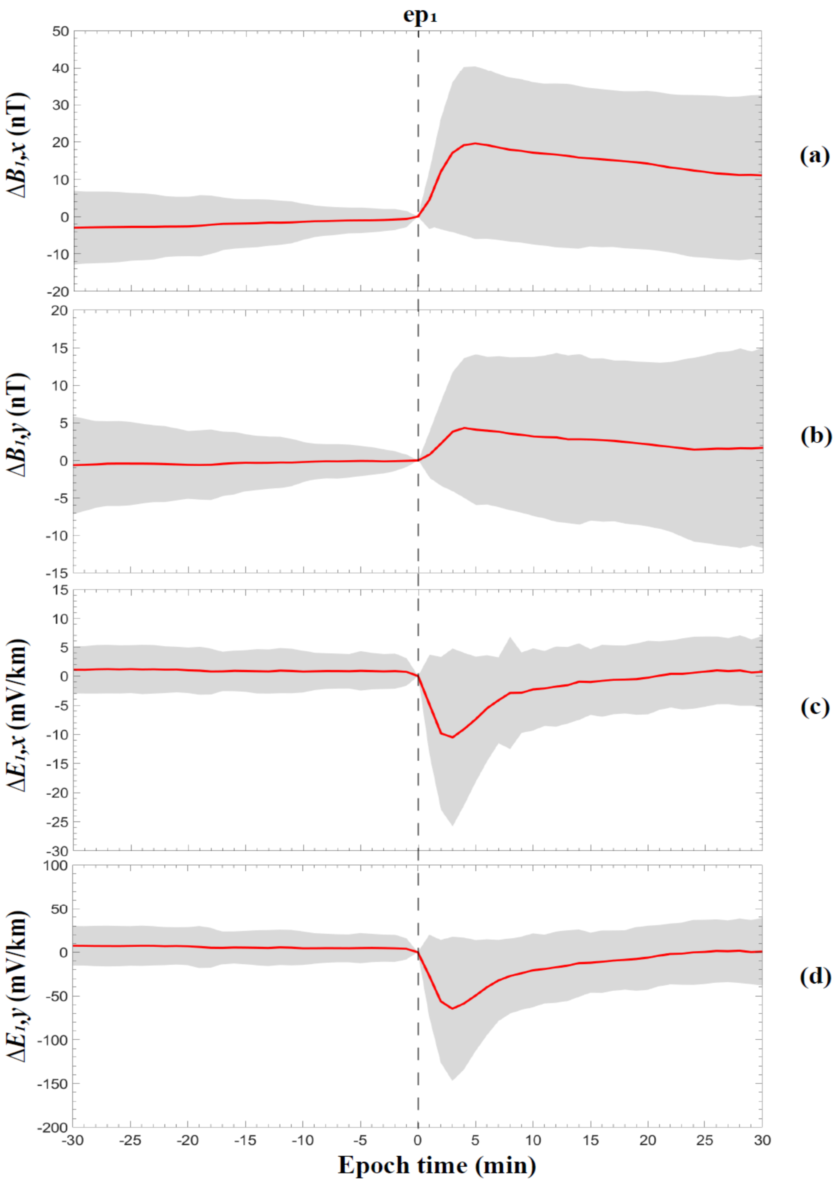

Figure 2.2 Superposed epoch averages of (a) $\Delta B_{1,x}$ (positive northward), (b) $\Delta B_{1,y}$ (positive eastward), (c) $\Delta E_{1,x}$ (positive northward), and (d) $\Delta E_{1,y}$ (positive eastward). The red lines indicate the averaged values and the gray regions indicate standard deviations. ep_1 refers the moment at which SSCs/SIs begin.

We sorted $\Delta E_{1,y}$ in accordance with magnetic local time (MLT) sectors, 00-06, 06-12, 12-18 and 18-24 MLTs. The results are shown in Figure 2.3. $\Delta E_{1,y}$ shows similar variations after ep_1 for all the MLT sectors. The maximum amplitudes of averaged $\Delta E_{1,y}$ are about 77, 36, 57, and 80 mV/km in 00-06, 06-12, 12-18 and 18-24 MLTs, respectively. The maximum amplitudes are slightly larger on the nightside than those on the dayside. This is probably caused by the contribution from the field-aligned current and the ionospheric current that developed on the nightside during the SSCs and SIs (Araki et al., 2006).

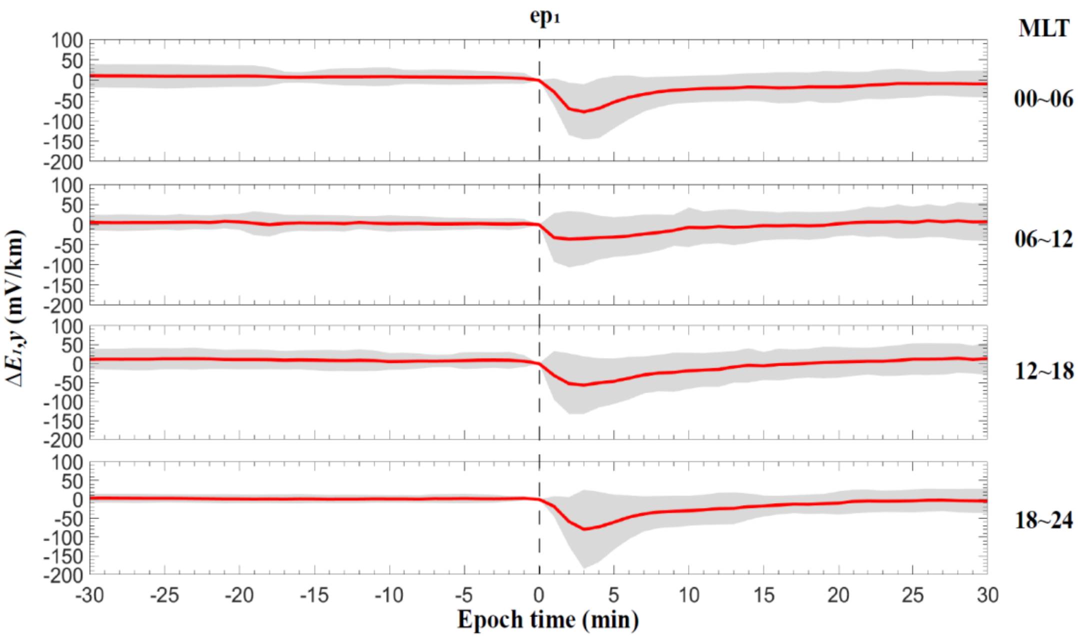

Figure 2.3 Superposed epoch averages of $\Delta E_{1,y}$ for the SSCs/SIs for 4 MLT sectors.

The relationship between $\Delta E_{1,x}$ and $\Delta E_{1,y}$ at the maximum $|\Delta \boldsymbol{E}_1|$ for the period from ep_1 to ep_1+15 minutes are shown in the left panel of Figure 2.4. $\Delta E_{1,x}$ and $\Delta E_{1,y}$ are highly correlated with each other. The dependence of $\Delta E_{1,x}$ and $\Delta E_{1,y}$ on ΔH is shown in the middle and the right panels of Figure 2.4. At a glance, linear relationship can be reasonably identified. We obtained the following regression lines without intercepts,

$$\begin{aligned} \Delta E_{1,x}(\mathrm{mV/km}) &= -(0.73 \pm 0.05)\Delta H(\mathrm{nT}), \\ \Delta E_{1,y}(\mathrm{mV/km}) &= -(4.31 \pm 0.12)\Delta H(\mathrm{nT}). \end{aligned} \tag{2.3}$$

The correlation coefficients are −0.68 and −0.97 for $\Delta E_{1,x}$ and $\Delta E_{1,y}$, respectively. The numerical figures following the symbol of ± represent the upper and lower limits of the 95% confidence level of the slope. The physical meaning of the linear relationship will be discussed below. Of course, the empirical equation is crude in comparison with a convolution method (Love & Swidinsky, 2014). The usefulness and the application to GICs will also be discussed below.

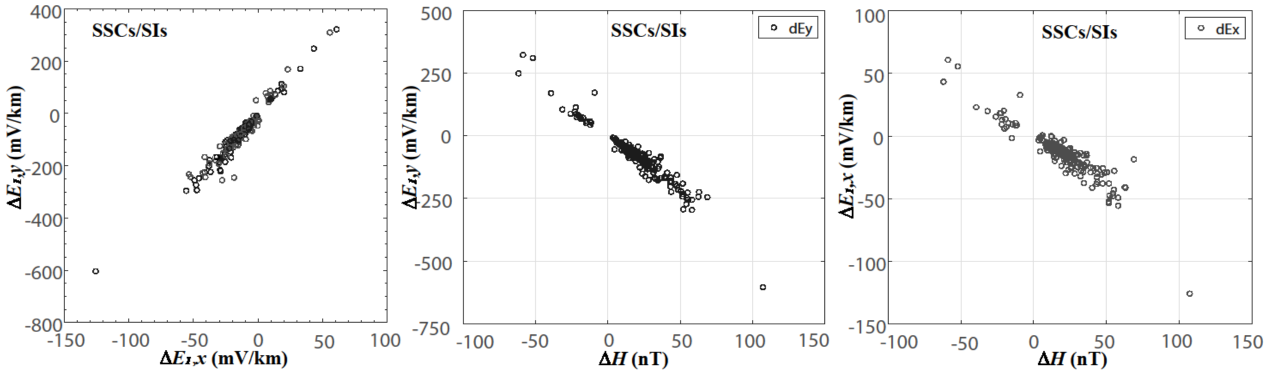

Figure 2.4 Relationship between (left) $\Delta E_{1,y}$ and $\Delta E_{1,x}$; relationship between (middle) $\Delta E_{1,y}$ and ΔH; and (right) $\Delta E_{1,x}$ and ΔH at the maximum of $|\Delta \boldsymbol{E}_1|$ for the SSCs/SIs.

2.3.2 Magnetic storms (main phase)

Figure 2.5 shows the result of the superposed epoch analysis of $\Delta\mathbf{B}_1$ and $\Delta\mathbf{E}_1$ for the epoch time ep_2. ep_2 corresponds to the moment when the SYM-H index reached a minimum, that can be regarded as a storm maximum. At a glance, the averaged $\Delta B_{1,x}$ decreases during the storm main phase (before ep_2), and increases during the storm recovery phase (after ep_2). These changes are well consistent with those in the SYM-H index. $\Delta E_{1,y}$ increases during the storm main phase, and decreases during the recovery phase. It reaches the maximum value of 84 mV/km at ep_2, at which the rate of change in $\Delta B_{1,x}$ is almost zero. After ep_2, the averaged $\Delta E_{1,y}$ starts to decrease and remains positive for a few hours, while the averaged $\Delta B_{1,x}$ monotonically increases. This can be explained by the cumulative effect of geomagnetic variations, according to the convolution theory suggested by Cagniard (1953). That is, the peak of GIE tends to appear where $\partial B/\partial t$ changes the sign. We have not found significant dependence of $\Delta\mathbf{E}_1$ on MLT (data not shown).

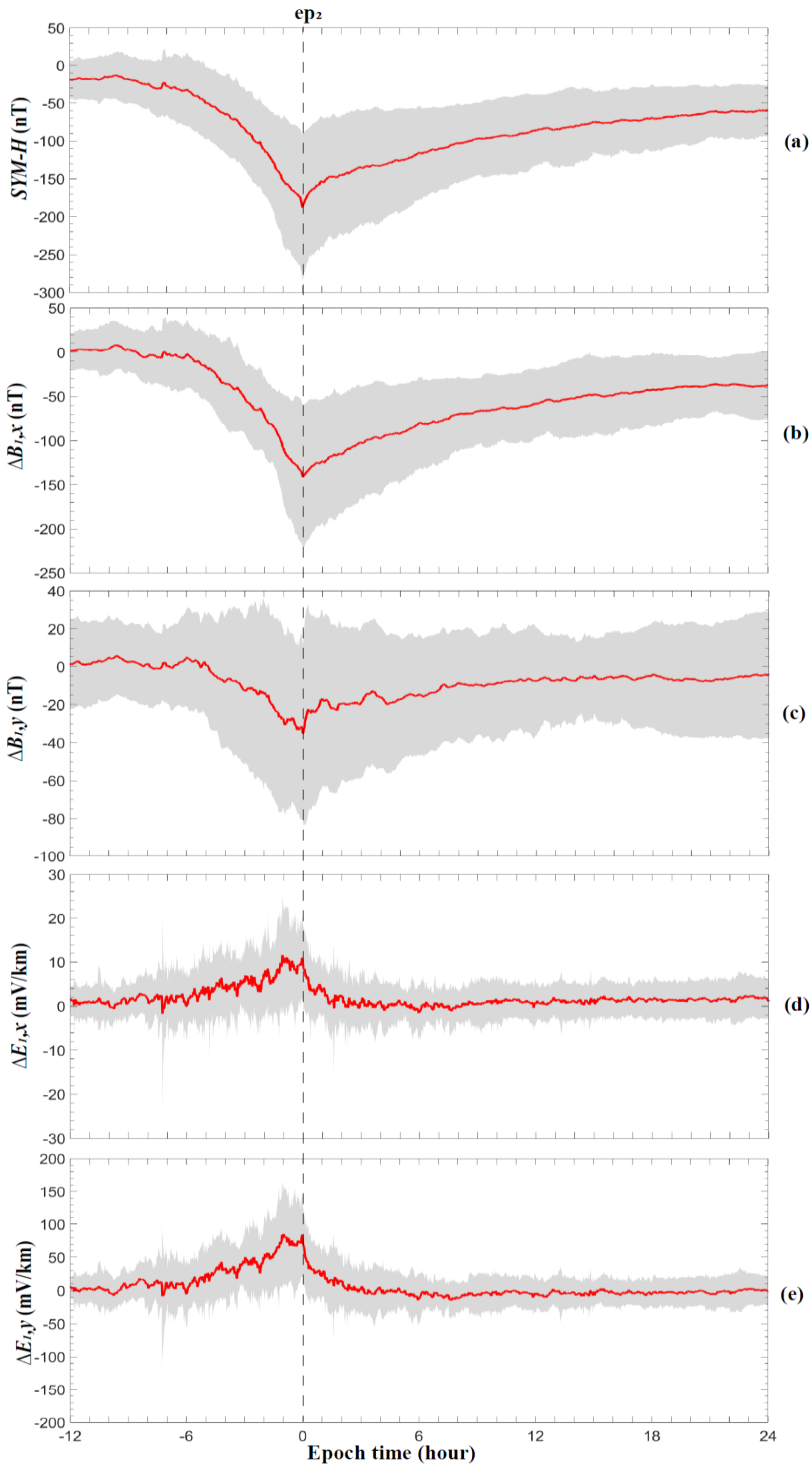

Figure 2.5 Superposed averages of (a) SYM-H (b) $\Delta B_{1,x}$ and (c) $\Delta B_{1,y}$, (d) $\Delta E_{1,x}$ and (e) $\Delta E_{1,y}$ for the intense storms. ep_2 refers to the moment at which the SYM-H index reaches the minimum.

Figure 2.6 is the same as Figure 2.4 except for storm main phase. We removed short-lived spikes and SI-like disturbances by applying a moving median method, and took the maximum amplitude of $|\Delta \boldsymbol{E}_1|$ for the period from ep_1+15min to ep_2. Again, fairly well correlation between $\Delta E_{1,x}$ and ΔH, and that between $\Delta E_{1,y}$ and ΔH are found. From the linear regression analysis, we obtained the following equations.

$$\begin{aligned} \Delta E_{1,x}(\mathrm{mV/km}) &= -(0.11 \pm 0.01)\Delta H(\mathrm{nT}), \\ \Delta E_{1,y}(\mathrm{mV/km}) &= -(0.85 \pm 0.11)\Delta H(\mathrm{nT}). \end{aligned} \tag{2.4}$$

The correlation coefficients are −0.64 and −0.76 for $\Delta E_{1,x}$ and $\Delta E_{1,y}$, respectively. The physical meaning of Equation (2.4) and the application will be discussed below.

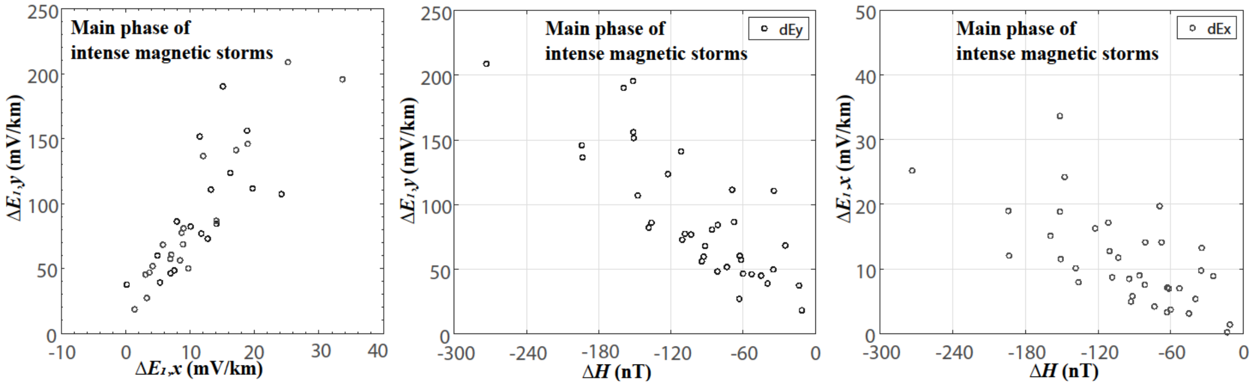

Figure 2.6 Same as Figure 2.4 except for the moment when the maximum value of $|\Delta \boldsymbol{E}_1|$ took place for storm main and recovery phases.

2.3.3 Bay disturbances

Figure 2.7 shows the results of the superposed epoch averages of the GIEs for the bay disturbances. The disturbances of the magnetic field $\Delta\mathbf{B}_3$ and the electric field $\Delta\mathbf{E}_3$ for the epoch time ep_3 were obtained by

$$\begin{aligned} \Delta\mathbf{B}_3(t) &\equiv \mathbf{B}(t) - \mathbf{B}(\mathrm{ep}_3), \\ \Delta\mathbf{E}_3(t) &\equiv \mathbf{E}(t) - \mathbf{E}(\mathrm{ep}_3). \end{aligned} \tag{2.5}$$

where ep$_3$ refers to the moment at which the bay disturbances begin. $\Delta B_{3,x}$ shows a rapid increase, and reaches a maximum about 40 minutes after ep$_3$, which is consistent with a typical variation of the positive bay (Meng & Akasofu, 1969; Akasofu & Meng, 1969; McPherron et al., 1973). $\Delta E_{3,x}$ and $\Delta E_{3,y}$ show negative excursions, and reached minima about 25 minutes after the expansion onset.

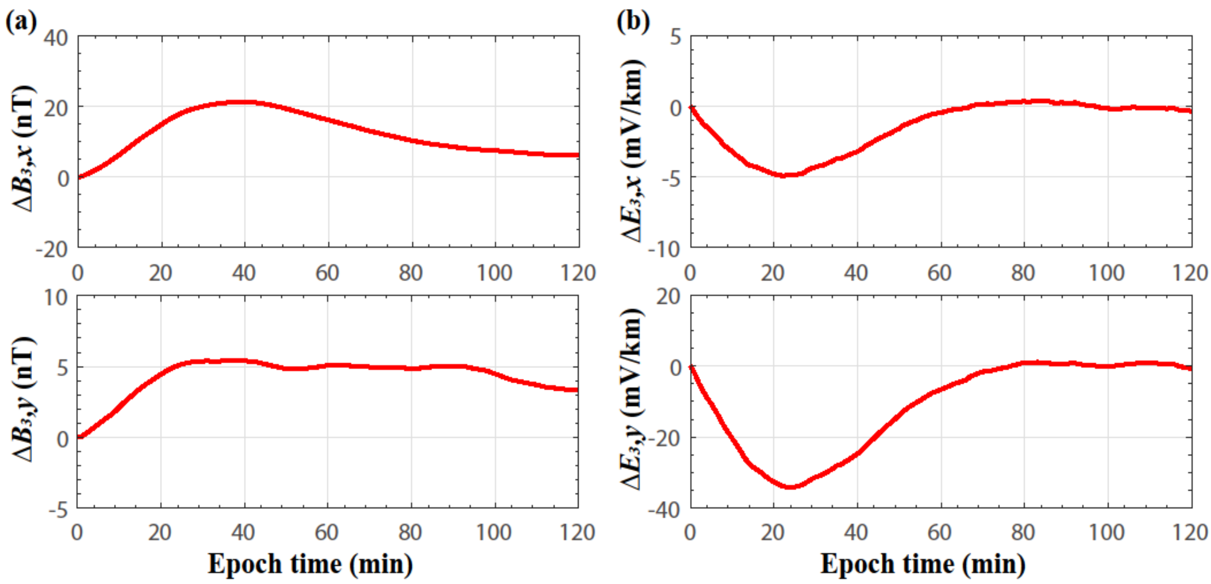

Figure 2.7 Superposed epoch averages of (a) ΔB_3 and (b) ΔE_3 for the bay disturbances. ep$_3$ refers to the moment at which the bay disturbances begin.

Figure 2.8 shows the relationship between $\Delta \boldsymbol{E}_3$ and ΔH at the moment when the amplitude of $\Delta \boldsymbol{E}_3$ is maximized for the period from ep$_3$ and ep$_3$+1 hour. We obtained the following equations for the bay disturbances.

$$\Delta E_{1,x}(\text{mV/km}) = -(0.34 \pm 0.01)\Delta H(\text{nT}),$$
$$\Delta E_{1,y}(\text{mV/km}) = -(2.18 \pm 0.09)\Delta H(\text{nT}). \tag{2.6}$$

The correlation coefficients are –0.83 and –0.83 for $\Delta E_{1,x}$ and $\Delta E_{1,y}$, respectively.

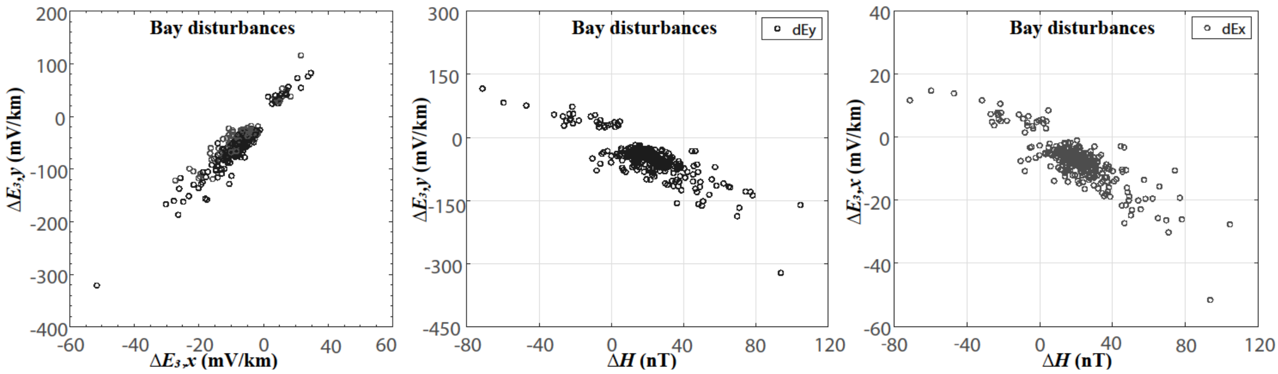

Figure 2.8 Same as Figure 2.4 except for the moment when the maximum value of $|\Delta E_3|$ took place for the bay disturbances.

2.3.4 Occurrence distribution of GIE

Figure 2.9 shows occurrence distributions for the SSC/SIs, the storm main phase, and the bay disturbances during 1996-2004. For the SSCs/SIs, we took the maximum $|\Delta E_1|$ for the period from ep1 to ep1+15 minutes. The largest value reaches 617 mV/km, which was recorded on 15 July 2000. For the storm main phase, the largest value reaches 210 mV/km on 20 November 2003. For the bay disturbances, the largest amplitude is 325 mV/km at 0946 UT on 10 November 2004. Note again that these values are all the largest ones for each event referred above. To illuminate the underlying tendency of GIE distribution caused by the three types of the geomagnetic disturbances in the solar cycle, we performed the generalized extreme value distribution (GEVD) (Kotz & Nadarajah, 2000). The probability density function for the GEVD with a location parameter μ, a scale parameter σ, and a shape parameter k ($\neq$ 0) is given by

$$y = f(x \mid k, \mu, \sigma) = \left(\frac{1}{\sigma}\right)\exp\left(-\left(1+k\frac{(x-\mu)}{\sigma}\right)^{-\frac{1}{k}}\right)\left(1+k\frac{(x-\mu)}{\sigma}\right)^{-1-\frac{1}{k}} \tag{2.7}$$

for $1+k\frac{(x-\mu)}{\sigma}>0$.

The results are shown by the red curves in Figure 2.9. We set the binning width of bars as 25 mV/km to avoid the statistical noise of the distribution. Parameters of the equation for 3 types of disturbances are presented in Figure 2.9.

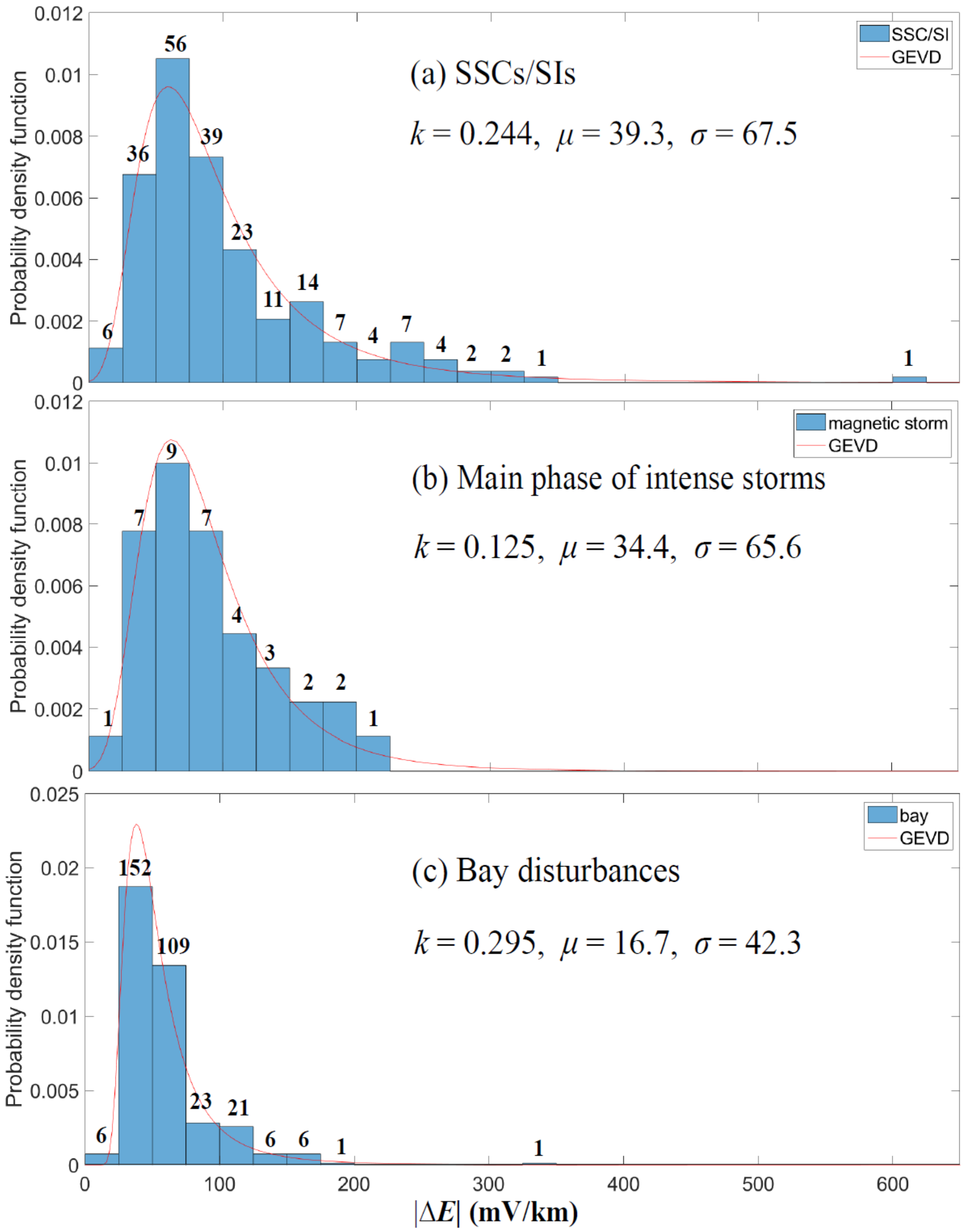

Figure 2.9 Histograms of the number of samples as a function of |ΔE|, distribution and GEVD fitting results for (a) the SSCs/SIs, (b) the storm main phase, and (c) the bay disturbances. The numerical figures above the bars indicate the number of occurrences. The left axis shows the probability density.

We predicted 10-year and 100-year values, which may help unveil the potential risk of GIC problems in the power grid in Japan. We obtained the return values in the GEVD by using the following equation:

$$x_T = \mu - \frac{\sigma}{k}\left(1 - \left[-\log\left(1 - \frac{1}{T}\right)\right]^{-k}\right) \text{ for } k \neq 0 \tag{2.8}$$

where x_T is called a return value, which is defined as a value that is expected to be equaled or exceeded on average once every interval of time T (with a probability of $1/T$). T refers to a return period. Following Woodroffe et al. (2016), we estimated 10-year and 100-year $|\Delta E|$ for the SSCs/SIs, the main phase of storms, and the bay disturbances. The results are presented in Table 2.2. The 10-year values of $|\Delta E|$ are 241.7, 204.9 and 177.4 mV/km for the SSCs/SIs, the main phase of storms, and the bay disturbances, respectively. The 100-year values are 612.3, 442.3 and 455.9 mV/km, respectively, but they may have some uncertainty because we used data obtained in 1996-2004. We will discuss these values later.

The largest GIE associated with the SSCs/SIs is 617 mV/km (ΔE_x of −125.7 mV/km and ΔE_y of −603.9 mV/km) in 1996-2004, which is nearly equal to the 100-year value as summarized in Table 2.2. For the storm main phase, the largest GIE in 1996-2004 is 210 mV/km (ΔE_x of 25.2 mV/km and ΔE_y of 208.9 mV/km), which is close to the 10-year value. For the bay disturbances, the largest GIE is 325 mV/km (ΔE_x of −51.6 mV/km and ΔE_y of −321.2 mV/km), which is close to the 10-year value.

Table 2.2 10-year and 100-year $|\Delta E|$ at KAK for SSCs/SIs, magnetic storms and bay disturbances.

Geomagnetic activity	10-year $\vert\Delta E\vert$ (mV/km)	100-year $\vert\Delta E\vert$ (mV/km)
SSCs/SIs	241.7	612.3
Main phase of storms	204.9	442.3
Bay disturbances	177.4	455.9

2.3.5 Validation of the empirical equations

We performed a case study to validate the applicability of the empirical equations. Figure 2.10 summarizes ΔH, ΔE_x, ΔE_y and $|\Delta E|$ observed at Kakioka for the magnetic storm of 20 April 2020. The SSC was recorded at 0230 UT on 20 April 2020, with the amplitude ΔH of 12 nT. Substituting ΔH of 12 nT into Eq. (2.3), we obtained ΔE_x and ΔE_y to be [−9, −8] mV/km and [−53, −50] mV/km, respectively. The numerical figures in the square brackets indicate the values obtain by the upper and lower limits of the 95% confidence levels of the slope of Eq. (2.3). These amplitudes are fairly consistent, but slightly larger than the observed ones shown in the second and third panels of Figure 2.10. Substituting ΔE_x and ΔE_y to Eq. (2.1), with the coefficients summarize in Table 2.1, we obtained GICs at SFS to be [−3.2, −3.1] A, which is about ~1.5 times larger than the observed GIC of −2 A in magnitude as shown in Figure 2e in Ebihara et al. (2021). During the SSC, the maximum amplitude of the GIC at STB and SFJ are less than 1 A, which also makes difficult to compare with the observations due to the offset values.

As for the storm main phase, we performed the same manner presented in Section 2.3.2. First, we removed short-lived spikes by applying a moving median method to extract the contribution from the ring current that varies relatively slowly. The smoothed values are indicated by the red lines in Figure 2.10. The smoothed values show plateaus, but we confirmed that they are not glitch in the calculation. The maximum value of the smoothed $|\Delta E|$ is found to take place at 1013 UT on 20 April 2020. At this moment, ΔH was −73 nT. Substituting ΔH of −73 nT into Eq. (2.4), we obtained $\Delta E_{1,x}$ and $\Delta E_{1,y}$ to be [7, 9] mV/km and [54, 70] mV/km, respectively. With Eq. (2.1), we obtained GIC for SFS to be ~ [1.8, 2.6] A. At this moment, the GIC observed at SFS is ~2 A as shown in Figure 2e in Ebihara et al. (2021), which is consistent with this estimate.

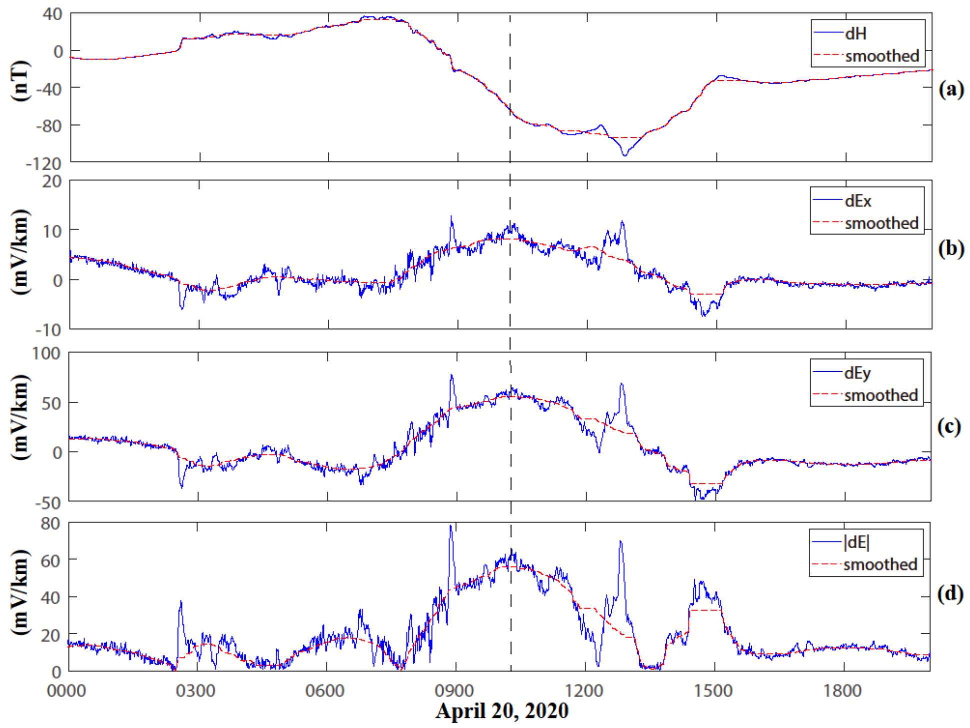

Figure 2.10 From the top, ΔH, ΔE_x, ΔE_y, and $|\Delta E|$ for the magnetic storm on 20 April 2020. The vertical line indicates the moment when the smoothed $|\Delta E|$ reaches the maximum during the storm main phase. The red lines indicate the values smoothed by the moving median method.

Next, we focus on the magnetic storm that took place on 13-14 March 1989, which is the largest one in terms of the minimum *Dst* value since 1957. During the magnetic storm, the minimum ΔH is ≈ −597 nT (which is the averaged value between 0018 and 0028 UT on 14 March 1989) at Kakioka. Substituting ΔH of −597 nT into Eq. (2.4) and (2.1), we obtained the GIC values at SFS, STB and SFJ to be [20, 28], [−5, −6] and [0, 2] A, respectively. The maximum GIC values obtained based on the convolution method are ≈ 11, −3, and −2 A, respectively, at 0025 UT on 14 March 1989 (Ebihara et al., 2021). Note that the GICs were not measured at SFS, STB and SFJ during the magnetic storm. For SFS and STB, the amplitude of the estimated GICs are about 2 times larger than that obtained by the convolution method. The GICs at SFJ are not well reproduced. One of the plausible reasons is that the GICs at SFJ is more sensitive to ΔE_x, likely depending on ΔD (geomagnetically east-west component of the magnetic disturbance), rather than ΔH. Inhomogeneous ground conductivity and the network topology can also make the difference (Nakamura et al., 2018).

We recognize that the empirical equations, (2.3), (2.4) and (2.6) give estimates that are less accurate than those obtained by a convolution method (Love & Swidinsky, 2014). For the magnetic storm of 20 April 2020, the estimated GICs are consistent with the observed ones. For the magnetic storm of 13-14 March 1989, the estimated GICs are about 2 times larger in magnitude than obtained by the convolution method. The temporal variations of the SSCs/SIs and the storm main phase vary with magnetic storms, and the estimated GICs do not necessarily match the precise values. However, we believe that these empirical equations are useful for evaluating extreme values of GIEs and GICs for which temporal variations of the geomagnetic field are not provided.

2.4 Discussion and Summary

For the SSCs/SIs, $\Delta E_{1,x}$ and $\Delta E_{1,y}$ are shown to be correlated fairly well with ΔH. This might be consistent with the statistical studies showing that $\Delta H/\Delta T$ is well correlated with ΔH, where ΔT is the rise time of SSCs/SIs (Araki et al., 2004). Similar tendency is also reported by Mayaud (1975). Araki et al. (2004) pointed out that for the large amplitude of SSCs/SIs, ΔH increases rapidly. Wang et al. (2006) showed that the rise time of SSCs decreases with increasing the solar wind speed. The amplitude of the ΔH associated with SSCs/SIs is also known to be proportional to the square root of the solar wind dynamic pressure, that is, being proportional to the solar wind speed (Siscoe et al., 1968; Ogilvie et al., 1968). The global magnetohydrodynamics (MHD) simulation also supports these observational facts (Kubota et al., 2015). These observational and simulation results can explain the fact that $\Delta H/\Delta T$ is well correlated with ΔH. The physical mechanism that determines the linear relationship is not unclear, and is expected to be complicated because of the transient phenomena involving the magnetosphere-ionosphere coupling processes (Araki, 1994; Piersanti & Villante, 2016) as well as frequency dependent response of ground (Fujii et al., 2015). If ΔE is simply proportional to $\partial B/\partial t$, ΔE would also be proportional to $\Delta H/\Delta T$. Of course, according to the convolution theory (Cagniard, 1953; Love & Swidinsky, 2014), ΔE is not necessarily proportional to $\partial B/\partial t$.

Yokoyama & Kamide (1997) investigated more than 300 magnetic storms, and found that the duration of the storm main phase (ΔT) does not increase linearly with the peak *Dst* value (ΔDst). However, $|\Delta Dst|/\Delta T$ does intend to increase with $|\Delta Dst|$, that is, large magnetic storms develop rapidly. This might explain, in part, the quasi-linear relationship between ΔE and ΔH.

McPherron & Chu (2018) calculated the probability density of the duration of the bay disturbances (magnetic positive bays) that took place from 1981 to 2012. The peak of the probability density ranges from ~32 for small bays to ~45 minutes for large bays. Their results indicate that the duration does not depend significantly on the size of the bays. If so, the amplitude of $\partial B/\partial t$ would be roughly proportional to the maximum value of ΔH.

On the basis of the magnetic field data obtained between 1981 and 2011, Woodroffe et al. (2016) showed that the median values of the electric field calculated from the magnetic field are ~72 mV/km, ~166 mV/km and ~245 mV/km at the magnetic latitude of 20°-30° for the ranges $-200 < Dst \leq -100$ nT, $-300 < Dst \leq -200$ nT and $Dst \leq -300$ nT, respectively. The median values of $|\Delta E|$ observed at Kakioka (27.8° magnetic latitude) for the range $Dst < -100$ nT is 80 mV/km for the SSCs/SIs and 78 mV/km for the storm main phase as shown in Figure 2.9. These median values are reasonable in comparison with those obtained by Woodroffe et al. (2016). It is interesting to note that the median value for the SSCs/SIs is close to that for the storm main phase. This implies that the SSCs/SIs and the storm main phase are equally of importance in the electric field. Although Woodroffe et al. (2016) did not distinguish the SSCs/SIs and the storm main phase, their results are, of course, valid in the evaluation of the median values for the magnetic storms (including SSCs/SIs).

It is of importance to estimate the GIC values for extreme events. For example, the largest amplitude of the ΔH disturbance associated with the SSCs/SIs is >273 nT at Kakioka, recorded on 24 March 1940 (Araki, 2014). Substituting ΔH of 273 nT to Eq. (2.3), we obtained $\Delta E_{1,x}$ and $\Delta E_{1,y}$ to be [−213, −186] mV/km and [−1209, −1144] mV/km, respectively. The GICs that could flow at SFS, STB and SFJ are estimated to be [−55, −53], [12, 12], and [7, 13] A, respectively.

Kataoka (2013) showed the probability of extreme storm-time disturbances of ΔH at Kakioka. Moriña et al. (2019) also performed statistical analysis of the *Dst* index, and provided the probability. For example, the occurrence frequency for the threshold level of −800 nT is 1.37 per 1,000 years. Their occurrence probability does not provide the temporal variation of ΔH. However, using Eqs. (2.3), (2.4) and (2.6), we can estimate GIEs and GICs without knowing the temporal variation, which will be useful for tolerance evaluation of electric facilities of the power grid. Vasyliunas (2011) theoretically estimated the upper limit of the storm-time ring current, and suggested the minimum *Dst* value of −2500 nT. It would be reasonable to regard ΔDst as ΔH at Kakioka for the purpose of evaluating the extreme value as a zeroth order approximation because Kakioka is one of the *Dst* stations. Substituting ΔH of −2500 nT to Eq. (2.4), we obtained $\Delta E_{1,x}$ and $\Delta E_{1,y}$ to be [250, 300] mV/km and [1850, 2400] mV/km, respectively. With Eq. (2.1), we calculated GICs flowing at SFS, STB and SFJ to be [88, 117], [−20, −26] and [2, 10] A, respectively.

One of the most severe magnetic storms ever observed is the Carrington storm that occurred in 2 September 1859 (Tsurutani, 2003; Siscoe et al., 2006). At Bombay, the minimum ΔH was recorded to be ≈ −1600 nT (Tsurutani, 2003). Following Sugiura (1991, WDC Kyoto, http://wdc.kugi.kyoto-u.ac.jp/dstdir/dst2/onDstindex.html), we corrected the magnetic record at Colaba by removing the possible contribution from the magnetic latitude effect. The corrected ΔH for Kakioka is ≈ −1450 nT (= −1600 nT×cos λ_K/cos λ_C, where λ_K and λ_C are the magnetic latitudes at Kakioka (≈ 27°) and that at Colaba (≈ 10°), respectively). Substituting ΔH of −1450 nT into Eqs. (2.4) and (2.1), GICs flowing at SFS, STB and SFJ are estimated to be [51, 67], [−11, −15], and [1, 6] A, respectively. Ebihara et al., (2021) used the time-series data of the magnetic field observed at Bombay on 2 September 1859, and estimated GIEs at Kakioka by taking convolution of the magnetic field. With Eq. (2.1), Ebihara et al., (2021) obtained the maximum GIC values to be [59, 119], [−27, −13] and [−46, 8] A at SFS, STB and SFJ, respectively.

According to the Kakioka observatory, the maximum amplitude of the bay disturbances is ~100 nT at Kakioka since 1957. Substituting ΔH of 100 nT into Eqs. (2.6) and (2.1), we estimated GICs flowing at SFS, STB and SFJ to be [−11, −10], [2.4, 2.2], and [0.7, 0.9] A, respectively.

SIs and bay disturbances often occur during the magnetic storms as shown in Figure 2.1. At Kakioka, ΔE_y tends to be positive during the storm main phase, while it decreases to negative values during the storm recovery phase as shown in Figure 2.1. On average, both the SSCs/SIs and the bay disturbances give rise to negative excursions of ΔE_y as shown in Figure 2.1 and Figure 2.7. It is expected from these results that the magnitude of ΔE_y would be amplified (negative deflection) when the SSCs/SIs and/or the bay disturbances occur during the storm recovery phase. An exception is a negative SI, which is caused by the sudden decrease in the solar wind dynamic pressure. When the negative SI occurs during the storm main phase, the amplitude of ΔE_y is also amplified (positive deflection) as shown in Figure 2.1. On average, E_y shows a broad, positive excursion from ~04 UT to ~13 UT on 19 October 1998. This interval is a part of the main phase of the storm in October 1998. A negative SI, occurred at ~05 UT on 19 October, resulting in the further increase in E_y.

It is possible that extreme SIs occur during an extreme magnetic storm. Tsurutani & Lakhina (2014) pointed out that if a second interplanetary shock arrives at Earth while a magnetic storm is ongoing, this type of the solar wind condition is geoeffective. The large-amplitude GICs, as high as 129 A, were recorded in the Japanese power grid on 30 October 2003 (Ministry of Economy, Trade and Industry of Japan, 2015). Ebihara et al. (2021) suggested that the large-amplitude GICs recorded on 30 October 2003 could result from the arrival of an interplanetary shock in the course of the recovery phase of the intense magnetic storm of 28-30 October 2003, known as the Halloween event. It is also possible that bay disturbances occur during an extreme magnetic storm. Hajra et al. (2016) showed that extreme substorms (supersubstorms) with minimum SML index being less than −2500 nT often occur during the storm main and recovery phases. The SML index is an extension of the AL index, representing the magnitude of the westward ionospheric current at high latitudes (Newell & Gjerloev, 2011). The amplitude of the bay disturbances is not necessarily correlated with the amplitude of the SML index for the supersubstorms since the mid-latitude bay disturbances are primarily caused by the field-aligned currents whereas the decrease in the SML index is primarily caused by the ionospheric Hall current depending on the ionospheric electric field and the conductivity. Further studies are needed to investigate the relationship between the magnetic storms and the substorms in terms of GICs. To assess the worst values of GICs flowing at low and mid latitudes, one should take into consideration the combination among the magnetic storms, the SIs and the bay disturbances.

According to the documents published by the North American Electric Reliability Corporation (NERC, 2016), the effective GIC of 75 A (225 A per 3 phases) is set to be a conservative screening criterion for thermal impact assessments of transformers. These GICs estimated above are probably less than the screening criterion for these particular substations, that is, SFS, STB and SFJ. If GIC data is available for the other substations and generators, the same calculation is applicable to estimate the GICs for extreme events. However, it is almost unrealistic to measure the GICs at all the substations and generators in a nation. An alternative way is to calculate numerically the GIE distribution in Japan (Püthe et al., 2014; Fujita et al., 2018; Nakamura et al., 2018), and to solve the equation of continuity of the current flowing in the grid (Lehtinen & Pirjola, 1985). Eventually, the coefficients a, b and c of Eq. (2.1) would be obtained for all the facilities of the power grid. If the solar wind conditions are reasonably predicted by simulations (e.g., Odstrcil, 2003; Shiota & Kataoka, 2016) in a real time manner, the maximum $|Dst|$ values would be calculated immediately with the aid of an empirical model (e.g., Burton et al., 1975). Substituting the estimated $|Dst|$ values to Eqs. (2.3) and (2.4), one can estimate immediately the maximum GIC values at the substations/generators at which the coefficients a, b and c of Eq. (2.1) are known. We will verify the validity of this scheme for the real-time prediction of GICs at mid and low latitudes in the future study.

Chapter 3 Nighttime Geomagnetic Response to Jumps of Solar Wind Dynamic Pressure

3.1 Introduction

Geomagnetically induced currents (GICs) generated by large geomagnetic disturbances impact on the power system (Pirjola, 2002). One of the largest magnetic storms in the twentieth century caused a well-known, long-lasting blackout in Québec in Canada in 1989 (Allen et al., 1989). However, many exact details of this event are not widely known, not only the storm itself but also the irreversible effects on power systems (Boteler, 2019). This blackout took place in Québec in the post-midnight sector, starting at 0745 UT on 13 March 1989. According to many previous studies (Boteler, 2019 and the references therein), we know that this power outage occurred in a large magnetic storm, especially in the course of a sudden commencement (SC) starting at 0743 UT on 13 March 1989.

The SC is an impulse response of the magnetosphere–ionosphere system caused by a sudden change in solar wind dynamic pressure (Araki, 1994; Kubota et al., 2015). The development of satellite observations revealed that a sudden increase of dynamic pressure is associated with the interplanetary shock or discontinuity (Curto et al., 2007). Usually, the SC has two more detailed classifications, SSCs (storm sudden commencements) and SIs (sudden impulses). The difference is that the former is followed by a geomagnetic storm, whereas the latter is not. The ground magnetic signature of the SC usually exhibits a sudden increase in the *H*-component (the component of the disturbance field along the horizontal direction of the quiet-day magnetic field) at mid- and low-latitudes (DL) as well as a bipolar variation in the *H* trace at auroral latitudes (DP) (Araki, 1994). Araki summarized the waveform of the SC at different latitudes from the equator to the auroral region on the dayside, and nightside equatorial latitudes according to the observations. Figure 11 in Araki (1994) described the dependence of the decomposed fields upon local time and latitude schematically. According to the physical model proposed by Araki (1994), the DP disturbance is composed of two successive impulses, called the preliminary and main impulse (PI and MI), respectively. Perturbation of the *H*-component (ΔH) caused by the MI usually lasts longer than that of the PI. The polarity of ΔH on the dayside associated with the DP is opposite in the morning and afternoon sector. Positive ΔH is often observed at mid- and low-latitudes due to the domination of the DL. The various characteristics of SCs have been studied over the past decades. Little attention, however, has been paid to the effects on the nightside, at low-latitudes (Araki et al., 2006) and at high latitudes (Zhou & Lühr, 2022). Boudouridis et al. (2011) examined the response of the dayside and nightside ionospheric convection to sharp solar wind dynamic pressure enhancements combined with case studies and statistical analysis.

SC-associated rapid magnetic field variations are considered as one of the major sources of large-amplitude geoelectric fields at Kakioka, Japan, which is strongly related to GICs (Zhang & Ebihara, 2022). Zhang et al. (2015) indicated clearly that, in China, GICs due to the SC are 2–3 times larger than those due to the storm main phase of the magnetic storm on 17 March 2015. Furthermore, Carter et al. (2016) discriminated between the magnetospheric contribution and the ionospheric contribution to the disturbance, and discussed the impact on GICs as well. They mentioned that the majority of stations observe a sudden increase in B_x (the northward component of the magnetic field), corresponding to an increase in the auroral electrojet in the eastward direction at the moment of SC, while a high-latitude station actually observes the opposite. The magnetic perturbations at mid-latitude and equatorial regions are most caused by magnetospheric currents, namely the DL component. In the auroral regions, the horizontal perturbations are primarily caused by currents flowing in the ionosphere, namely the DP component. The DL component is large on the dayside, while more processes arising from the magnetotail plasma sheet, which complicate the relationship between the solar wind and the magnetosphere-ionosphere coupling processes, are also involved on the nightside (Shidi et al., 2022).

Although Carter et al. (2016) investigated the magnetic field variations from high to equatorial regions, it is not easy to imagine what happens in the much larger magnetosphere from the limited observations on the ground (Curto et al., 2007). The obtainment of the global picture for the transient response of the SC is also restricted by limited geomagnetic stations. Madelaire et al. (2022), whose goal is to isolate the influence of dipole tilt and IMF (interplanetary magnetic field) orientation on SC development, find very few instances with both adequate in-situ data and observations on ground. Performing high-resolution global MHD simulations is proved to be a useful tool to study the reproduction of the geomagnetic disturbances in recent years. For example, Fujita et al. (2003a, 2003b) investigated the PI- (preliminary impulse) and MI- (main impulse) associated variations at auroral latitudes by performing a global MHD simulation that takes into consideration the magnetosphere-ionosphere coupling under a northward IMF condition. Kubota et al. (2015) also investigated magnetospheric response of the PI to large and sudden increases of solar wind dynamic pressure by using MHD simulation. Furthermore, Tanaka et al. (2020) emphasized the importance of conducting the comparison between simulation results and observations, to verify the validity of the simulation. Shidi et al. (2022) performed global MHD simulations for 122 geomagnetic storms, and compared the ground magnetic field perturbations with magnetometer station data provided by a large-scale database of magnetic disturbances, SuperMAG (Gjerloev, 2012) (https://supermag.jhuapl.edu/). Kikuchi et al. (2022) attempted to obtain a consistent understanding of observation, theoretical model, and simulation with the geomagnetic sudden commencement (SC) observed in the morning and afternoon at high- and mid-latitudes in the Northern and Southern Hemispheres and at the noontime equator.

Tanaka et al. (2020) highlighted that the magnetic field variations could be accurately evaluated from Biot-Savart's law with the current distribution obtained by the global MHD simulation. They noted that in the auroral region, the Hall current effect far prevails over other currents, which determines the AU/AL indices. Yu et al. (2010) also found that at high latitudes, the Hall current dominates, since FACs and Pedersen current partly cancel each other, though not completely. In our MHD simulations, Fukushima's theorem (Fukushima, 1976, 1971) is violated due to the uneven ionospheric conductivity though, we still find in the northward geomagnetic response that the contribution from the Hall current is dominant at high latitudes on the nightside as mentioned below. Thus, in this chapter we focus on the effects of the ionospheric Hall current when calculating the ground magnetic fluctuations (northward component) in the region of interest using Biot-Savart's law.

The aim of this study is to understand the large-amplitude magnetic fields associated with SCs, especially on the nightside at high latitudes, and the possible cause of the Québec blackout. We performed the MHD simulations with different solar wind conditions (velocity and density), and compared the results with the observed geomagnetic data provided by Canadian magnetic observatories and IMAGE magnetometer network (Tanskanen, 2009). We focus on the DP-like disturbances at high magnetic latitudes (MLATs). The resultant geoelectric variations are also computed by the convolution method with an assumed ground conductivity.

3.2 Geomagnetic Data

We used 1-min resolution geomagnetic field data recorded at 12 magnetic observatories in Canada (see the geographic distribution in Figure 3.1). The 12 observatories provided the geomagnetic data since 1989 or earlier. Table 3.1 provides the detailed information including the geomagnetic coordinates. In the ionospheric domain, the *x*- and *y*-components refer to the northward and eastward components of the geomagnetic field, respectively.

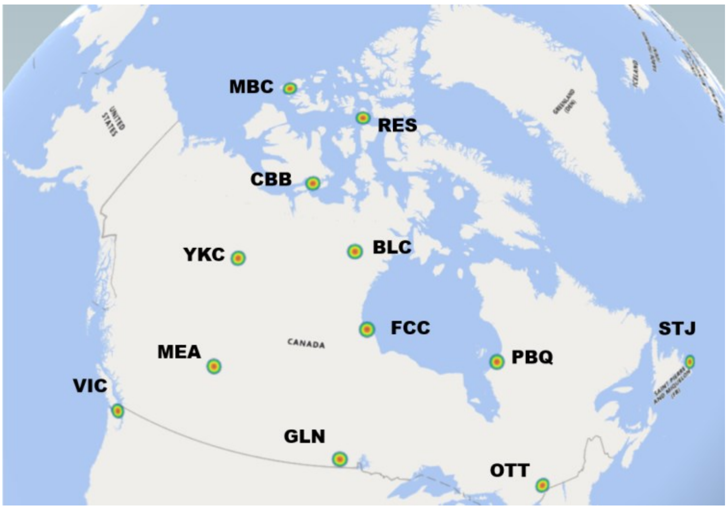

Figure 3.1 12 observatories marked on the map.

Table 3.1 Observatories information.

Name	Code	Geographic latitude (°N)	Geographic longitude (°E)	Geomagnetic latitude (°N)*[1]	Geomagnetic longitude (°W)*[1]	UT at 00 MLT*[2]
Mould Bay	MBC	76.3	240.6	80.0	90.9	9.81
Resolute	RES	74.7	265.1	82.6	51.5	6.94
Cambridge Bay	CBB	69.1	255.0	76.2	53.7	7.69
Baker Lake	BLC	64.3	264.0	72.7	35.5	6.71
Yellowknife	YKC	62.5	245.5	68.6	58.2	8.30
Fort Churchill	FCC	58.8	265.9	67.4	29.7	6.48
Poste de-la-Baleine	PBQ	55.3	282.3	64.7	6.87	5.06
Meanook	MEA	54.6	246.7	61.2	51.9	8.04
Glenlea	GLN	49.6	262.9	58.1	30.6	6.67
Victoria	VIC	48.5	236.6	53.8	60.8	8.75
St John's	STJ	47.6	307.3	56.4	24.7(°E)	3.08
Ottwa	OTT	45.4	284.4	54.9	3.59	4.92

*[1]according to IGRF-12 (Thébault et al. 2015).
*[2]see details in https://omniweb.gsfc.nasa.gov/vitmo/cgm.html.

The 10-second resolution geomagnetic data and stack plot for the SC event on 15 May 1997 are provided by IMAGE magnetometer network (Tanskanen, 2009). The observatories are located in the Fenno-Scandian sector from subauroral to polar cap regions. The MLT in that sector is about 2 hours ahead of the Universal Time (UT). For more details of the data and plot, check the webpage of https://space.fmi.fi/image/www/index.php?page=user_defined.

3.3 MHD Simulation and Methodology

3.3.1 Simulation settings

We used the global MHD simulation code REPPU (the third version) developed by T. Tanaka and details of the code are explained in his papers (Tanaka, 1994, 1995, 2015). The coordinate system in the magnetospheric domain is set as that the x-axis points sunward, the z-axis points north, and the y-axis is chosen to satisfy the right-handed system correspondingly. The outer boundary conditions correspond to the solar wind on the upstream side at x = 40 R_E and a zero gradient on the downstream side at x = -200 R_E. The simulation is started from a quasi-stationary state with solar wind parameters of N_{sw} = 5/cc, V_{sw} = 400 km/s, B_y = 0 nT, B_z = 3 nT (northward IMF) for the first 120 min. For the northward case, we increased the solar wind velocity and/or the solar wind density as a step function at x = 40 R_E at the elapsed time of 120 min (T = 120 min). The IMF was kept constant. For the southward IMF case, we changed IMF B_z to –3 nT at T = 120 min. We increased the solar wind velocity and/or the solar wind density at T = 240 min. We use the notation Run-*nmz* to represent the conditions, where "*n*" and "*m*" (both from 0 to 4) mark the runs with different jumps of the velocity and/or density respectively, as summarized in Table 3.2. "*z*" indicates the polarity of IMF B_z, in which "*n*" stands for the northward IMF case and "*s*" stands for the southward IMF case. For example, Run-31n means the solar wind with a jump of velocity from 400 km/s to 1000 km/s, and density from 5/cc to 10/cc for the northward IMF case.

Table 3.2 Simulation settings.

Number	Solar wind velocity (km/s) *n*	Solar wind density (/cc) *m*
0	400	5
1	600	10
2	800	20
3	1000	50
4	1200	100

3.3.2 Calculation of geomagnetic and geoelectric field

In this section, we mainly showed the result of the Biot-Savart integral over the Hall current associated with a SC, since we compared the contributions to the nighttime B_x disturbances from the Hall current, the Pedersen current and the FAC as shown in the Appendix, and the Hall current is dominant at high latitudes. Tanaka et al. (2020) also pointed out that the Hall current effect far prevails over other currents and determines the AU/AL indices in the auroral region. Thus, we present simulated magnetic variations at 50-90 MLATs in the following sections. Zhang et al. (2012) used the ionospheric current to calculate the geomagnetic perturbations using Biot-Savart's law with the integration domain limited in 1000 km both in latitudinal and longitudinal directions. This is shown to be adequate for reproducing horizontal magnetic perturbations in the auroral region (Yiqun Yu & Ridley, 2008). We calculated the magnetic perturbations caused by Hall currents as follows (the contributions from Pedersen currents and FACs could be obtained similarly).

First, in the simulation, the height-integrated Hall current density vector $\mathbf{J}_H$ is given at each grid point in the ionosphere, which is a function of the MLAT and the magnetic local time (MLT). The height-integrated Hall current is given by

$$\mathbf{J}_H = \Sigma_H \frac{\mathbf{B} \times \mathbf{E}}{B}, \tag{3.1}$$

where Σ_H, $\mathbf{B}$ and $\mathbf{E}$ are the height-integrated Hall conductivity, the magnetic field, and the electric field, respectively. The electric field is given by solving the partial differential equation for given field-aligned current and ionospheric conductivity so as to satisfy the current continuity in the ionosphere (inductive effects are ignored). The ionospheric conductivity is determined in accordance with three sources. The first source is the solar EUV (extreme ultraviolet), which is described as a functional form depending on the solar zenith angle. The second source is the contribution from precipitating particles likely associated with discrete aurorae, and the third one is the contribution from the precipitating particles likely associated with diffuse aurorae (Ebihara et al. 2014). In the simulation, we increased the ionospheric conductivity where the upward FAC flows to represent electron precipitation. The detail of the calculation of the electric field and the conductivity is explained by Tanaka (2015) and Ebihara et al. (2014). In the calculation of the ionospheric conductivity, current-voltage relation known as the Knight relation is not considered.

Then, based on the Biot-Savart's law, the magnetic field $\mathbf{B}$ produced at position $\mathbf{r}$ generated by the ionospheric current could be given by the following equation (Zhang et al. 2013),

$$\mathbf{B}(\mathbf{r}) = \frac{\mu_0}{4\pi} \int_S \frac{\mathbf{J}(\mathbf{r}') \times (\mathbf{r} - \mathbf{r}')}{\left|\mathbf{r} - \mathbf{r}'\right|^3} dS, \tag{3.2}$$

where $\mathbf{J}(\mathbf{r}')$ is the ionospheric Hall current flowing in a thin shell in the ionosphere, $\mathbf{r}'$ denotes the position of the current element, S is the area of a sphere at 100 km altitude, and μ_0 is the magnetic permeability of free space. The surface integral was conducted over the region defined within 500 km from the location of interest ($\mathbf{r}$) on the ground.

With respect to the geoelectric field variations, we use the equation based on the convolution theory (Cagniard, 1953; Love & Swidinsky, 2014; Ebihara et al. 2021) with an assumed ground conductivity to calculate as follows,

$$\mathbf{CE(t)} = \frac{1}{\sqrt{\pi\mu_0\sigma}} \int_0^t \frac{\partial \mathbf{B}}{\partial t} \frac{d\theta}{\sqrt{t-\theta}}, \tag{3.3}$$

where $\mathbf{C} = \begin{pmatrix} 0 & -1 \\ 1 & 0 \end{pmatrix}$ is a rotation matrix that comes from the curl operator and is only two-dimensional (Love & Swidinsky, 2014), t is the length of time series of interest, θ is the time interval between two adjacent points in the series, μ_0 is the magnetic constant and the assumed ground conductivity σ = 0.001 S/m, as the value used in Model 1 (*Uniform Earth*) used by (Boteler, 2015). Though this model of the ground conductivity may be simple, it would be fast and useful for evaluating the relative variation of the geoelectric field in response to the change in the solar wind conditions.

3.4 Observations and Simulation Results

3.4.1 Observed geomagnetic disturbances during SCs

Figure 3.2 shows the B_x disturbances observed by IMAGE magnetometer network on 15 May 1997. The SC took place at 0159 UT defined by Kakioka Observatory (https://www.kakioka-jma.go.jp/obsdata/dataviewer/en). The jump of the solar wind parameters for the SC is ~320 to 360 km/s for velocity, ~20 to 30 /cc for density and IMF B_z is almost zero at the onset, according to https://omniweb.gsfc.nasa.gov/form/omni_min_def.html. We noticed the positive (northward) variations about 2 minutes after the onset (0159 UT) observed at BJN and the stations located at higher latitudes, and negative (southward) variations at SOR and the stations at lower latitudes. The small perturbations observed at OUJ, HAN and NUR are considered as the effect of DL component. As shown below, we observed the same tendency in the geomagnetic disturbances at high latitudes during the Québec blackout, whose solar wind condition is unknown.

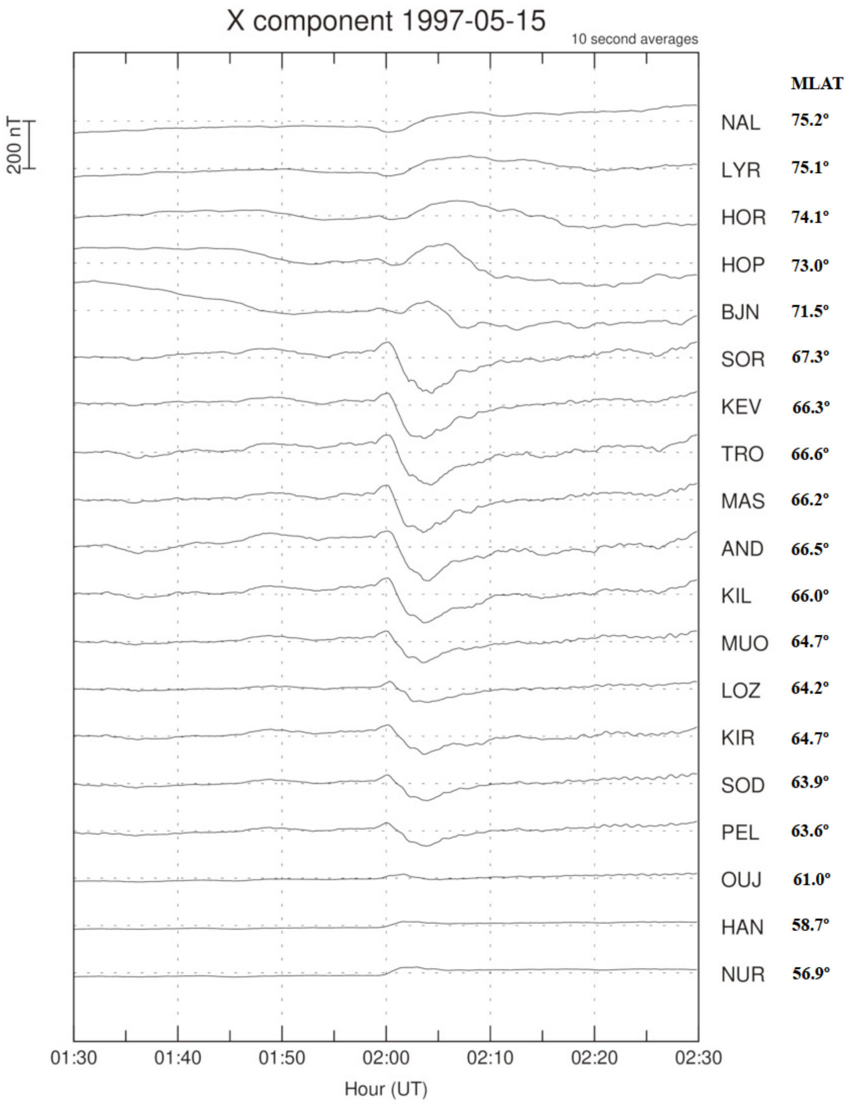

Figure 3.2 Stack plot of B_x taken at 19 stations of IMAGE. The plots are sorted by the magnetic latitude from high (top) to low (bottom) latitudes. The SC took place at 0159 UT on 15 May 1997. The distance between ticks in the vertical axis corresponds to 200 nT.

Figure 3.3 shows the northward component of the magnetic perturbations B_x observed in Canada on 13 March 1989. There is a sharp change in B_x around 0743 UT, which is considered to be an SC (Boteler, 2019). We may find the tendency that B_x shows positive changes at FCC and higher latitudes, and negative changes at PBQ and lower latitudes instead. This implies that an eastward current flows at higher latitudes, and a westward current flows at lower latitudes in the post-midnight sector. The amplitude of the negative disturbances reaches ≈ 1,800 nT, which is larger than that of positive ones. The blackout took place at MLAT ≈ 60° (see in Table A1 of Boteler, 2019). Thus, the blackout is supposed to be related to the negative (southward) perturbations after the SC. The tendency of the magnetic disturbance is the same as that observed on 15 May 1997 as shown in Figure 3.2. The major difference is the amplitude of the disturbance.

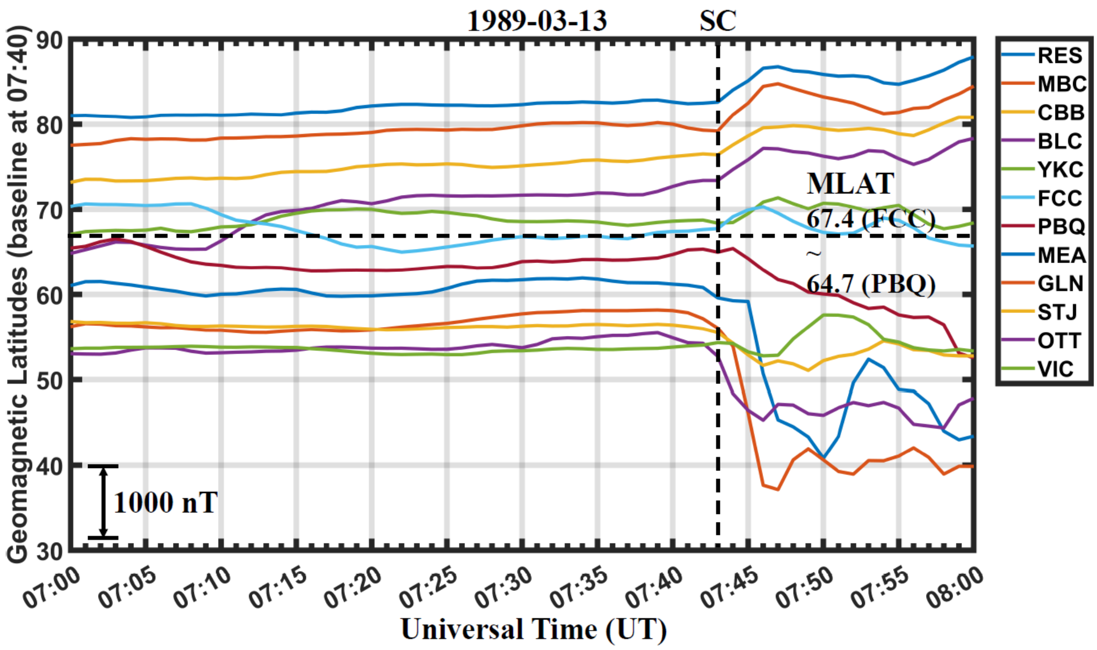

Figure 3.3 Stack plot of B_x taken at 12 stations in Canada sorted by MLATs. The base line of B_x is taken at 0740 UT on 13 March 1989. The distance between ticks in the vertical axis corresponds to 1000 nT.

3.4.2 Simulation results

3.4.2.1 Geomagnetic disturbances

Figure 3.4 shows the stack plot of the simulated B_x from 56 MLAT to 80 MLAT at 03 MLT for Run-12n (400 to 600 km/s for velocity, 5 to 20 /cc for density, northward IMF). Compared to Figure 3.2, we could find that the distribution of the B_x disturbances is quite similar with the observation. At high latitudes (70-80 MLAT), negative disturbances are followed by the positive disturbances, which increase slightly with the decrease of MLATs; the plot for the location at MLAT=68 seems to be a dividing line, showing the conversion of the waveform; and the new type of the waveform, at 66 MLAT, starts with a small increase then decreases largely. This pattern appears in the waveforms of these stations similarly, including from SOR to PEL (about 67.3 ~ 63.6 MLAT) in the name list in Figure 3.2, while the magnitude is getting smaller. The small perturbations at lower latitudes observed at OUJ, HAN and NUR, considered as the effect of DL component, are not clearly visible in Figure 3.4. Although, the jump of the solar wind parameters is not the same, we still observed the same tendency of the distribution of B_x in the simulation, as shown in both real SC events in 1997 (Figure 3.2) and 1989 (Figure 3.3).

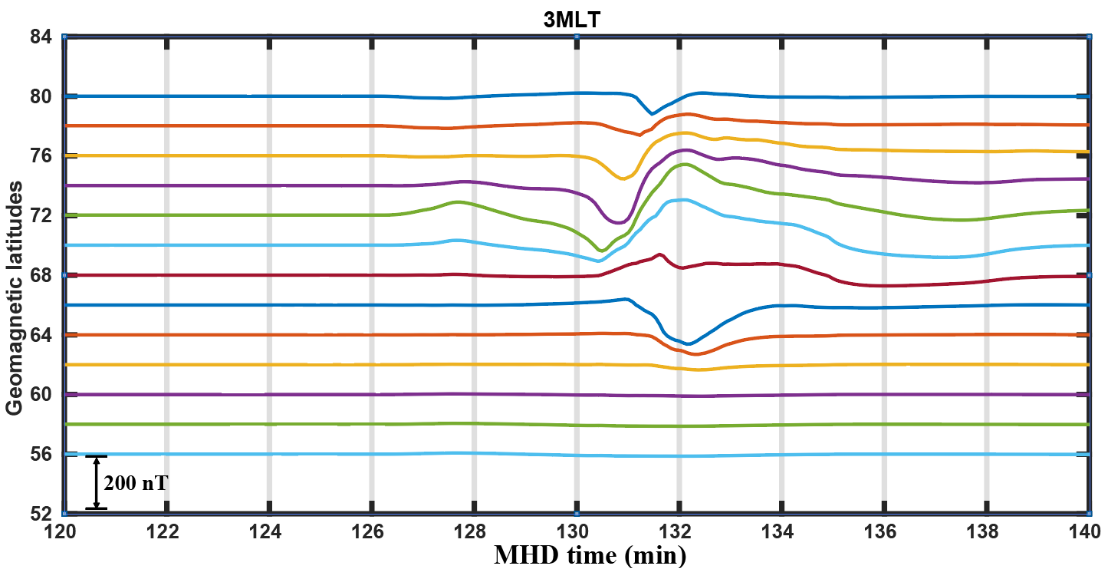

Figure 3.4 Stack plot B_x of Run-12n (northward IMF, solar wind velocity 600 km/s, and density 20 /cc), along MLATs at 0300 MLT. The distance between ticks in the vertical axis corresponds to 200 nT.

Figure 3.5 shows the stack plot of the simulated B_x from 56 MLAT to 80 MLAT at 03 MLT for different solar wind conditions. The simulation results for Run-33n, Run-30n, Run-33s and Run-30s are provided (see the naming of runs in Section 3.3.1). For these runs, the solar wind velocity was increased from 400 km/s to 1,000 km/s. For Run-33n and Run-33s, the solar wind density was increased from 5/cc to 50/cc, whereas for Run-30n and Run-30s, the solar wind density remained constant to be 5/cc. In addition, the runs ending in "n" correspond to northward IMF cases, and "s" to southward ones.

For Run-33n (Figure 3.5a), B_x shows a positive excursion at 74-80 MLAT, whereas it shows a decrease, followed by an increase 66-72 MLAT after $T = \approx 125$ min. At 56-64 MLAT, B_x shows a negative excursion.

For Run-30n (Figure 3.5b), the solar wind velocity was increased from 400 km/s to 1,000 km/s, whereas the solar wind density remained constant at 5/cc. Around T = 129 min, B_x increases at ≥ 68 MLAT except for a small negative excursion. The small negative excursion propagates to high latitudes with time, which is not clearly seen in Run-33n (Figure 3.5a). At < 68 MLAT, the disturbances become negative.

Run-33s (Figure 3.5c) is the same as Run-33n (Figure 3.5a) except for the southward IMF. The southward turning of IMF took place at T = 240 min at x = 40 R_E. Large negative excursion appears after T = 245 min at 70 MLAT and lower latitudes. At < 60 MLAT, the amplitude of the negative excursion is small.

Run-30s (Figure 3.5d) is the same as Run-30n (Figure 3.5b) except for the southward IMF. After T = 246 min, B_x shows a positive excursion at ≥ 72 MLAT, whereas it shows a negative excursion at < 72 MLAT. Compared to Run-33s (Figure 3.5c), we find that the density of the solar wind affects the time scale of the disturbance. We do not know the reason, and will investigate the dependence on the solar wind density in future.

The amplitude of the negative excursion is larger for the southward IMF case than for the northward case. The intensity of the FACs associated with the negative excursion is almost in the same range for the southward and northward case, that is, the FACs are almost independent of the polarity of IMF B_z. However, the ionospheric electric field and/or conductivity is somewhat larger for the southward case (at different locations), resulting in the intensification of the ionospheric Hall current and the amplitude of the negative excursion. As stated in Section 3.3.2, there are three sources determining the ionospheric conductivity. Among of them, the evolution of plasma pressure owns a similar variation with that of the conductivity as a function of MLAT along the longitude at MLT = 3. The upward FACs also have some impact on the variation. Considering this, we conducted the controlled simulations in which the plasma pressure would have no effect on the intensity of the ionospheric conductivity. This time the conductivity increases sharply with the enhancement of the upward FAC, while the larger B_x disturbances for southward IMF cases are not found, which may imply the significance of the contribution from the plasma pressure. In the global MHD simulation, the ionospheric conductivity associated with diffuse aurora is estimated from the plasma pressure (Tanaka et al. 2017). The results from the controlling simulation suggest that the diffuse aurora may have some impacts on the evolution of the MI-associated FACs, but this topic is beyond the scope of this chapter. Furthermore, the northward cases generated some large negative disturbances before the positive disturbances, especially for Run-33n case at 66 and 68 MLAT, which is not seen in the southward cases.

A common feature among these results is that the negative disturbance appears just lower than a certain latitude and the positive one appears higher than this latitude when the MI-associated Hall current structure extending to the nightside (the second vertical dashed line in Figure 3.5). This feature is qualitatively consistent with the observation around 0745 UT on 13 March 1989 as shown in Figure 3.3. The southward IMF case (Run-33s) appears to fit better to the geomagnetic observations, not only in the amplitude of the variations, but also the waveforms, which agrees with the conclusion that the IMF was southward by Boteler (2019). While the time scale of the large-amplitude decrease of B_x in Canada is closer to the low-density case than the high-density one. Although, these discrepancies of the geomagnetic response between northward and southward IMF cases exist, the common feature appears regardless of the polarity of IMF B_z. Note that we cannot compare the magnetic disturbances with the observations quantitatively since the solar wind and IMF data was unavailable during that period. But as discussed below, the negative excursion could be related to the magnetic disturbance involved in the blackout.

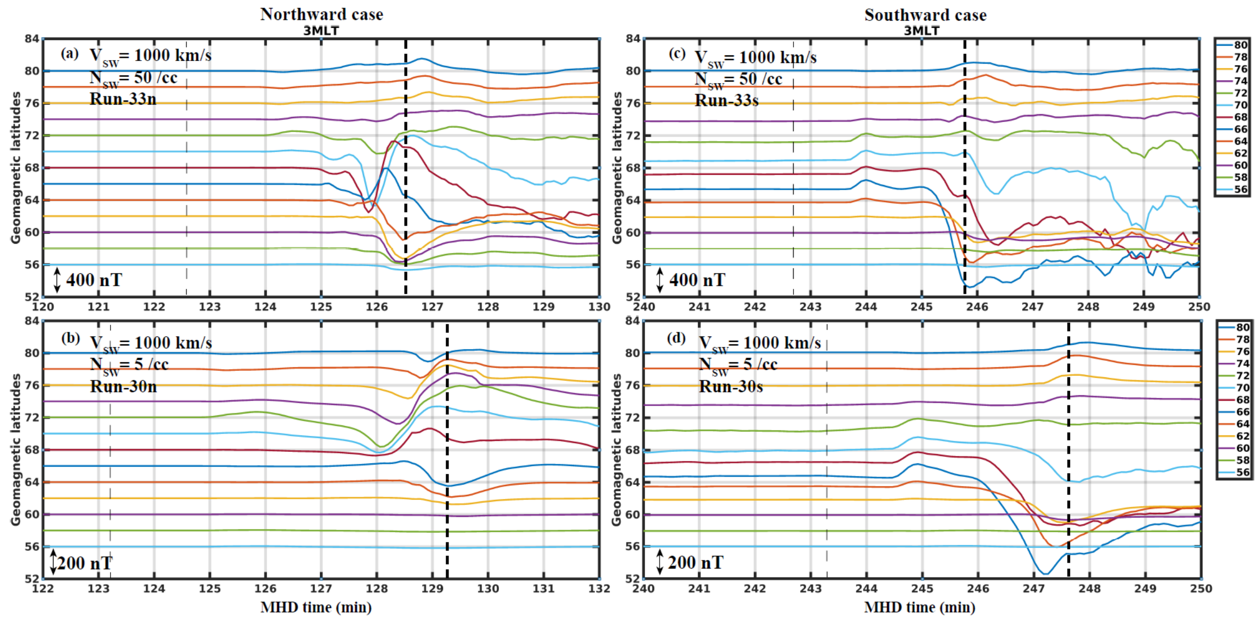

Figure 3.5 Stack plot B_x of (a) Run-33n (northward IMF, increases in solar wind velocity and density), (b) Run-30n (northward IMF, an increase in solar wind velocity), (c) Run-33s (same as Run-33n except for southward IMF), and (d) Run-30s (same as Run-30n except for southward IMF) along MLATs at 0300 MLT. The base line of B_x is taken at T = 120 min for the two panels on the left, and T = 240 min for the two panels on the right. The distance between ticks in the vertical axis corresponds to 400, 400, 200, 200 nT, respectively. The first vertical dashed line indicates the time when the shock arrives at the subsolar bow shock, and the second one indicates the moment when the tendency occurs.

3.4.2.2 Field-aligned currents and ionospheric electric potential

In this chapter, the magnetic disturbance is calculated by the ionospheric Hall current in the simulation. The Hall current is determined by the ionospheric Hall conductivity and the electric field. The electric field is determined by the conductivity and the field-aligned currents (FACs) so as to satisfy the current continuity. Thus, the magnetic disturbance should be tightly related to the FACs in the simulation. Figure 3.6 shows the snapshots of FACs (filled contour in the top panel), electric potentials (line contour in the top panel), and B_x disturbances (filled contour in the bottom panel) for Run-33n, in which the solar wind velocity is increased to 1,000 km/s and the solar wind density is increased to 50/cc. The following is a brief summary of the variation of the FACs, the electric potential and the magnetic disturbances.

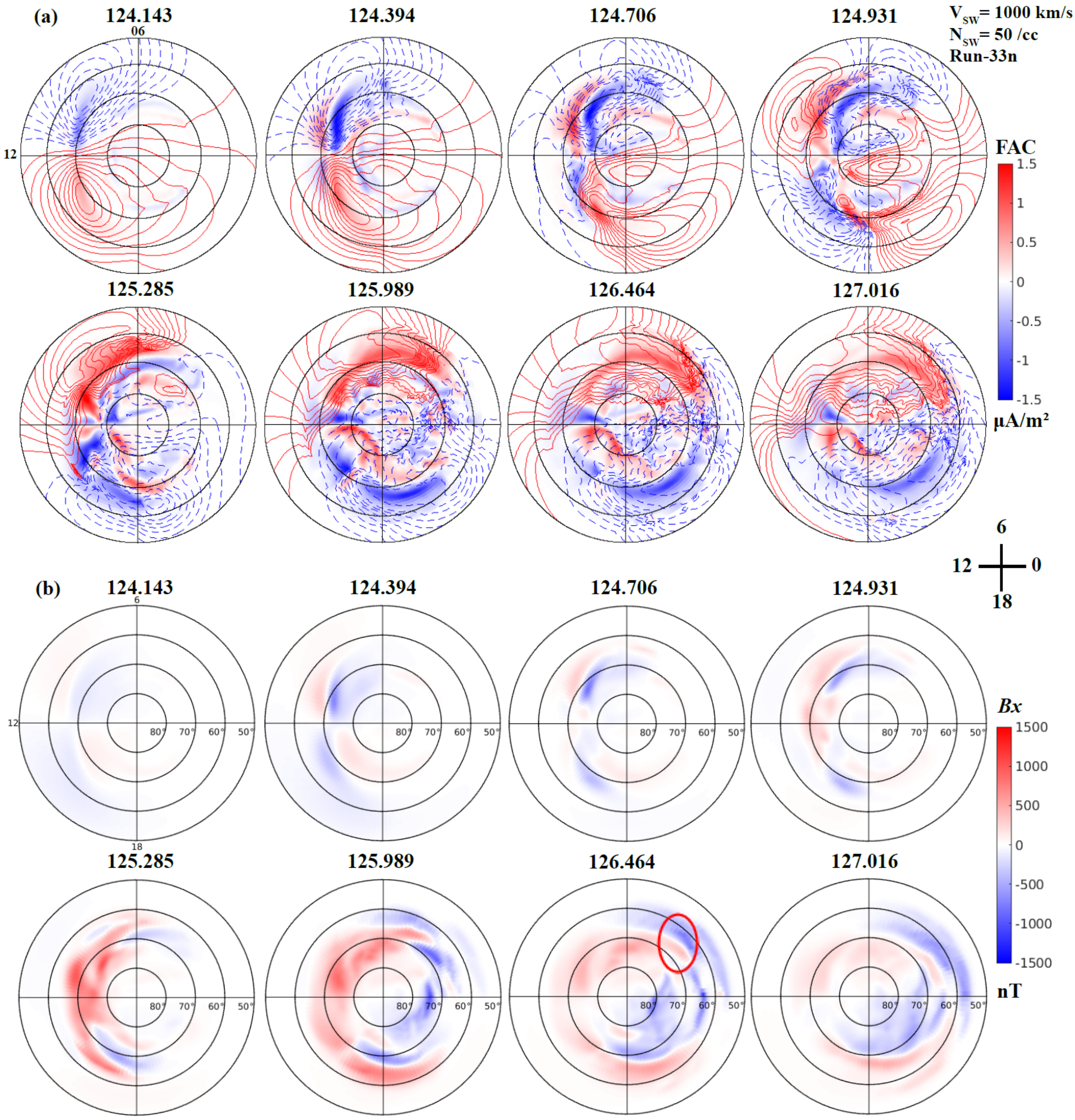

Figure 3.6 8 snapshots of (a) FACs in μA/m^2 (colored contour, positive downward) and electric potentials, and (b) B_x in nT (positive northward) for Run-33n. The solid line indicates positive potential and the dashed lines negative potential. The outermost circle corresponds to 50 MLAT. The Sun is to the left. The number on the top of each panel is the MHD time T. The jump of the dynamic pressure took place just upstream of the bow shock at 120 min.

Figure 3.7 is the same as Figure 3.6a except for Run-02n, that is, a small jump in the solar wind density. At 128.8 min, PI-associated FACs (upward on dawnside and downward on duskside) appear on the dayside first, propagating in the anti-sunward direction. Then, MI-associated FACs (downward on dawnside and upward on duskside) appear, which propagate in the anti-sunward direction. Again, the ionospheric Hall current flows in the clockwise direction around the MI-associated FACs on the nightside. The intensity of the MI-associated FACs increases as they propagate in the anti-sunward direction. It is clearly shown that the MI-associated FACs also appear for a small jump in the solar wind density. The similar motion of the Hall current vortex to the nightside is observed in the southward IMF cases as well (not shown here).

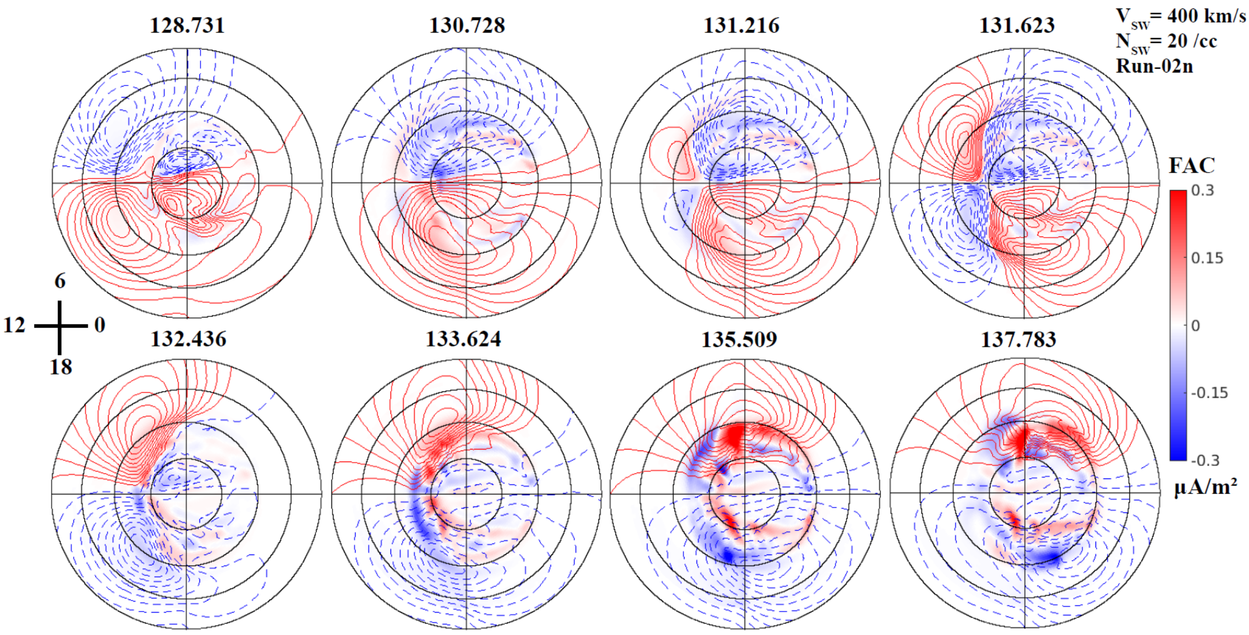

Figure 3.7 Same as Figure 3.6a except for Run-02n. The solar wind velocity remains constant to be 400km/s, whereas the solar wind density increases to 20/cc.

3.4.2.3 Amplitude of geomagnetic disturbances

Figure 3.8 shows the distribution of the 99th percentile of $|B_x|$ disturbances during full time series (to avoid the possible extreme values caused by the numerical instability) for each point in response to the jump in the solar wind density and/or solar wind density for northward IMF. These maps are useful to understand the overall response of the geomagnetic disturbances to the rapid change in the solar wind parameters in the context of the GIC prediction work. There are some characteristics to be noted. First, it is obvious that the amplitude of these disturbances increases with the increase of solar wind velocity and/or density. Secondly, when the solar wind velocity and density are low, the magnitude of geomagnetic variations is much larger on the dayside than on the nightside as shown in the first three columns. Thirdly, when the solar wind velocity and density are high enough, large disturbances appear on the nightside, especially between 60-70 MLAT. This implies that the nighttime polar region is also sensitive to hazardous GICs when a large-amplitude solar wind jump arrives. The dawn-dusk asymmetry is probably due to the different ionospheric conductivity. The small increase of the conductivity on the dawnside where the upward FAC flows is likely to result in changes in the ionospheric current.

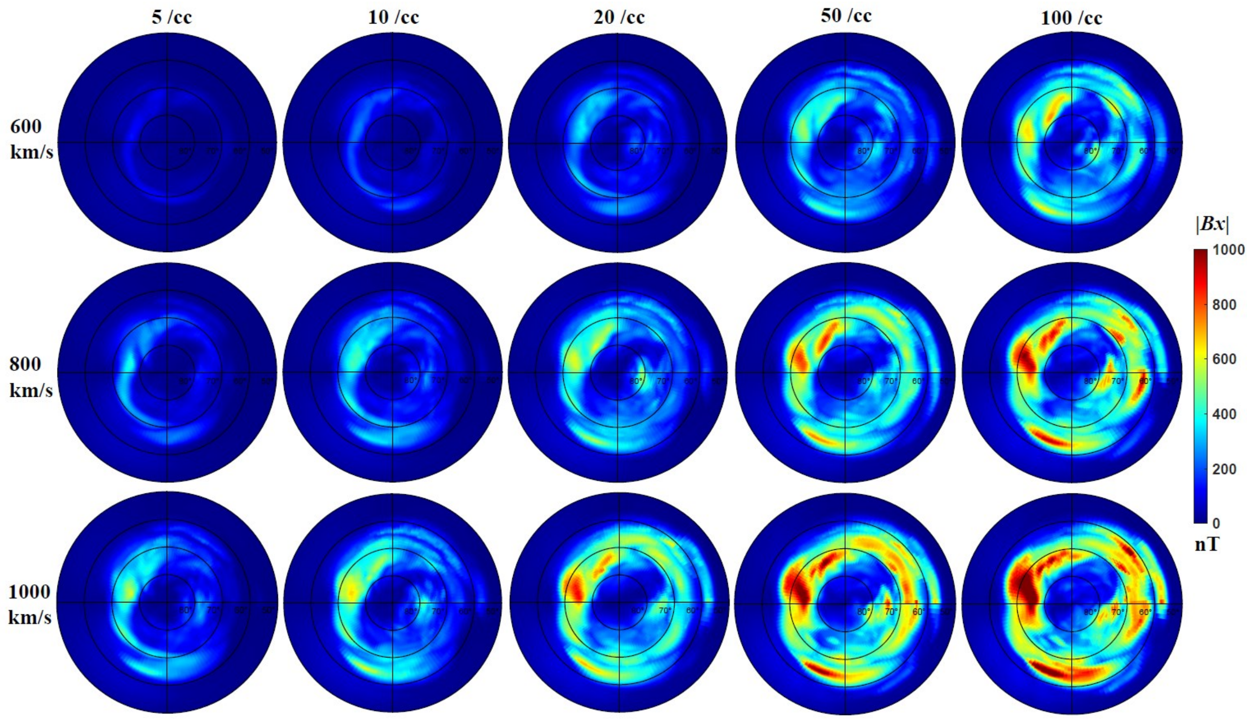

Figure 3.8 Distribution of the 99th percentile $|B_x|$ disturbances for the northward cases. The panels from top to bottom indicate the runs with the solar wind velocity of 600, 800, 1000 km/s, and the panels from left to right indicate those with the density of 5, 10, 20, 50, 100/cc. The outermost circle corresponds to 50 MLAT. The Sun is to the left.

3.4.2.4 Temporal variations of the geoelectric field

We calculated the induced geoelectric field according to Equation (3.3) for Run-33n (V_{sw} = 1000 km/s, N_{sw} = 50/cc). Figure 3.9 shows B_x and the corresponding E_y at 0242 MLT and

64.7 MLAT, which is close to PBQ (see Table 3.1 Observatories information.). B_x (black curve) starts showing a negative excursion with a relatively small amplitude at ≈ 125.2 min, followed by a rapid decrease with a higher time rate of change. This tendency is similar to that observed at PBQ and FCC as shown in Figure 3.3, although the amplitude and the scale of the temporal variation in both results are different. The large negative perturbation starting at ≈126.1 min is caused by the MI-associated Hall current as explained in Section 3.4.2.2. The orange curve in Figure 3.9 shows the calculated eastward geoelectric field. The amplitude of the geoelectric field increases rapidly, and reaches the maximum value just before and around the maximum of the amplitude of B_x. This may reasonably explain the Québec blackout, in which the blackout took place in the course of the large decrease in B_x.

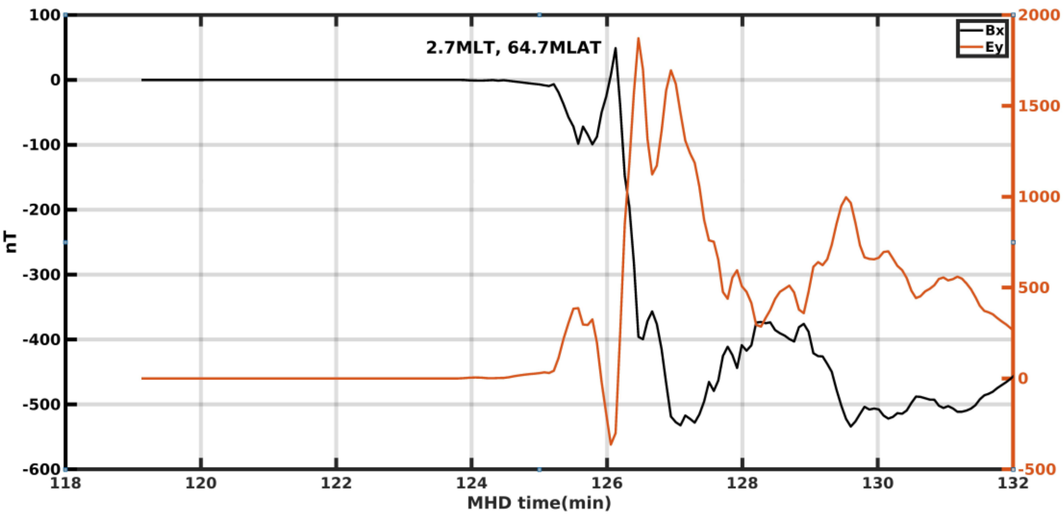

Figure 3.9 Northward component of the magnetic perturbation B_x (black curve) and eastward component of geoelectric field E_y (orange curve) of Run-33n (1000 km/s, 50/cc) at 0242 MLT and 64.7 MLAT.

3.5 Discussions and Conclusions

Fujita et al. (2003b) assumed that the ground magnetic variations observed at high latitudes are explained by the ionospheric Hall currents closely related to a pair of upward and downward field-aligned currents (FACs). The downward and upward FACs are associated with the clockwise and counterclockwise potential cells (so-called double-cell system), and there are two sequential systems with the opposite polarity, the first corresponding to PI and the second corresponding to MI (Moretto et al., 2000). Sequential occurrence of the two vortices of the Hall current (PI then MI phase) induces the bipolar magnetic field variations at a fixed point on the ground. Fujita et al. (2003b) focused on the MI-associated current systems and showed three latitudinal variation of the *H* (north-south)- and *D* (east-west)-components of the ground magnetic field at 1200, 1500, and 1800 MLT. Kubota et al. (2015) also demonstrated the magnetic variations on the ground on the basis of the global MHD simulation. Large-amplitude magnetic variations are shown not only on the dayside, but also on the nightside. These features are, in general, consistent with the results shown above.

Araki et al. (2006) showed the large-amplitude SCs at midnight observed at 3 Japanese geomagnetic stations. Shinbori et al. (2009) similarly performed a statistical study of the observed magnetic disturbances, and showed that the amplitude of SC is enhanced on the nightside from the middle latitudes to the equator. They both attributed the nighttime enhancement to the contribution from the MI-associated FACs expanding equatorward. Even earlier, Araki et al. (1985) pointed out that the geomagnetic variation associated with a PRI (preliminary reverse impulse) may appear on the nightside equator as well although its amplitude is very small. It is worth noting that in these studies, on the nightside at mid- and low-latitudes, the northward magnetic disturbance is observed, which could be induced by the FACs associated with the SCs. We investigated the contribution from FACs, Hall and Pedersen currents at several locations (see Tab. A.1) and also the nighttime changes with the MHD time at different MLATs (Fig. A.**1** in 0), and found that a part of the contribution from the FAC could be canceled by the ionospheric Pedersen current in the polar region where the magnetic inclination angle is fairly high. The contribution from Hall currents is getting higher when the observing point approaches the source region at high latitudes (Tanaka et al. 2020). The contribution to northward geomagnetic disturbances of Pedersen currents and FACs is much smaller compared to that of Hall currents, especially on the nightside. We will further investigate how the disturbances associated with the FACs vary in time and space during SC in the near future, especially at high latitudes.

We showed the temporal and spatial variations of FACs and the resultant ionospheric electric potential in Figure 3.6a and Figure 3.7. When the jump in the solar wind dynamic pressure is large (400 to 1000 km/s, 5 to 50/cc, see Figure 3.6a), the propagation of the MI-associated FACs and the electric potential cells are clearly seen at higher latitudes (around and above 70

MLAT). When the jump is small (no jump of velocity, density from 5 to 20/cc, see Figure 3.7), the propagation of the MI-associated FACs is somewhat complicated, and is relatively slow. The motion of dawnside/duskside potential cells looks more westward/eastward, whereas the motion of the associated FACs looks more poleward. This tendency is different with the evolution of the ionospheric electric potential obtained by the assimilative mapping of ionospheric electrodynamics (AMIE) (Moretto et al. 2000) and some other studies based on the observed magnetic data (Stauning & Troshichev, 2008; Madelaire et al., 2022). In these studies, the jumps of the solar wind dynamic pressure are relatively small. For example, the SC investigated by Moretto et al. (2000) is triggered by a jump of the solar wind dynamic pressure, in which the solar wind speed increased from ≈ 310 to ≈ 360 km/s and the density from ≈ 2 to ≈ 10/cc. They pointed out that the potential cells in the polar cap move very slowly and poleward rather than anti-sunward. In our simulation, the MI-associated potential vortex would propagate clearly in the anti-sunward direction both for high and low jump cases (the extension of Hall current structure to the nightside). That is, the resultant large-amplitude southward disturbances related to the MI-associated ionospheric current would also propagate clearly in the anti-sunward direction. As shown in Figure 3.3, the southward magnetic perturbations appeared at < 67 MLAT, whereas the northward ones appeared at > 67 MLAT in Canada after the SC that took place at 0743 UT on 13 March 1989. The boundary between the southward and northward perturbations is located at ≈ 67 MLAT, which probably corresponds to the center of the MI-associated downward FACs propagating anti-sunward.

The amplitude of the negative disturbances reaches ≈ 1,800 nT around 0746 UT on 13 March 1989 in the post-midnight sector as shown in Figure 3.3. The amplitude of the negative disturbances obtained by the MHD simulation is smaller than the observation. We cannot discuss the amplitude of the magnetic disturbances quantitatively because of the lack of the solar wind parameters and IMF for this event. Whereas, for the SC on 15 May 1997, the magnitude of disturbances shown in Figure 3.2 is comparable to that of the Run-12n (see Figure 3.4), when the jump of the dynamic pressure is close. It is worth stating that the magnetic disturbances depend largely on the choice of the MLAT. Figure 3.9 shows the magnetic disturbance at 0242 MLT at 64.7 MLAT, which is close to PBQ. The disturbance is fully different at 0242 MLT and 70.0 MLAT (not shown).

The southward magnetic disturbance is clearly present at subauroral latitudes in the observation (Figure 3.2 and Figure 3.3) and in the simulation (Figure 3.4 and Figure 3.5). In the simulation, the magnetic disturbance was taken at the same MLT, whereas the observational data were acquired from IMAGE stations located in a wider region (about 20 degrees), and even more than 70 degrees in longitude across Canada, according to the map shown in Figure 3.1. The similarity between the observation and simulation most likely implies that the temporal variation of the magnetic disturbance does not depend significantly on the MLT. That is, large-scale potential cells propagated anti-sunward, and similar magnetic disturbances could have been detected widely at various MLTs. In the simulation, the similar magnetic disturbances are found from 0200 to 0500 MLT (about 45 degrees in magnetic longitude).

Last but not least, Boteler (2019) proposed the viewpoint that the blackout of the Hydro-Québec power system was caused by the substorm after the onset of the SC. They found the time of the SC coincides with the onset of a magnetic substorm, suggesting that the shock on the magnetosphere caused a more rapid unloading of energy from the tail than might otherwise have occurred. Previous studies (Yue et al., 2010; Zhou & Tsurutani, 2001) show that interplanetary shocks can trigger substorms and it requires preconditioning by loading of energy in the magnetotail associated with southward IMF B_z. However, to date, we do not know the solar wind condition and the polarity of IMF B_z for the event. In the earlier times, Boteler & Jansen (1993) showed a clear structure of the equivalent current system that westward currents flow at low latitudes and eastward currents flow at high latitudes in Figure 4c of their paper, which is similar with the Hall current vortex shown in our simulations. According to our results, one point to be emphasized is that the MI-associated ionospheric current alone can cause this structure, small positive magnetic disturbances at high latitudes and large negative ones at a bit lower latitudes, that resembles the one observed in Canada. The MI-associated ionospheric current and the resultant magnetic disturbance appear in the post-midnight sector regardless of the polarity of the IMF B_z. We cannot exclude the possibility that the Québec event was directly related to a substorm.

In this chapter, we carried out MHD simulations to investigate the transient disturbances of the ground magnetic field in response to different jumps of the solar wind dynamic pressure. We also compared with the SC-associated magnetic disturbances observed by IMAGE magnetometer network and Canadian observatories, separately. Especially, the magnetic variations took place around 0746 UT on 13 March 1989, at which the Québec blackout occurred. We obtained the conclusions as summarized below:

1. The large-amplitude disturbances were observed in Canada in the post-midnight sector just after the SC that took place around 0743 UT on 13 March 1989. Northward and southward magnetic field disturbance was observed above and below ~ 67 MLAT, respectively. The Québec blackout was likely related to the southward disturbance.

2. The global MHD simulation results show that the northward and southward disturbances can be reasonably explained by the main impulse (MI)-associated ionospheric Hall current that extends to the nightside.

3. In the global MHD simulation, the MI-associated Hall current appears regardless of the magnitude of the jump of the solar wind dynamic pressure and the polarity of IMF B_z. The structure of the Hall current is somewhat complicated and the propagation speed is low on the nightside in comparison with that on the dayside.

4. The amplitude of the geoelectric field reaches the maximum value just before and around the maximum of the southward magnetic disturbance. This is consistent with the observation of the magnetic disturbances in Canada and the moment at which the Québec blackout took place.

5. The magnetic disturbances associated with SC are most significant on the dayside for the jumps of the solar wind dynamic pressure. For the large jumps, the magnetic disturbances on the nightside are also significant and nonnegligible. This implies that the nighttime polar region is also sensitive to hazardous GICs when a large-amplitude jump of the solar wind dynamic pressure arrives.

Chapter 4 Generation of Field-Aligned Currents in Response to Sudden Enhancement of Solar Wind Dynamic Pressure

4.1 Introduction

Sudden commencement (SC) is the so-called ground manifestation of two abrupt and successive geomagnetic disturbances, namely the preliminary impulse (PI) and the main impulse (MI), in response to the jump in solar wind dynamic pressure (e.g., Tamao, 1964; Araki, 1982, 1994; Fujita et al., 2003a, 2003b, 2005; Fujita & Tanaka, 2022; Kikuchi et al., 2016, 2022). It usually exhibits a step-function like increase in the *H*-component (the horizontal component of the disturbance geomagnetic field) at mid- and low-latitudes (DL), and bipolar variations at auroral latitudes (DP). The study of SCs from the global magnetic observations has a long history since the great progress made during the IGY 1957-58 (e.g., Matsushita, 1957; Wilson & Sugiura, 1961; Akasofu & Chapman, 1959).

These observed facts mentioned above are explained by assuming that the ionospheric electric field associated with a pair of upward and downward field-aligned currents (FACs) induces such ground magnetic disturbances through the Hall currents (Araki, 1994). It has been found that the ionospheric Hall current associated with the PI shows a double-cell structure (anticlockwise vortex in the dawn hemisphere, and clockwise vortex in the dusk hemisphere) at high latitudes, followed by a subsequent MI-associated vortex with an opposite sense of the Hall current flowing (e.g., Moretto et al. 2000). The generation mechanism of FACs plays an important role in understanding this very transient physical process.

Many studies based on both observational data analysis and numerical simulation have been done. Tamao (1964) theoretically interpreted the cause of the PI-associated current as the mode conversion from fast magnetosonic wave generated by sudden compression of the dayside magnetosphere to the Alfvén wave. It is suggested that the mode conversion takes place where the spatial gradient of the Alfvén speed arises. Fujita et al. (2003a, 2003b) showed that the excitation of the FAC coincides with the region where the gradient of the Alfvén wave is large, and suggested that the mode conversion from the fast magnetosonic wave to the Alfvén wave occurs. The mode conversion region is clarified to be in the outer magnetosphere through tracing a current line by Fujita & Tanaka (2022), which remains to be verified by obseravation. An induced dusk-to-dawn electric field following the sudden compression is considered as the source that gives rise to the FACs during PI phase in some other studies (e.g., Araki, 1994; Moretto et al., 2000; Yu & Ridley, 2009; Yu et al. 2022). For MI FACs, many studies (e.g., Araki, 1994; Fujita & Tanaka, 2006; Guo & Hu, 2007; Yu & Ridley, 2009; Tian et al. 2016) suggested that the generation is related with a plasma vortex just after the passage of the compressional wave, and the vortex is more dominant during the late stage of MI phase. This process may repeat (e.g., Fujita et al. 2012), since wave-like oscillations are observed in the geomagnetic data as reported in (Hori et al. 2012) and (Yu & Ridley, 2011).

The current generator (dynamo) region is determined by the condition $\mathbf{J}\cdot\mathbf{E} < 0$ (where $\mathbf{J}$ and $\mathbf{E}$ are the current density and the electric field, respectively), which is widely used (e.g., Tanaka, 1995; Siscoe et al. 2000). The negative value stands for energy transfer from plasma flow to electromagnetic energy. Samsonov et al. (2010) investigated the intensification of northward B_z (NBZ) and Region 1 currents (near the poleward edge of the auroral zone, downward on the dawnside and upward on the duskside, Iijima & Potemra, 1976; Zmuda & Armstrong, 1974) due to the interplanetary shock, and identified two strong dynamo regions in the magnetosphere based on this condition. However, Ebihara & Tanaka (2022) pointed out that this criterion ($\mathbf{J}\cdot\mathbf{E} < 0$) does not always mean the generation of Alfvén waves when magnetic pressure force is nonnegligible (see detailed explanation in Section 0).

Keller et al., (2002) found that the generation locations for both PI and MI FACs were in the magnetosphere in response to a density jump of solar wind by mapping FACs along the magnetic field lines. Tracing a magnetic field line from the ionosphere is the most popular method when investigating the generation region of FACs, while FACs do not always flow just along magnetic field lines. Another method of tracing current lines is used by Fujita & Tanaka (2022), who claimed that there were two current systems in PI phase of SCs. Sun et al., (2014) linked the MI-associated geomagnetic response with the negative magnetic field disturbance (magnetic field decreases due to interplanetary shocks) in nightside magnetosphere by tracing the current lines. Whereas the location of current lines would be affected by the field-perpendicular current and do not always pass through the generation region of FACs in the simulations (Ebihara & Tanaka, 2024). This method of tracing current lines may not be able to identify the generation region precisely either.

Thus, we followed a new approach proposed by Ebihara & Tanaka (2022, 2023), who identified the generation region of Region-1 FACs and substorm-associated FACs by tracing a packet of Alfvén wave. The FAC dynamo region is defined therein from the following three aspects based on fundamental physics. The first perspective is the continuity of the current. When FACs are generated, the divergence of the FACs should not be zero due the conservation law. The second one is the time rate of change in the FACs, which should be nonzero, indicating the current is generating. The last is the negative work against the magnetic tension force performed by the plasma, which is supposed to excite the Alfvén waves (see details in Section 4.2.3).

The aim of this study is to understand the generation of FACs in response to the solar wind pressure pulse. The key issues to be settled include where and how the FACs are generated, the reason why there are bidirectional FACs on the same side (dawn or dusk), considering if they are generated by the same mechanism, and what causes the change in the polarity of the FACs during different impulse phases. Thus, the new method that traces the Alfvén wave packet is employed, which enables us to identify the generation region of FACs precisely combined with three criteria mentioned above and obtain the quantities required in the analysis of the simulation result that may help to make clear the generation process. The results are explained in terms of dynamo regions, corresponding to the physical processes in the passage of the compressional wave excited by the impact of solar wind dynamic pressure on the dayside magnetosphere.

4.2 Method

4.2.1 Global MHD simulation

The global MHD simulation code "Reproduce Plasma Universe (REPPU)" is developed by T. Tanaka and the details are explained in his papers (Tanaka, 1994, 1995, 2015). The coordinate system in the magnetospheric domain is set as that the origin is at the center of the Earth, the x-axis points sunward, the z-axis points to the north, and the y-axis is chosen to satisfy the right-handed system correspondingly. The outer boundary conditions correspond to the solar wind on the upstream side at x = 600 R_E at noon and a zero gradient on the downstream side at x = -200 R_E at midnight. The inner boundary is at 2.6 R_E. The grid system is constructed by a sixth-order triangulation with 320 radially stacked spheres. The MHD domain with 30,722 grids is coupled with the ionospheric domain (Ebihara et al., 2014). The grid spacing in the outward direction is 0.044 R_E at the inner boundary, and 0.22 R_E at 12 R_E at midnight in the equatorial plane (Ebihara & Tanaka, 2015). This coupling process considers four aspects: 1) the mapping of instantaneous values of FACs, plasma pressure and temperature from the inner boundary to the ionosphere; 2) the calculation of the height-integrated ionospheric conductivity that is decided by the solar extreme ultraviolet (EUV), and both the contribution from precipitation associated with discrete aurorae and diffuse aurorae; 3) the requirement of current continuity; and 4) the mapping of electric field from the ionosphere to the inner boundary along the dipole magnetic field line (Ebihara & Tanaka, 2022).

The simulation is started from a quasi-stationary state with solar wind parameters of N_{sw} = 5/cc, V_{sw} = 400 km/s, B_y = 0 nT, B_z = 3 nT, where N_{sw} is the solar wind density and V_{sw} is the solar wind velocity. The pressure pulse was imposed by increasing V_{sw} from 400 km/s to 1000 km/s, and N_{sw} from 5/cc to 50/cc at x = 40 R_E and at the elapsed time of 120 min (T = 120 min). The IMF B_z remains northward. The tracing method described in detail below to identify the generation region of the FACs is proposed by Ebihara & Tanaka (2022, 2023).

4.2.2 Alfvén wave packet tracing

It is assumed that the perturbation associated with the FACs propagates at the characteristic velocity **v** (Neubauer, 1980; Wright & Southwood, 1987) as

$$\begin{aligned} \mathbf{v} &= \pm \mathbf{V}_{\mathrm{A}} + \mathbf{V}, \\ \mathbf{V}_{\mathrm{A}} &= \mathbf{B} / \sqrt{(\mu_0 \rho)}, \end{aligned} \tag{4.1}$$

where $\mathbf{V}_{\mathrm{A}}$ is the Alfvén velocity, $\mathbf{V}$ is the velocity of plasma, ρ is the mass density of plasma and μ_0 is the magnetic constant. The group velocity of the Alfvén wave moves along the background magnetic field in the rest frame of the moving medium (Walker, 2008). The sign $\pm$ indicates the motion is parallel (+) or antiparallel (-) to the magnetic field, separately. The packet of Alfvén wave carrying the information associated with the FACs could be located by the equation below (Ebihara & Tanaka, 2022, 2023):

$$\mathbf{r}(t) = \int_0^t \mathbf{v}(\mathbf{r}, \tau) d\tau + \mathbf{r}_0, \tag{4.2}$$

where $\mathbf{r}_0$ is the starting point of tracing. The inner boundary of the MHD domain is located at 2.6 R_E. The packets were first traced from the ionosphere to a sphere at a radius of 3.9 R_E along the dipole magnetic field line, then from this sphere to the further region using Equations (4.1) and (4.2) with positive $\mathbf{V}_{\mathrm{A}}$ (Ebihara & Tanaka, 2023).

4.2.3 Identification of FAC generation

Three criteria of FAC dynamo mentioned in the introduction are described as follows.

1) The first criterion is based on the current continuity,

$$\begin{aligned} &\nabla\cdot\mathbf{J}_{\parallel}+\nabla\cdot\mathbf{J}_{\perp}=0, \\ &\mathbf{J}_{\perp}=\mathbf{J}_{d}+\mathbf{J}_{i} \end{aligned} \tag{4.3}$$

where $\nabla\cdot\mathbf{J}_{\parallel}\neq 0$, indicating the field-perpendicular current (including the diamagnetic current $\mathbf{J}_d$ and the inertial current $\mathbf{J}_i$) is converted to the FAC.

2) The second criterion is the nonzero rate of change in the FAC (Itonaga et al., 2000; Song & Lysak, 2001),

$$\begin{aligned} \frac{\partial J_{\parallel}}{\partial t} &= -\frac{1}{\mu_0}\left(\nabla\times\nabla\times\mathbf{E}\right)_{\parallel} \\ &= \frac{-\nabla_{\parallel}\left(\nabla\cdot\mathbf{E}\right)}{\mu_0}+\frac{\left(\nabla^2\mathbf{E}\right)_{\parallel}}{\mu_0}, \end{aligned} \tag{4.4}$$

where $\mathbf{E}$ is the electric field and only $\mathbf{E}_{\perp}$ is present under the ideal MHD approximation. The displacement current is omitted.

3) The third criterion is associated with the excitation of Alfvén waves. To understand the origin of Alfvén waves, it is relevant to define the magnetic tension first. The Lorentz force is

$$\begin{aligned} \mathbf{F} &= \mathbf{J}\times\mathbf{B} \\ &= \frac{1}{\mu_0}(\nabla\times\mathbf{B}\times\mathbf{B}), \end{aligned} \tag{4.5}$$

with the vectorial identity, we obtain

$$\begin{aligned} \mathbf{F} &= \frac{1}{\mu_0}(\nabla\times\mathbf{B}\times\mathbf{B}) \\ &= -\nabla\left(\frac{B^2}{2\mu_0}\right)+(\mathbf{B}\cdot\nabla)\frac{\mathbf{B}}{\mu_0}, \end{aligned} \tag{4.6}$$

where the Lorentz force involves two terms. The generation of an Alfvén wave could be described as the magnetic field line is first bent due to the motion together with the plasma according to frozen-in theorem, and then magnetic tension appears in the field line, so the plasma performs negative work against the tension force. Based on Ebihara & Tanaka (2022, 2023), the Lorentz force **F** is decomposed into the magnetic pressure force $\mathbf{F}_m$ and the magnetic tension force $\mathbf{F}_t$ as

$$
\begin{aligned}
\mathbf{F} &= \mathbf{F}_m + \mathbf{F}_t, \\
\mathbf{F}_m &\equiv -\nabla_{\perp}\left(\frac{B^2}{2\mu_0}\right), \\
\mathbf{F}_t &\equiv (\mathbf{B}\cdot\nabla)\frac{\mathbf{B}}{\mu_0} - \nabla_{\parallel}\left(\frac{B^2}{2\mu_0}\right) \\
&= \frac{B^2}{\mu_0}(\mathbf{b}\cdot\nabla)\mathbf{b},
\end{aligned}
\tag{4.7}
$$

where **b** is the unit vector of the magnetic field (=$\mathbf{B}/B$), and $B^2/2\mu_0$ is the magnetic pressure. Ebihara & Tanaka (2022) pointed out that ($\mathbf{J}\cdot\mathbf{E} = \mathbf{V}\cdot\mathbf{F} < 0$) is not necessarily associated with the generation of Alfvén waves when the magnetic pressure force is present. Thus, the last criterion is given as

$$
\mathbf{V}\cdot\mathbf{F}_t < 0. \tag{4.8}
$$

Magnetic tension is necessary for exciting Alfvén waves. Although this condition indicates the excitation of Alfvén waves, it does not always generate FACs (Cravens, 1997; Ebihara & Tanaka, 2024). Consequently, all the three criteria listed above must be satisfied when identifying the generation of FACs. For example, for a downward FAC ($J_{\parallel} > 0$) transported by an Alfvén wave parallel to the magnetic field ($V_A > 0$) in the Northern Hemisphere, the three conditions based on the above criteria should be: $\nabla\cdot\mathbf{J}_{\parallel} > 0$, $\partial J_{\parallel}/\partial t > 0$, and $\mathbf{V}\cdot\mathbf{F}_t < 0$.

4.3 Results

4.3.1 Candidate dynamo regions (where $\mathbf{V}\cdot\mathbf{F}_t < 0$) in the magnetosphere

Figure 4.1 shows the evolution of the velocity of plasma flow (Figure 4.1a ~ Figure 4.1f) and the distribution of $\mathbf{V}\cdot\mathbf{F}_t$ (Figure 4.1g ~Figure 4.1l) in the equatorial plane after the propagation of the sudden pressure pulse according to the MHD simulations. The discussion in this paper is focused only on the dawnside due to IMF $B_y = 0$. The red curves in top six panels (from Figure 4.1a to Figure 4.1f) correspond to $\mathbf{V}\cdot\mathbf{F}_t = -2.0\times10^{-12}$ W/m³, and the green curves in bottom six panels (from g to l) correspond to $\mathbf{V}\cdot\mathbf{F}_t = -1.0\times10^{-12}$ W/m³. These red and green lines are surrounding the Earth at the early stage due to the Earth's intrinsic magnetic field. The change in the colors of shadings in Figure 4.1a ~ Figure 4.1f indicates the location of bow shock and magnetopause as the solar wind is suddenly decelerated there.

Figure 4.1a shows that the impulse front encounters the magnetopause at around $T = 123.05$ min, the magnetopause starts to move inward and this results in a compressional wave propagating into the magnetosphere (Samsonov & Sibeck, 2013). The compressional front is in a convex shape, and shortly deformed by the touch of a particular boundary as shown in Figure 4.1b. The front part across the Sun-Earth line becomes a concave shape (Samsonov et al. 2007), and extends forward through the flank continuously towards nightside according to Figure 4.1c. When the PI FACs start to appear in the 3 R_E sphere as shown in Figure 4.1i, the first $\mathbf{V}\cdot\mathbf{F}_t < 0$ region located at the compressional front is developing. We call it FAC dynamo 1. Soon later, the plasma behind the compressional front flows along the boundary, and then another region with $\mathbf{V}\cdot\mathbf{F}_t < 0$ is formed on the dayside in Figure 4.1d and Figure 4.1j. We call it FAC dynamo 2. Meanwhile, the plasma is decelerated and diverted near the dawnside. Later, on the dayside the plasma inside the boundary moves sunward instead, and another region near noon with $\mathbf{V}\cdot\mathbf{F}_t < 0$ appears as shown in Figure 4.1e and Figure 4.1k. This region is called Region 3, expanding rapidly towards nightside. The slow sunward plasma flow inside the boundary together with the outside fast anti-sunward flow develops into a flow vortex (Sibeck, 1990; Fujita et al., 2003b; Samsonov & Sibeck, 2013; Shi et al.,

2014) according to Figure 4.1f. It should be noted that the naming of the three regions is based on that FACs are generated in the first two regions, so they are called FAC dynamo 1 and 2 (to distinguish with the existed Region-1 and Region-2 FACs), but no FACs are generated in Region 3 according to the following study. Both of FAC dynamo 1 and 2 have a 3-D structure.

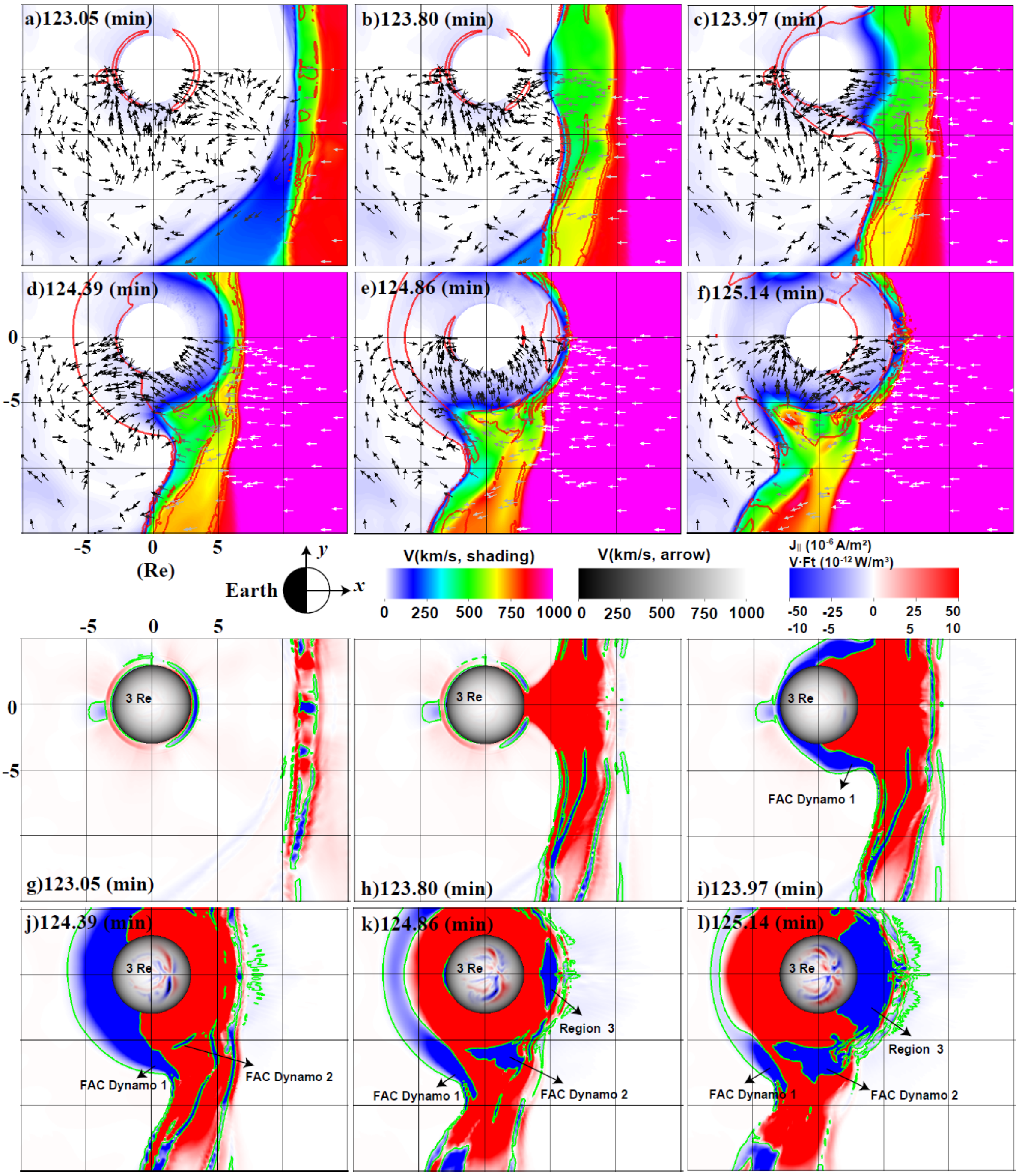

Figure 4.1 A time sequence of six snapshots of the MHD simulation in the equatorial plane ($z = 0$). Sun is to the right. Top six panels (from a to f) show the evolution of plasma flow velocity; blank area marks the inner boundary; colors and arrows indicate the magnitude and direction of the plasma flow. Bottom six panels (from g to l) indicate the evolution of FACs on 3 R_E sphere and $\mathbf{V} \cdot \mathbf{F}_t$ in the equatorial plane; magnitude and polarity of FACs and $\mathbf{V} \cdot \mathbf{F}_t$ are indicated by colored shadings, red for positive and blue for negative.

4.3.2 Footprints of FACs in the ionosphere

Figure 4.2 shows the FACs (color shadings) and the electric potential (contour lines) in the ionosphere taken at T = 124.55, 125.57 and 126.06 min. The solar wind velocity is increased from 400 km/s to 1,000 km/s and the solar wind density is increased from 5/cc to 50/cc. The whole evolution of the simulated SC in response to the pressure pulse could be found in Zhang et al. (2023). A pair of FACs corresponding to PI (upward on the dawnside, and downward on the duskside) appear first in Figure 4.2a. Then, the other pair of FACs with the opposite sense corresponding to MI appear and move in the anti-sunward direction. Figure 4.2b shows a snap shot at T = 124.55 min when PI and MI FACs had appeared in the ionosphere. We chose a point that is located at the leading edge of PI-associated upward FAC on the dawnside, and call it P_1. Figure 4.2c is taken at T = 125.57 min when MI keeps developing and moving anti-sunward. We chose a point that is located at the leading edge of MI-associated downward FAC on the dawnside. We call this point P_2. Figure 4.2d shows the snapshot at T = 126.06 min, corresponding to a very late stage of SC. We chose a point in the heart of the MI-associated downward FAC, and call it point P_3. The corresponding tracing of the Alfvén wave packets associated with the three moments is started from the point P, located at the ionospheric altitude, then along the magnetic field line to the point Q (see details in Table 4.1) on the sphere with a radius of 3.9 R_E (to avoid uncertainty in the calculation of the Alfvén velocity near the inner boundary). The tracing would continue from this sphere backward in time in the way as expressed in Equations (4.1) and (4.2). The trajectories of the packets from P_1, P_2 and P_3 shown in Figures 4.3-4.5 are connecting to three $\mathbf{V}\cdot\mathbf{F}_t < 0$ regions in Figure 4.1, separately. In fact, most points distributed in the footprints as shown in Figure 4.2 were selected as the start point of tracing to find the generation region, but only those in a small region satisfied three criteria. We chose the points (P_1 and P_2) in this region, because the generation of the FACs is clearly identified near the leading edges of the PI- and MI-associated FAC regions.

Table 4.1 Locations on the trajectory of traced Alfvén wave packets.

MHD time T (min)	Point on the ionosphere P (MLT, MLAT)	Point on 3.9 R_E Q (x, y, z)*
124.55	P_1 (7, 70)	Q_1 (0.63, -2.59, 2.84)
125.57	P_2 (5, 67)	Q_2 (-1.04, -3.02, 2.28)
126.06	P_3 (7, 67)	Q_3 (0.71, -3.11, 2.38)

* x, y, z in unit of R_E.

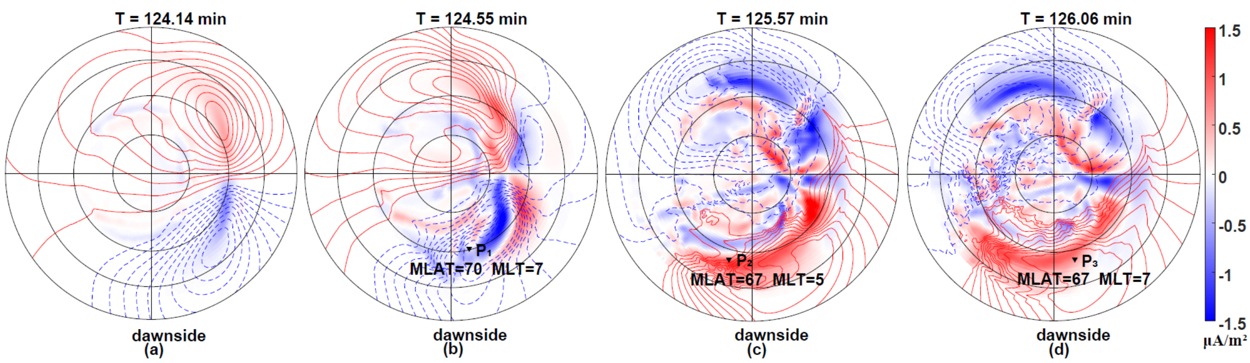

Figure 4.2 Snapshots of the footprints of the FACs and the electric potential in the ionosphere. Negative/positive values indicate upward/downward FACs (bluish/reddish). Sun is to the right, and the outermost circle represents the magnetic latitude of 50°. The solid/dashed contour lines represent positive/negative potential, respectively. The triangles in black indicate the starting point of tracing from the ionosphere.

4.3.3 Generation of FACs

Figure 4.3 summarized the associated quantities (panels on the left-hand side) taken along the trajectory indicated by a long thin tube in the snapshot on the right, and the location of Alfvén wave packet at T = 124.3 min (indicated by the green vertical dashed lines in the left panels) is depicted using a short thick tube in this trajectory. The packet arrived at P_1 (7 MLT, 70 MLAT) in the ionosphere at 124.55 min, where the upward FAC ($J_{\parallel} < 0$, PI-associated FAC on the dawnside) has just begun to develop in the ionosphere. The snapshot on the right column indicates the flow velocity of plasma in the x-y and x-z planes, the FACs on the sphere, with a radius of 3.9 R_E and the red contour lines that are plotted to indicate $\mathbf{V} \cdot \mathbf{F}_t = 0$ in the two planes. A small plane shows the magnitude of the flow velocity in the *x-y* plane at z = 2.7 R_E at which the packet intersects at this moment. The color of the tubes (short and long one) indicates $\mathbf{V} \cdot \mathbf{F}_t$. We traced the packet backward in time from the point Q_1 (0.63, -2.59, 2.84) R_E on the 3.9 R_E sphere, which is mapped to the point P_1 (7 MLT, 70 MLAT) in the ionosphere along the dipole magnetic field line (see Table 4.1). It is found from Figure 4.3c, Figure 4.3d and Figure 4.3e that the FACs are generated in the limited region around the green vertical line, where all the criteria mentioned in Section 4.2.3 are met, that is, $\nabla \cdot \mathbf{J}_{\parallel} < 0$, $\partial J_{\parallel} / \partial t < 0$, and $\mathbf{V} \cdot \mathbf{F}_t < 0$. The generation region is located at off-equator, and for this particular packet, it is located at (1.2, -5.6, 2.7) R_E at T = 124.3 min. This belongs to FAC dynamo 1. According to Figure 4.3c, the FAC is almost closed with the diamagnetic current ($\mathbf{J}_d$). According to Equation (4.4), the time rate of change in FACs ($\partial J_{\parallel} / \partial t$) is decomposed into $-\nabla_{\parallel}(\nabla \cdot \mathbf{E}) / \mu_0$ and $(\nabla^2 \mathbf{E})_{\parallel} / \mu_0$. The two terms are indicated by the red and blue lines, respectively in Figure 4.3d. In this case, they both contribute to the generation of this upward (negative) FAC at the compressional front. Figure 4.3f shows the parallel component of the Poynting flux defined by

$$S_{\parallel} = \frac{\mathbf{E} \times \mathbf{B}}{\mu_0} \cdot \frac{\mathbf{B}_0}{\mathrm{B}_0} \tag{4.9}$$

where $\mathbf{B}_0$ is the dipole magnetic field (Ebihara et al. 2020). At the low altitudes where the dipole magnetic field dominates, $S_{\parallel}$ is expected to reasonably represent the Poynting flux associated with the Alfvén waves. Obviously, $S_{\parallel}$ is positive at distance less than 3 R_E, which indicates that the magnetic energy flows in the direction to the Northern ionosphere out of the region where the FAC is generated. The Alfvén speed V_A shown in Figure 4.3g increases quickly in a short time, and the plasma is accelerated in the anti-sunward direction at the compressional wave front as shown in Figure 4.3h. The Figure 4.3i indicates the location of the packet, showing that the generation region for this case is off the equator. The generation mechanism will be discussed in next subsection.

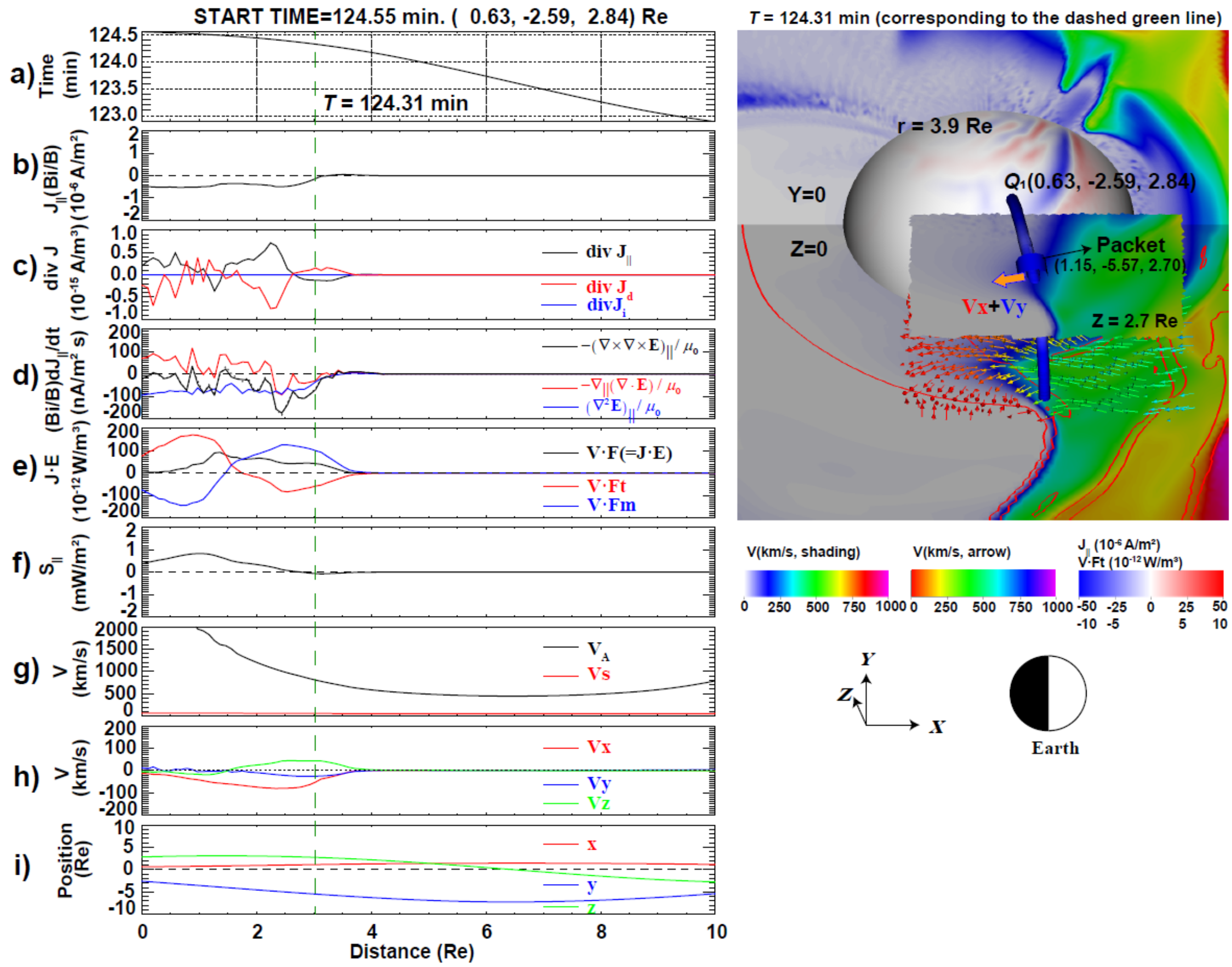

Figure 4.3 Quantities taken along the trajectory of the packet of the Alfvén wave associated with PI. (a) Elapsed time, (b) Normalized field-aligned current (FAC) (B_i/B) $J_\parallel$ (positive parallel and negative anti-parallel to the magnetic field), (c) $\nabla\cdot\mathbf{J}_\parallel$, $\nabla\cdot\mathbf{J}_d$, and $\nabla\cdot\mathbf{J}_i$, where $\mathbf{J}_\parallel$, $\mathbf{J}_d$ and $\mathbf{J}_i$ are the FAC, the diamagnetic current and the inertial current, respectively, (d) the rate of change in the FAC, $\partial J_\parallel/\partial t$, consists of $-\nabla_\parallel(\nabla\cdot\mathbf{E})/\mu_0$ (red line) and $(\nabla^2\mathbf{E})_\parallel/\mu_0$ (blue line), (e) $\mathbf{J}\cdot\mathbf{E}$ (black), $\mathbf{V}\cdot\mathbf{F}_t$ (red) and $\mathbf{V}\cdot\mathbf{F}_m$ (blue), where $\mathbf{F}_t$ and $\mathbf{F}_m$ are the magnetic tension force and the magnetic pressure force, respectively, (f) parallel Poynting flux $S_\parallel$, (g) velocity of Alfvén speed and sound speed, (h) velocity of plasma, and (i) the position; the snapshot taken at T = 124.31 min in the right column shows the location of the Alfvén wave packet on the trajectory from Q_1 on the 3.9 R_E sphere (color of shadings on the sphere indicates intensity of FACs) to the equatorial plane, and the plasma flow in the x-y and x-z plane. Arrows indicate the flow velocity in z planes. The color of tubes and shadings indicate the value of $\mathbf{V}\cdot\mathbf{F}_t$ and $J_\parallel$, separately.

Figure 4.4 is the same as Figure 4.3 except for the packet that reached P_2 (5 MLT, 67 MLAT) at 125.57 min, where the downward FAC ($J_{\|} > 0$, MI-associated FAC on the dawnside) has begun to develop in the ionosphere. In this case, the three criteria, $\nabla \cdot \mathbf{J}_{\|} > 0$, $\partial J_{\|} / \partial t > 0$, and $\mathbf{V} \cdot \mathbf{F}_t < 0$, are satisfied around T = 125.28 min as shown in Figure 4.4c, Figure 4.4d and Figure 4.4e. The generation region for the downward FAC is in the vicinity of the equatorial plane, which belongs to FAC dynamo 2. For this specific packet, it crossed the equatorial plane at (-3.0, -4.8, 0.0) R_E. According to Figure 4.4c, the divergence of inertia current ($\mathbf{J}_i$) plays a minor role in the closure of the FAC compared to the divergence of diamagnetic current ($\mathbf{J}_d$). In Figure 4.4d, the two terms $-\nabla_{\|}(\nabla \cdot \mathbf{E}) / \mu_0$ (red line) and $(\nabla^2 \mathbf{E})_{\|} / \mu_0$ (blue line) both contribute to the time rate of change in FACs ($\partial J_{\|} / \partial t$) as well. In contrast to that for FAC dynamo 1, the former term becomes very positive, which results in the increase of the downward FAC. Figure 4.4e shows $\mathbf{J} \cdot \mathbf{E}$, $\mathbf{V} \cdot \mathbf{F}_t$, and $\mathbf{V} \cdot \mathbf{F}_m$. Though the process of work being performed is much shorter than that for FAC dynamo 1 (see Figure 4.3e), the effect on the Alfvén wave is larger due to the large amplitude of the rate of the energy conversion. The parallel component of the Poynting flux $S_{\|}$ is positive as shown in Figure 4.4f, implying that the magnetic energy propagates towards the Northern ionosphere from the equatorial plane. When comparing Figure 4.4h and Figure 4.3h, it is found that the acceleration of the plasma V_x at the wave front ceases and then decelerates when a flow shear is formed at x = -3 R_E and y = -5 R_E near dawn. While the sunward motion is still too slow at this moment to present a clear vortex structure as shown in Figure 1 by Samsonov & Sibeck (2013). The flow shear is accompanied with the strong downward FAC region.

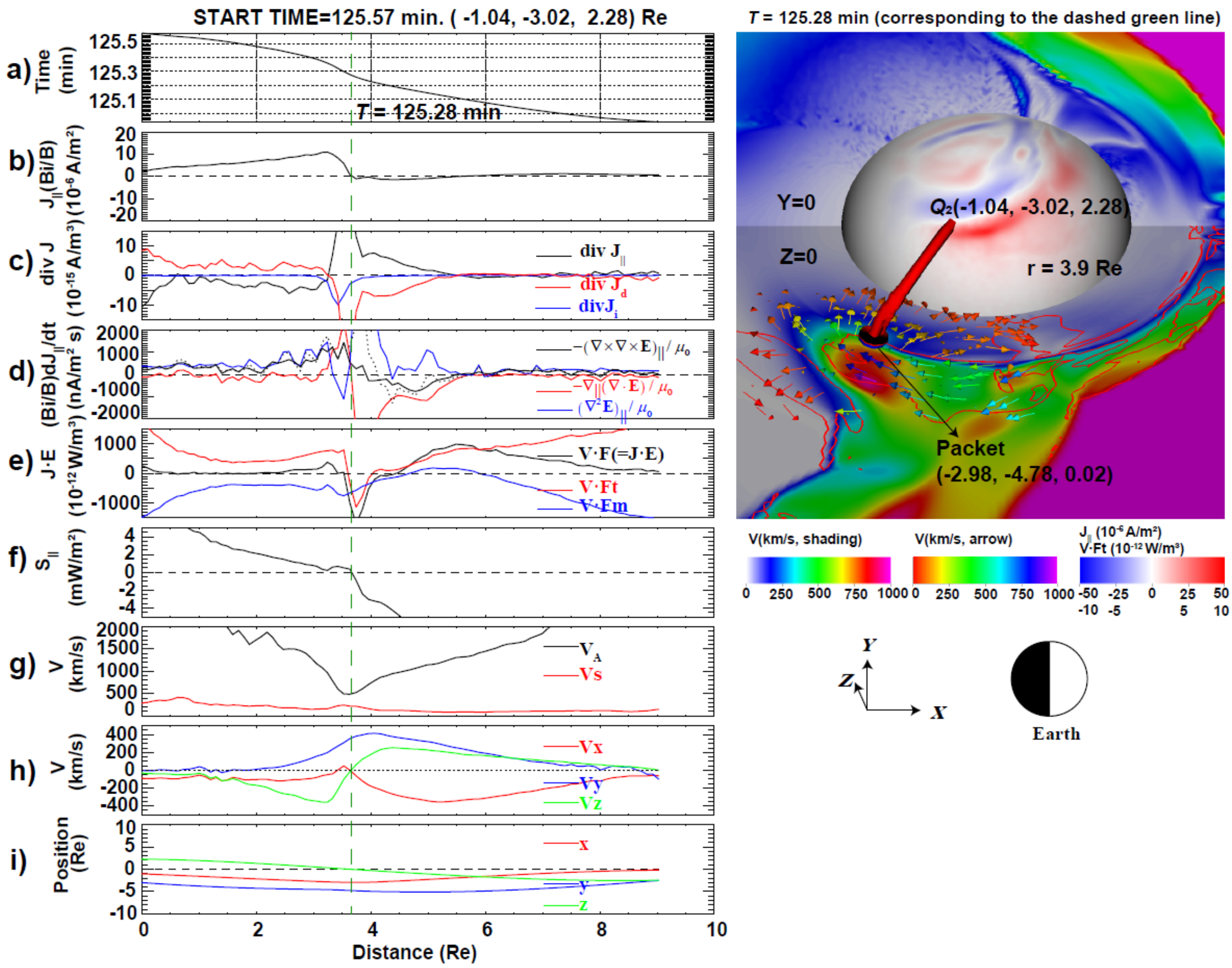

Figure 4.4 Same as Figure 4.3 except for the trajectory of the packet of the Alfvén wave associated with MI. The trace started backward in time from point Q_2 at $T = 125.57$ min, and the snapshot is taken at $T = 125.28$ min.

Figure 4.5 is the same as Figure 4.3 except for the packet that reached P_3 (7 MLT, 67 MLAT) at 126.06 min, where the downward FAC ($J_{\|} > 0$, MI-associated FAC on the dawnside) is in a fairly steady condition. The third region (where $\mathbf{V}\cdot\mathbf{F}_t < 0$) is present after the passage of the pressure pulse. Although the amplitude is small, the downward FAC persists in the Northern Hemisphere (Figure 4.5b). $\nabla\cdot\mathbf{J}_{\|}$ is, in general, positive (Figure 4.5c), but $\partial J_{\|}/\partial t$ is almost zero (Figure 4.5d). $\mathbf{V}\cdot\mathbf{F}_t$ is negative all the way along the trajectory of the Alfvén wave packet (Figure 4.5e). This is also clearly demonstrated in the right panel of Figure 4.5, that is, the packet that we traced is located in the structure with $\mathbf{V}\cdot\mathbf{F}_t < 0$ (region 3). This structure is expanding from the magnetospheric boundary shown in Figure 4.1e. Figure 4.5e shows that $S_{\|}$ is negative at distance less than 3.3 R_E, which means that the magnetic energy flows in the direction anti-parallel to the **B** field. The FAC may be generated in the ionosphere and flows into the magnetosphere. It is thus speculated, on the basis of careful diagnosis, that there is no generation of Alfvén waves and the FACs in this region in the magnetosphere. We will discuss the FAC dynamo 1 and 2 in the following section.

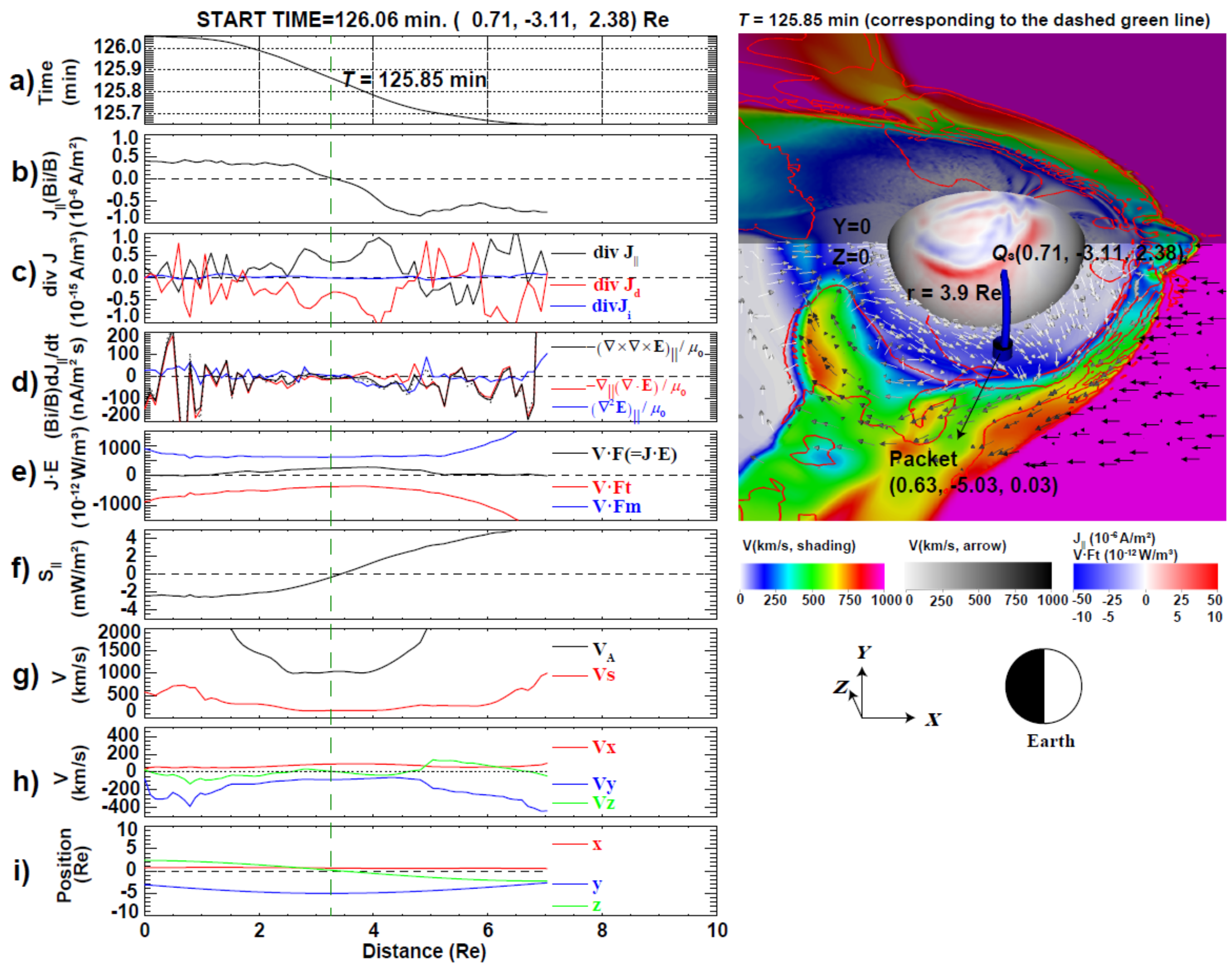

Figure 4.5 Same as Figure 4.3 except for the trace started backward in time from point Q_3 at T = 126.06 min, and the snapshot is taken at T = 125.85 min.

4.3.4 Mechanism of generation

In Figures 4.3 and 4.4, the generation of upward and downward FACs are identified, which corresponds to FAC dynamo 1 and 2, respectively. The former one is associated with PI, and the latter one is associated with MI, both on the dawnside. The associated generation mechanism is interpreted based on the results shown in Figure 4.6 and Figure 4.7 for upward and downward FACs separately. For Figure 4.6, as to the upward FAC (Figure 4.6a), it is found that the acceleration in the *x*-direction A_x and in the *y*-direction A_y (Figure 4.6d and Figure 4.6f) is dominated by the Lorentz force ($\mathbf{J} \times \mathbf{B}$). The Lorentz force consists of the magnetic pressure force ($\mathbf{F}_m$) and the magnetic tension force ($\mathbf{F}_t$) as shown in Figure 4.6e and 4.6g. The former term contributes to the acceleration a little more than the latter. The plasma pressure force ($\mathbf{F}_p = -\nabla P$, where P is plasma pressure) almost has no effect on the acceleration of plasma during the generation of upward FACs. Figure 4.6b indicates that the perpendicular current is dominated by the inertia current, which is also suggested by Fujita & Tanaka (2022). The physical process here is supposed to be as follows. The plasma in front of the compressional wave is accelerated by the Lorentz force, especially the magnetic pressure force. The field line is bent due to frozen-in theorem. The magnetic tension appears in the field line. The plasma performs negative work against the tension force because $\mathbf{V}$ (accelerated by $\mathbf{F}_m$) is opposite to the tension force ($\mathbf{F}_t$) and then Alfvén waves are generated.

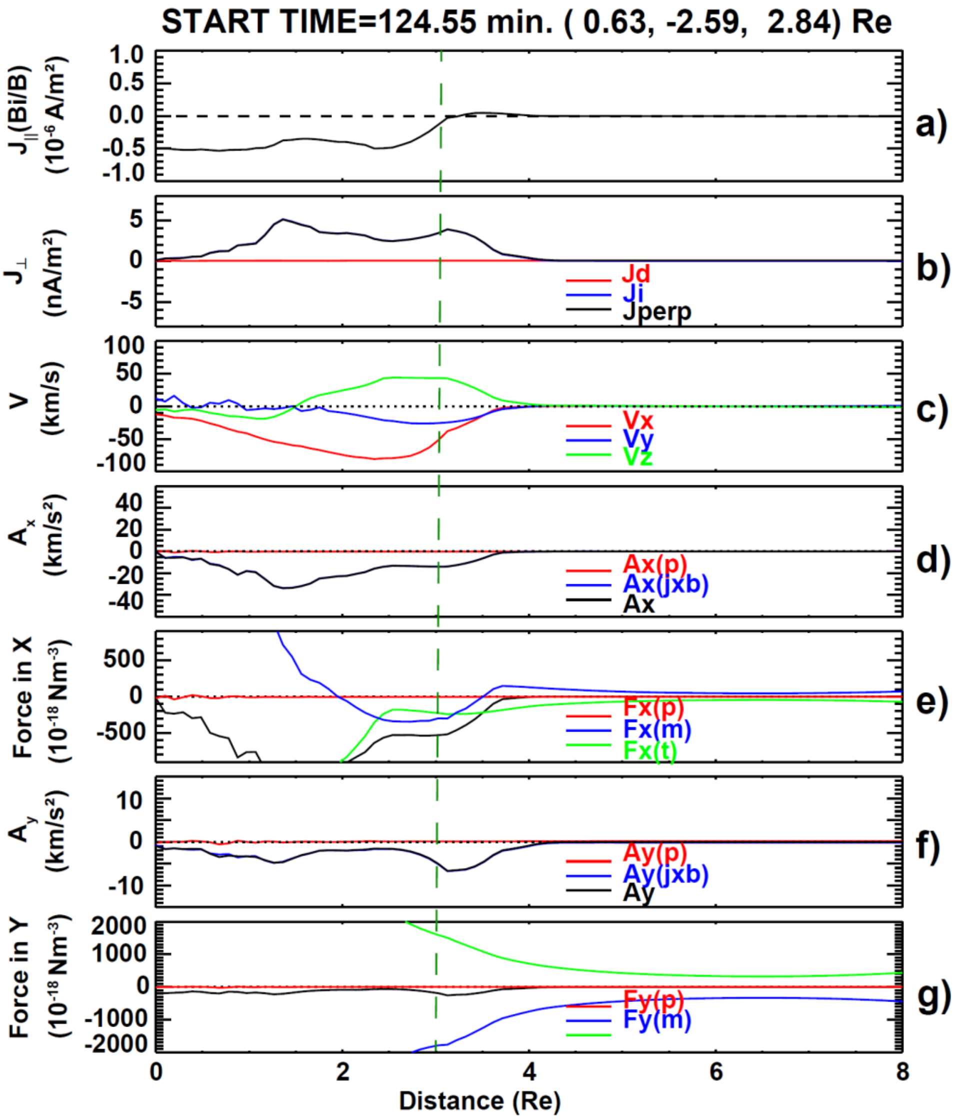

Figure 4.6 Quantities taken along the trajectory of the packet of the Alfvén wave associated with PI. (a) Normalized field-aligned current (FAC) (B_i/B) $J_{\|}$ (positive parallel and negative anti-parallel to the magnetic field), (b) magnitude of perpendicular currents, including the diamagnetic current $\mathbf{J}_d$ and the inertial current $\mathbf{J}_i$, (c) velocity $\mathbf{V}$, (d) x-component of the acceleration A_x, (e) x-component of the force, where $\mathbf{F}_p$, $\mathbf{F}_t$ and $\mathbf{F}_m$ are the plasma pressure force, the magnetic tension force and the magnetic pressure force, respectively, (f) y-component of the acceleration A_y, (g) y-component of the force. These quantities are taken along the packet that arrived at P_1 at 124.55 min, at which the upward FAC ($J_{\|} < 0$, PI-associated FAC on the dawnside) flows.

Figure 4.7 summarizes the relevant quantities for the case of the generation of downward FACs (MI-associated FACs on the dawnside), corresponding to Figure 4.4. A large amount of the FACs are connected with the diamagnetic current as shown in Figure 4.4c, but the magnitude of the diamagnetic current is smaller than that of the inertial current as shown in

Figure 4.7b, which may imply that the magnitude of the currents (the inertial current $\mathbf{J}_d$ and the diamagnetic current $\mathbf{J}_i$) does not immediately mean the degree of connection of the FAC. The acceleration is mostly in $+x$ direction because of the strong magnetic tension force as indicated in Figure 4.7d and 4.7f. The magnitude of $\mathbf{F}_t$ is increasing with the curvature of $\mathbf{B}$ field lines. In this case, the plasma behind the wave front in the equatorial plane is greatly decelerated due to the enhanced tension force.

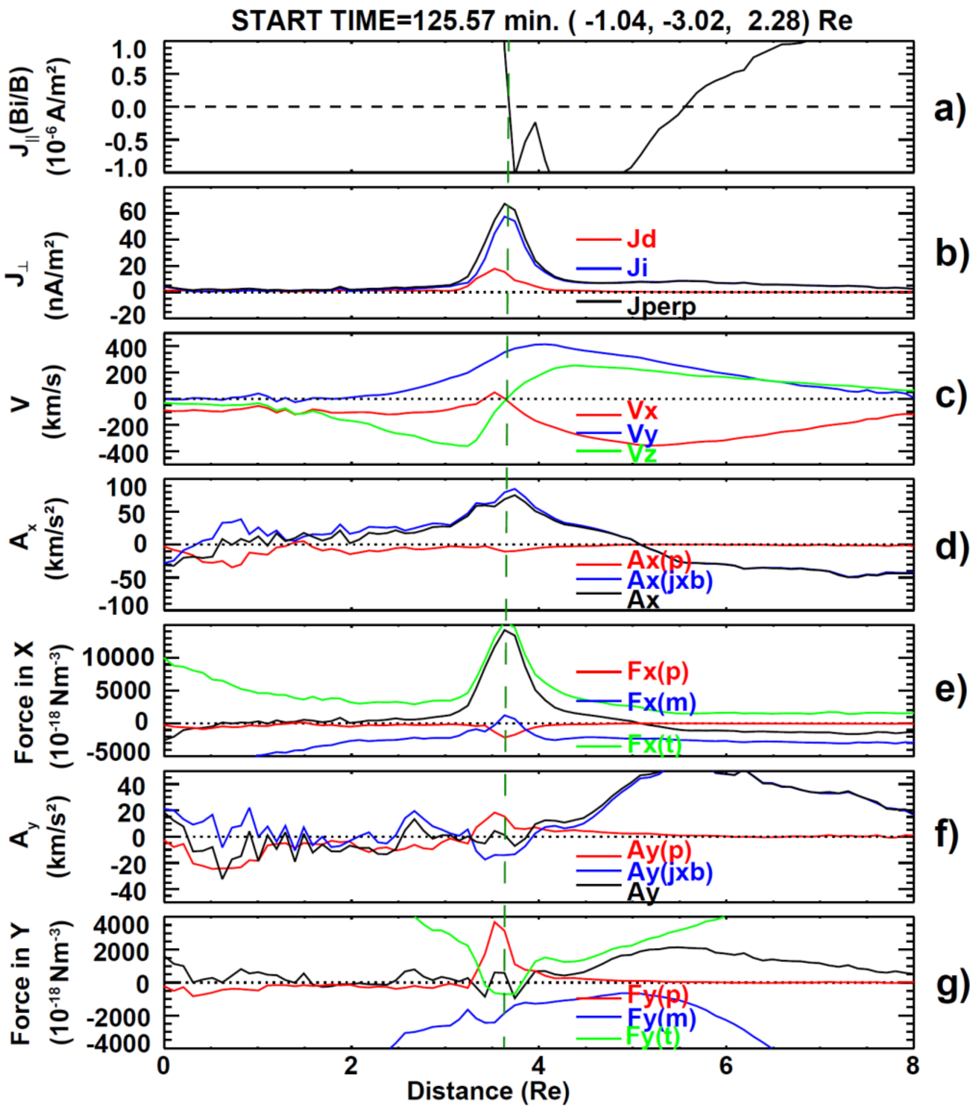

Figure 4.7 Same as Figure 4.6 except for the trajectory of the packet of the Alfvén wave associated with MI. These quantities are taken along the packet that arrived at P_2 at 125.57 min, at which the downward FAC ($J_{\|} > 0$, MI-associated FAC on the dawnside) flows.

4.3.5 Polarity of FACs

It is noticed that the FACs have opposite flowing directions not only during PI and MI phases, but also on the dawnside and duskside. The immediate question is what determines the polarity of the FACs. The polarization of the FAC is determined by Equation (4.4). The second term on the right-hand side of (4.10) are negative in the generation regions of PI and MI as shown in Figure 4.3 and Figure 4.4. That is, the first term on the right-hand side of (4.4), $-\nabla_{\|}(\nabla\cdot\mathbf{E})/\mu_0$, could determine the polarity of the FAC.

According to Equation (4.4) and the ideal MHD assumption ($\mathbf{E}=-\mathbf{V}\times\mathbf{B}$), we have (when only $\mathbf{E}_{\perp}$ is present)

$$\begin{aligned}\nabla\cdot\mathbf{E}_{\perp} &= \nabla\cdot\left(-\mathbf{V}_{\perp}\times\mathbf{B}\right)\\ &= -\mathbf{B}\cdot(\nabla\times\mathbf{V}_{\perp}) + \mathbf{V}_{\perp}\cdot(\nabla\times\mathbf{B})\\ &= -\mathbf{B}\cdot\mathbf{\Omega}_{\|} + \mu_0\mathbf{V}_{\perp}\cdot\mathbf{J}.\end{aligned} \tag{4.10}$$

where the vorticity is defined as $\mathbf{\Omega}\equiv\nabla\times\mathbf{V}_{\perp}$. Taking the divergence of both sides, we have

$$-\nabla_{\|}(\nabla\cdot\mathbf{E}_{\perp}) = \nabla_{\|}(\mathbf{B}\cdot\mathbf{\Omega}_{\|}) - \mu_0\nabla_{\|}(\mathbf{V}_{\perp}\cdot\mathbf{J}). \tag{4.11}$$

Equation (4.11) indicates that the term $-\nabla_{\|}(\nabla\cdot\mathbf{E})/\mu_0$ consists of two terms. One is associated with the gradient of $(\mathbf{B}\cdot\mathbf{\Omega}_{\|})$ in the parallel direction, and the other one is associated with the gradient of the dot product of the velocity and the current density in the parallel direction. The gradient in the parallel direction $\nabla_{\|}$ is calculated based on the localized magnetic field. Since the packet of the Alfvén wave does not move along the magnetic field line, we traced the magnetic field lines starting from the locations of packets in Figure 4.3 (1.15, -5.57, 2.70) R_E and Figure 4.4 (-2.98, -4.78, 0.02) R_E, separately. These points correspond to the generation regions of the PI and MI FACs, respectively.

Figure 4.8 shows the quantities along the magnetic field line from the generation regions of PI and MI FACs. In the vicinity of the generation region (starting from the leftmost where the tracing distance is zero), three criteria are met as shown in Figure 4.8b, 4.8c and 4.8d. As discussed previously in Section 4.3.3, the polarity of the time derivative of FACs is determined by the gradient of $-\nabla_{\|}(\nabla\cdot\mathbf{E})$ as indicated in Figure 4.8e. Figure 4.8f shows that $(\nabla\times\mathbf{V})_{\|}$ with an opposite sense of $(\nabla\cdot\mathbf{E})$ is increasing/decreasing for PI/MI case. According to (4.11), $-\nabla_{\|}(\nabla\cdot\mathbf{E})$ also consists of two components, $\nabla_{\|}(\mathbf{B}\cdot\mathbf{\Omega}_{\|})$ and $\nabla_{\|}(\mathbf{V}_{\perp}\cdot\mathbf{J})$. It is found that for PI FAC, the contribution from $\nabla_{\|}(\mathbf{B}\cdot\mathbf{\Omega}_{\|})$ is dominant, and that for MI FAC, the contribution from $\nabla_{\|}(\mathbf{V}_{\perp}\cdot\mathbf{J})$ plays an important role. The features of terms $(\nabla\times\mathbf{V})_{\|}$ and $(\mathbf{V}_{\perp}\cdot\mathbf{J})$ will be explained in detail later.

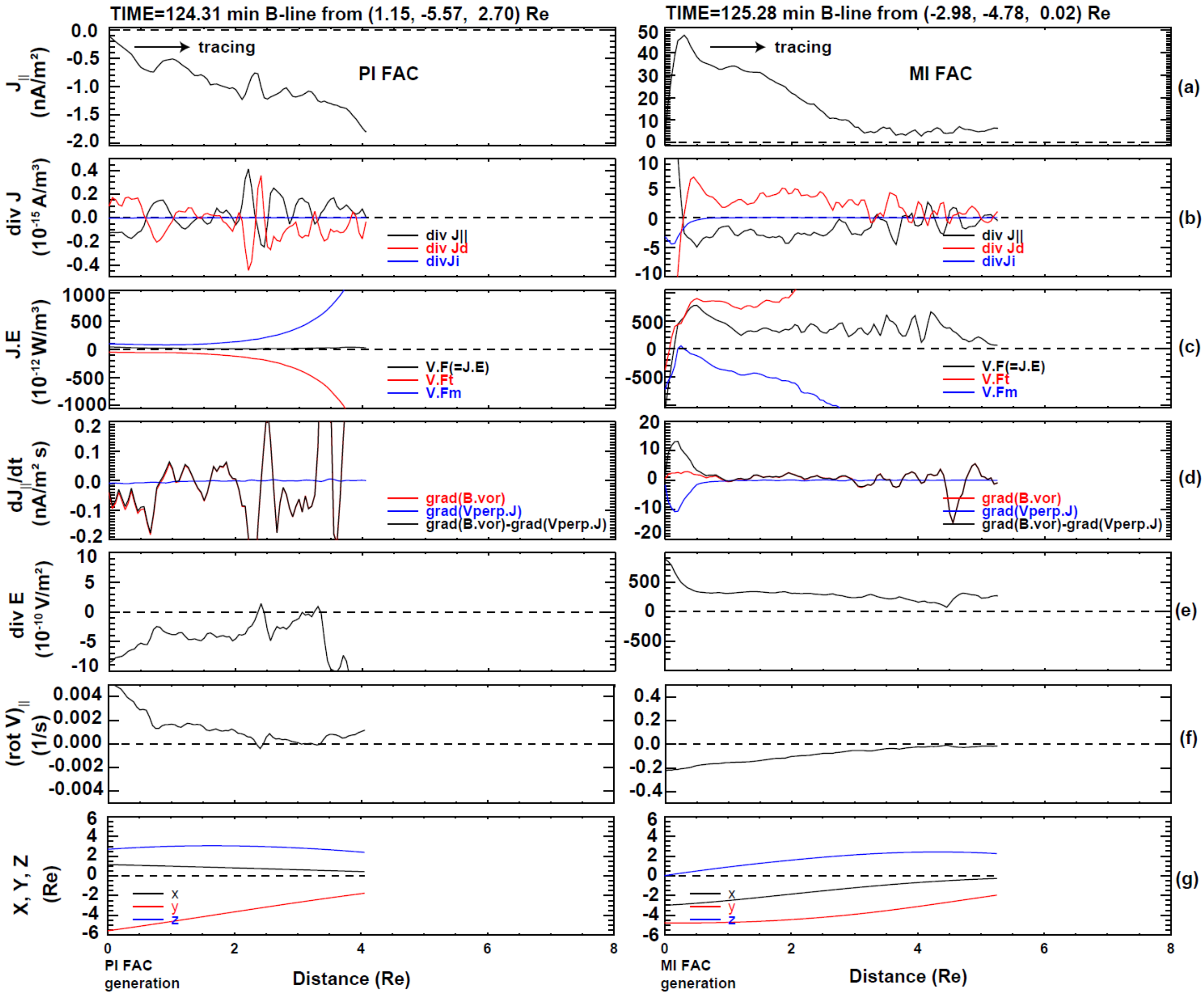

Figure 4.8 Quantities taken along the field line extending from the packets of Alfvén wave associated with PI (left) and MI (right) FAC generation. (a) field-aligned current (FAC) $J_{\|}$ (positive parallel and negative anti-parallel to the magnetic field), (b) $\nabla \cdot \mathbf{J}_{\|}$, $\nabla \cdot \mathbf{J}_d$, and $\nabla \cdot \mathbf{J}_i$, where $\mathbf{J}_{\|}$, $\mathbf{J}_d$ and $\mathbf{J}_i$ are the FAC, the diamagnetic current and the inertial current, respectively, (c) $\mathbf{J} \cdot \mathbf{E}$ (black), $\mathbf{V} \cdot \mathbf{F}_t$ (red) and $\mathbf{V} \cdot \mathbf{F}_m$ (blue), where $\mathbf{F}_t$ and $\mathbf{F}_m$ are the magnetic tension force and the magnetic pressure force, respectively, (d) time rate of change in the FAC, $-\nabla_{\|}(\nabla \cdot \mathbf{E}_{\perp})$, consists of $\nabla_{\|}(\mathbf{B} \cdot \boldsymbol{\Omega}_{\|})$ (red line) and $\nabla_{\|}(\mathbf{V}_{\perp} \cdot \mathbf{J})$ (blue line), (e) $\nabla \cdot \mathbf{E}$, (f) parallel vorticity $(\nabla \times \mathbf{V})_{\|}$, and (g) position (x, y, z) R_E.

Figure 4.9 shows the magnetic pressure in the equatorial plane and $(\nabla \times \mathbf{V})_{\|}$ in the x-y plane at different z. At T = 123.64 min before the generation of PI FACs, the compressional wave that is characterized by high magnetic pressure is shown in Figure 4.9a. Both the distributions of $(\nabla\times\mathbf{V})_{\parallel}$ at z = 0 and z = 2.7 R_E are similar at the early stage (T = 123.64 min). At this moment, the disturbances associated with the compressional wave have not reached the ionosphere, and FACs in the ionosphere remain low. About half a minute later (T = 124.23 min), the distribution of the magnetic pressure is largely changed by the propagation of the compressional wave as shown in Figure 4.9b. Together with the Earth's intrinsic magnetic field, the gradient of the magnetic pressure gives rise to the varied distribution of $(\nabla\times\mathbf{V})_{\parallel}$ according to the two right panels in Figure 4.9b. This bump of the high-magnetic pressure region near the equatorial plane coincides with the distribution of $(\nabla\times\mathbf{V})_{\parallel}$ in the equatorial plane. At low z-values (z = 0), on the dawnside, the opposite vorticity appears earthward (negative) and anti-earthward (positive) of the protruding high magnetic pressure region in the equatorial plane. At high z-values (z = 2.7 R_E), $(\nabla\times\mathbf{V})_{\parallel} > 0$ is still dominant at the wave front because there is no such protrusion. The positive vorticity decreases along the field line, which causes the generation of the upward FAC as shown in Figure 4.8.

For MI FACs, the contribution from $\nabla_{\parallel}(\mathbf{V}_{\perp}\cdot\mathbf{J})$ is dominant. Figure 4.10 shows the current density $\mathbf{J}$ and plasma flow velocity $\mathbf{V}$ in the equatorial plane at the moment of MI FAC generation (T = 125.28 min). Near the generation region (-3.0, -4.8, 0) R_E, it is found the current (black arrows) is flowing westward on both dawn and dusk sides. The plasma flow (white arrows) is westward on the dawnside, and eastward on the duskside, which causes the dawn-dusk asymmetry in the result of the dot product.

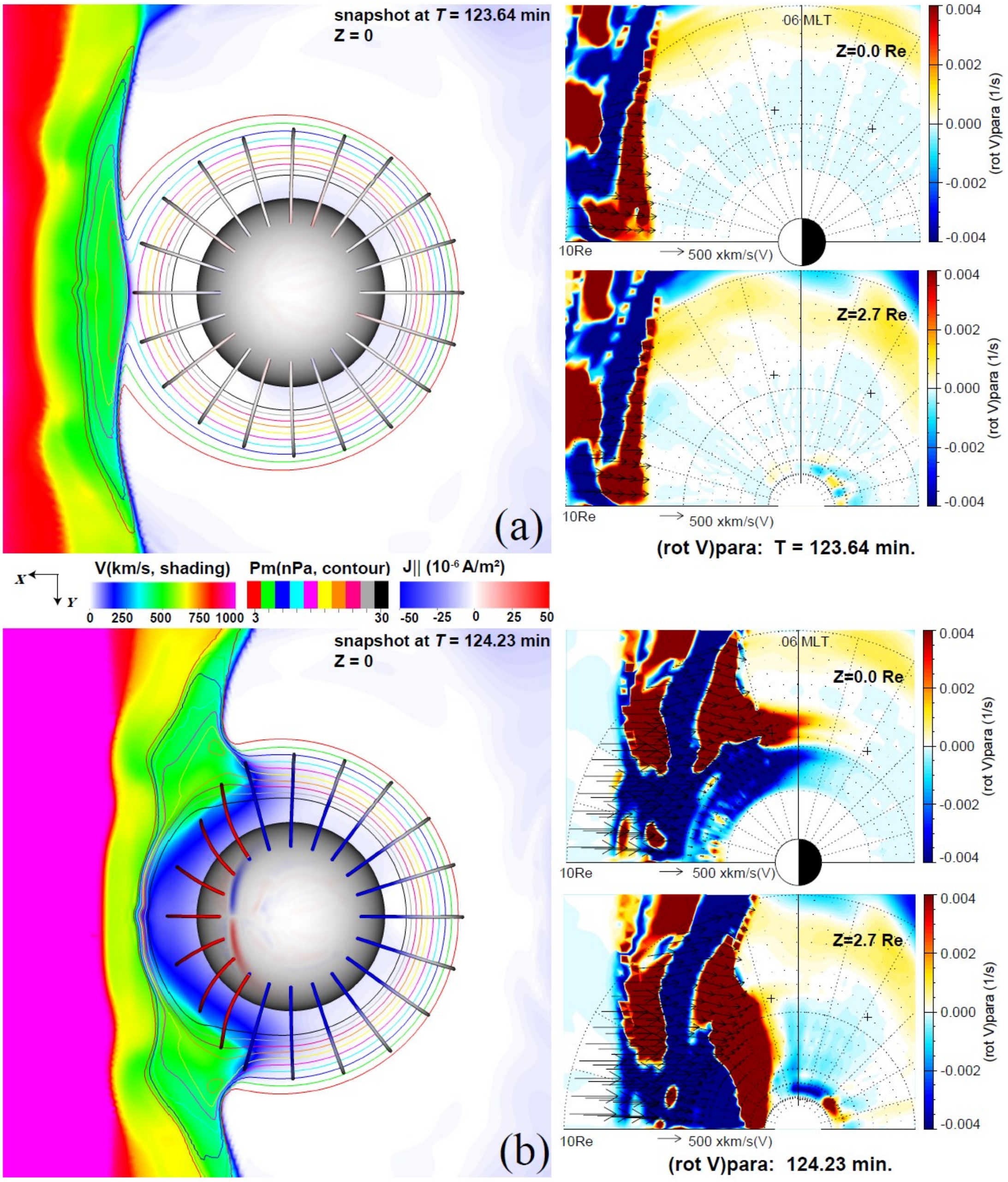

Figure 4.9 A view from the magnetic north pole. The magnetic pressure structure (contour lines), plasma velocity (color shadings), and field lines are shown in the left column. The distribution of $(\nabla\times\mathbf{V})_{\parallel}$ at different $z = 0$ and $z = 2.7\ R_E$ (two panels on the right). The Sun is to the left. Sub-figure (a) is taken at T = 123.64 min; (b) at 124.23 min.

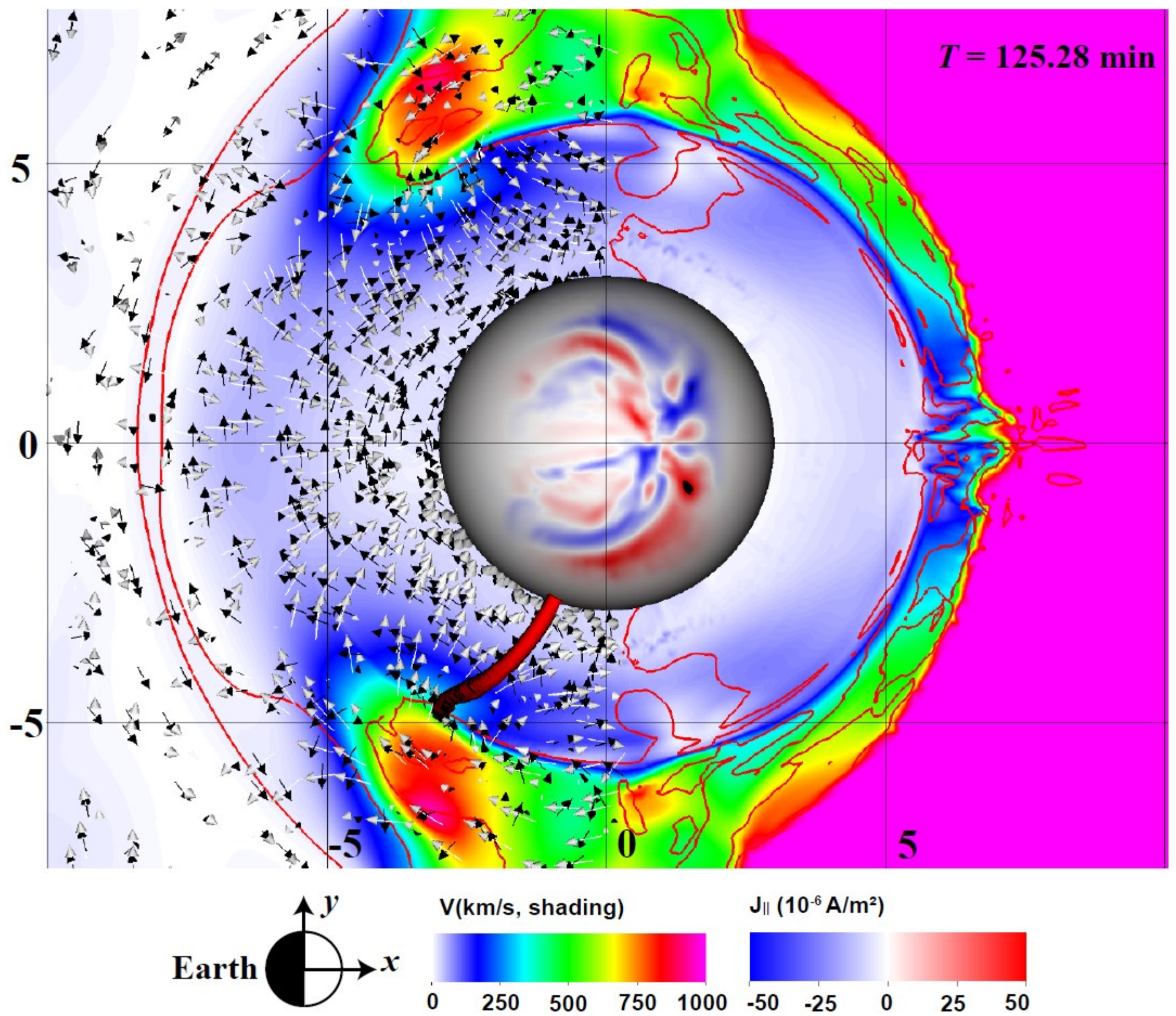

Figure 4.10 A view from the magnetic north pole at T = 125.28 min. MI FAC is generated where the reddish thick tube crosses the x-y plane. The Sun is to the right. Color bars show the plasma flow velocity in the equatorial plane and the intensity of $J_{\|}$ mapped to the sphere 3 R_E. Red curves indicate where $\mathbf{V}\cdot\mathbf{F}_t = 0$. White and black arrows represent the direction of plasma flow and current in the equatorial plane, separately.

4.4 Discussions and Summary

We identified the FAC dynamos associated with the SC by tracing Alfvén wave packets. According to the simulation results above, the PI FACs are generated in FAC dynamo 1 that is at the wavefront and off the equator due to the acceleration by the magnetic pressure force, and MI FACs are generated in the equatorial plane where FAC dynamo 2 is located due to the enhanced magnetic tension force that decelerates the plasma. The shape of wavefront in the magnetosphere is not a plane as indicated by Samsonov & Sibeck (2013), and the non-uniformity at different z-values (distance from the equatorial plane) leads to the different distribution of $(\nabla\times\mathbf{V})_{\parallel}$ through the Lorentz force (including both magnetic pressure force and tension force) that determines the polarity of PI FACs. MI FACs are downward/upward on the dawnside/duskside due to the great contribution from $\nabla_{\parallel}(\mathbf{V}_{\perp}\cdot\mathbf{J})$ in the equatorial plane, which may be associated with the rapid enhancement of perpendicular currents in the generation region.

The generation region was identified by the condition $\mathbf{J}\cdot\mathbf{E} < 0$ in many previous studies (e.g. Fujita et al., 2003a, 2003b; Samsonov et al., 2010). By tracing the current lines, Fujita et al. (2003a) indicated that the PI-associated current is generated in the magnetopause where $\mathbf{J}\cdot\mathbf{E}$ is negative. They point out that at the wavefront region, electromagnetic forces push the plasma, which makes $\mathbf{J}\cdot\mathbf{E}$ become positive. Similarly, Samsonov et al. (2010) found that the plasma is accelerated in the region near the magnetopause where $\mathbf{J}\cdot\mathbf{E} > 0$, and they attributed the dynamo region to the reconfiguration of the magnetic field near the magnetopause. As shown in Figure 4.3e, $\mathbf{J}\cdot\mathbf{E}$ is indeed positive because the magnitude of $\mathbf{V}\cdot\mathbf{F}_m$ (which is positive) is larger than that of $\mathbf{V}\cdot\mathbf{F}_t$ (which is negative). The plasma is then accelerated by the magnetic pressure force at the wavefront. The motion of the accelerated plasma gives rise to the bend of magnetic field lines due to the frozen-in theorem, which explains the reason why $\mathbf{V}\cdot\mathbf{F}_t$ is negative and PI FAC is generated as identified in Section 4.3.3. Thus, the term of $\mathbf{J}\cdot\mathbf{E}$ indicates the energy conversion though, it does not suggest the generation of FACs when the effect from the magnetic pressure force is present.

The generation of FACs associated with the pressure pulse is explained in terms of the PI and MI phases separately in previous studies. Fujita et al. (2003a) suggested that the PI current is converted from an enhanced magnetopause current along the compressional wavefront due to the nonuniformed plasma. The mode conversion takes place in the region where there is a steep gradient of V_A. Their conculsion that the current in the wavefront region is an inertia current, is simialr with the dominance of the inertial current in the dynamo region in our simulation as illustrated in Figures 4.6b and 4.7b. According to the divergence of the currents shown in Figures 4.3c and 4.4c, a large amount of the FACs is connected with the diamagnetic current. Currently, we do not know the reason why FACs are mostly connected to the diamagnetic current, not the inertial current. Fujita & Tanaka, (2022) discussed the components of the divergence of the inertia current and the possible mechanisms on the basis of tracing the current lines. This method may result in the different conclusion with that using the method of tracing an Alfvén wave packet (Ebihara & Tanaka, 2024).

The generation mechanism of MI FACs was interpreted as an isolated enhancement of plasma pressure in the equatorial plane, caused by the compression of the magnetospheric flank due to the solar wind impulse, which gives rise to a plasma convection vortex subsequently (Fujita et al., 2003b, Fujita, 2019). In-situ observations of magnetospheric vortex on both the dayside and nightside are reported (Shi et al. 2014; Tian et al. 2016 and the references therein). Yu and Ridley (2009) demonstrated that the magnetospheric flow vortex is driven by the plasma pressure gradient. It is found in our simulation that the vortex is moving with a high plasma pressure region in the equatorial plane together with the generation region of the MI FACs (not shown). This plasma flow vortex appears after the sudden compression of the magnetosphere and moves towards the nightside, which is called FAC dynamo 2 as shown in Figure 4.4. Samsonov & Sibeck, (2013) invesigated the large-scale flow vortex following a magnetospheric sudden impulse through global MHD simulations and suggested that this vortex near the Earth is caused by the interaction between the fast compressional wave and the inner boundary of the simulation model. They claimed that the inner boundary of the simulation model can be regarded as the plasmapause or the ionosphere. Further studies are needed to investigate the overall influence of the inner boundary of the simulation model. In addition, they indicated that the Lorentz force ($\mathbf{J}\times\mathbf{B}$) is involved in the formation of the vortex. The Lorentz force consists of magnetic pressure force ($\mathbf{F}_m$) and magnetic tension force ($\mathbf{F}_t$) according to Equation (4.7). The effect from the former/latter is dominant in the acceleration/deceleration of plasma respectively, which gives rise two different FAC dynamo regions as shown in our result.

The prominent difference between PI and MI FACs is the opposite flowing direction. The PI FAC is flowing out of the ionosphere and the MI FAC is flowing into it on the dawnside. The asymmetry exists not only at different phases (PI and MI), but also on the dawn and dusk side. According to our results, the asymmetry in PI/MI phase is due to the different generation mechanism that the polarity PI FACs is depending on the $\nabla_{\|}(\mathbf{B}\cdot\mathbf{\Omega}_{\|})$, and MI FAC is determined by $\nabla_{\|}(\mathbf{V}_{\perp}\cdot\mathbf{J})$. The magnitude of $\Omega_{\|}\nabla B$ is much smaller compared to $B\nabla\Omega_{\|}$ (not shown) in PI FAC generation region and $\nabla_{\|}(\mathbf{V}_{\perp}\cdot\mathbf{J})$ is almost zero in PI case. This implies that polarity of PI FACs is closely related with the field-aligned variation of parallel vorticity $\Omega_{\|}$, which also explains the dawn-dusk asymmetry of PI FACs. The dawn-dusk asymmetry of MI FACs is due to the perpendicular current flowing from dawn to dusk (westward) in the equatorial plane, and plasma flow is westward/eastward on dawn/dusk side as shown in Figure 4.10, which causes the dot product ($\mathbf{V}_{\perp}\cdot\mathbf{J}_{\perp}$) is positive on the dawnside and negative on the duskside. When the strength of MI FACs is enhanced, the gradient will have a different polarity. Many previous studies thought that $\nabla\cdot\mathbf{E}_{\perp}$ is associated with a perpendicular vortex or shear motion ($\Omega_{\|}$), when $\mathbf{V}_{\perp}\cdot\mathbf{J}_{\perp}$ is omitted (e.g., Araki, 1994; Song & Lysak, 2001; Fujita et al. 2003b; Yu & Ridley, 2009). However, it should be noted that this may be reasonable only for PI case, and the perpendicular current is increasing quickly during MI phase that gives rise to the large field-aligned gradient of $\mathbf{V}_{\perp}\cdot\mathbf{J}_{\perp}$, so it makes the contribution from the term $\nabla_{\|}(\mathbf{V}_{\perp}\cdot\mathbf{J})$ nonnegligible and significant as shown in Figure 4.8d for the MI case.

For the Region 3 in Figure 4.1, it is found at the very late stage of the MI phase (after 125.14 min) that the negative $\mathbf{V}\cdot\mathbf{F}_t$ region would take over the entire near-Earth space, expanding from near the dayside magnetopause to the magnetotail. This may be explained by the enhanced dawn-to-dusk electric field in the compressed magnetosphere. After the passage of the compressional wavefront towards the nightside, the magnetospheric convection adjusted to the new compressed state of the magnetosphere, since the dynamic pressure of the solar wind remains high due to the continuous high-velocity/density flow in the MHD simulation (Tohru Araki, 1994). However, in this case, the time rate of change in FACs is quite minor as shown in Figure 4.5d, compared to Figures 4.3d and 4.4d, even though $\mathbf{V}\cdot\mathbf{F}_t$ is negative all along with the expansion. It is thought that the Alfvén wave packet would have a chance to capture the generation information of FACs several times, or say it is the intersection of different packets in the same region (Ebihara & Tanaka, 2022). Another possibility is that the FAC is generated in the ionosphere, since $S_{\|}$ is negative along the trajectory as seen in Figure 4.5f, indicating that the energy flows from the ionosphere into the magnetosphere. It is thus speculated that there is no generation of FACs in this region in the magnetosphere, given that the three criteria are not all satisfied.

In this study, three criteria are used to identify the generation of the FAC (dynamo) in response to the solar wind dynamic pressure pulse. The generation region and mechanism are interpreted from the perspective of the possible dynamo regions ($\mathbf{V} \cdot \mathbf{F}_t < 0$). The general process of FAC generation associated with the pulse could be summarized as follows.

1. When the solar wind dynamic pressure hits the magnetopause, a compressional wave is excited.
2. As the compressional wave propagates tailward in the magnetosphere, the wavefront forms a protruding part near the equatorial plane. Plasma is accelerated by the magnetic pressure force, and the accelerated plasma pulls the magnetic field line. Alfvén waves are excited, and PI-associated FACs are generated off the equator (FAC dynamo 1).
3. As the compressional wave further propagates, the magnetic field lines are extremely curved, causing the enhancement of magnetic tension force that results in a plasma flow shear. The tension force recovers the bend and gives rise to strong MI-associated FACs due to $\mathbf{V} \cdot \mathbf{F}_t < 0$ (FAC dynamo 2).
4. The polarity of PI FACs is determined by the field-aligned variation of $(\nabla\times\mathbf{V})_{\|}$, and polarity of MI FACs is decided by the gradient of $(\mathbf{V}_{\perp} \cdot \mathbf{J})$ in the parallel direction.

Some unsettled issues, like the role of the inner boundary and what determines the connection among FACs, diamagnetic currents and inertial currents, remain for further studies. It is also necessary to investigate in the future the probable instabilities in the magnetosheath and kinetic effects, which may affect the morphology of the compressional wavefront.

Chapter 5 Conclusion and Prospect

5.1 Conclusion

Based on the study, the major conclusions in the thesis are summarized as follows:

1. Using the geoelectric field measured at Kakioka Geomagnetic Observatory as a proxy for geomagnetically induced currents (GIC), we clarified the relationship between geomagnetic variations and the geoelectric field for three main types of geomagnetic variations in Japan: sudden commencements (SC), geomagnetic storms, and bay-type variations. We showed that the maximum amplitude of the geoelectric field is largest during SC, followed by geomagnetic storms and bay-type variations, and that there is a linear relationship between the maximum amplitude of geomagnetic variations and the maximum amplitude of the geoelectric field, and derived the proportionality constant. Extreme value analysis was performed using the generalized extreme value distribution (GEVD) method to obtain the maximum amplitude of the geoelectric field over a 10-year and 100-year return period.

2. Using magnetohydrodynamic (MHD) simulations, we succeeded in reproducing the geomagnetic fluctuations that occurred when a widespread blackout occurred in Canada in March 1989 due to a GIC. We showed that an interplanetary shock wave arrived, generating an SC, which caused a strong current associated with main impulse (MI) to flow in the ionosphere, significantly disrupting the geomagnetic field and causing the widespread blackout in Canada. The important role played by SCs in generating large GICs is pointed out and the attention should be paid to the effects on power systems.

3. Using MHD simulations, we succeeded in identifying the cause of field-aligned currents (FACs) that increase with SCs and the region in which they are generated. The generation mechanism is proposed and the difference in polarity of FACs is also analyzed. We showed the details of the entire physical process from the interplanetary shock compressing the magnetosphere, to the FACs generated in the magnetosphere connecting with the ionosphere, intensifying ionospheric currents and disrupting the magnetic field on the ground, and clarified the fundamental cause of the widespread blackout that occurred in Canada in March 1989.

5.2 Prospect

To fully accomplish the global map of geomagnetic/geoelectric response on the ground, it is expected to further study the detailed geomagnetic response to ring current and substorms at different latitudes in combination with both simulations and observations. For sudden commencements, the DL-component affected by the magnetopause current deserves more study as well. In addition, the prediction work of GIC amplitude under extreme conditions attracts lots of attention, which is also a good direction in the future. In the scope of space weather, understanding origins, propagation and interactions of solar-produced processes within geospace is always the topic, and forecasting the space weather is the purpose based on these studies. Analysis of impacts on the technical systems, including e.g. telecommunications, transportation, electric power grids, satellite navigation, are useful practical applications.

Appendix A

A.1 Comparison between the contribution of Hall currents, Pedersen currents and FACs to variations of ground magnetic northward component Bx during SCs

Tab. A.1 summarizes the B_x disturbances caused by the ionospheric Hall current, the Pedersen current and the field-aligned current for Run-33n (1000 km/s, 50/cc) at 4 specific locations distributed in the four different time sectors. The B_x for each location is taken at the moment when the ionospheric current reaches the maximum during the SC. Fig. A.**1** shows the temporal variations of B_x along 3 MLT at different MLATs for the northward IMF cases. We could find through the table and figure that the contribution to the disturbances is dominated by the ionospheric Hall current. The effect of Pedersen currents is calculated in a similar way with that of Hall currents. The FACs inside the inner boundary (from 3 to 1.016 Re) of the global MHD simulation are mapped from the sphere at the geocentric distance at 3 Re along the dipole magnetic field lines. The focus of Chapter 3 is on the magnetic disturbances around 60 MLATs. We can safely consider that the contribution from the FACs to the magnetic disturbances around 60 MLATs is most likely minor for these locations. The reason is that the ionospheric Hall current flows over there. We expect that the contribution from the FACs becomes major at low latitudes as Ohtani (2022) pointed out. We are currently investigating the contribution from the FACs, and more details about this topic would be explained and discussed in the future.

Tab. A.1 Northward component of the magnetic disturbances on the ground B_x caused by the Hall current, the Pedersen current and the FAC.

Location (MLAT in degree, MLT in hour)	MHD time (min)	B_x - Hall (nT)	B_x - Pedersen (nT)	B_x - FAC* (nT)
(60, 09) pre-noon	124.23 (PI)	53.8	-14.4	13.0
(60, 15) post-noon	124.23 (PI)	-134.7	-6.9	15.9
(60, 21) pre-midnight	126.87 (MI)	171.1	-1.7	19.6
(60, 03) post-midnight	126.46 (MI)	-378.0	-0.9	31.0

*FACs within the distance of 3 Re to the point of interest on the ground are taken into consideration.

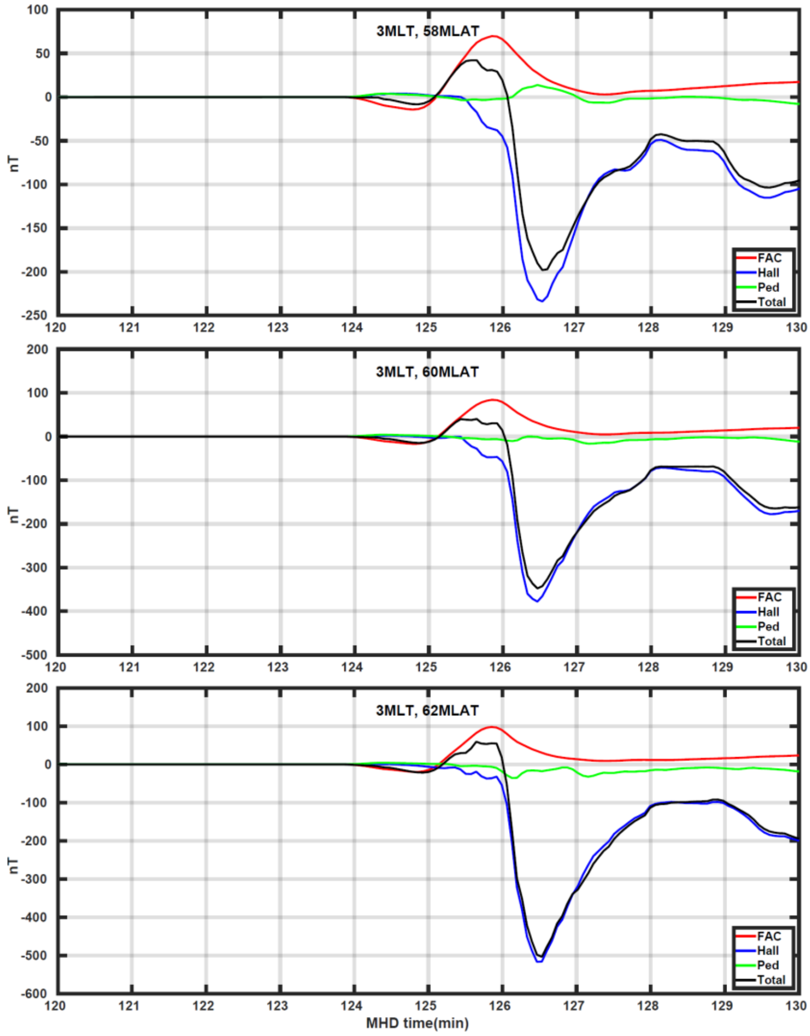

Fig. A.1 Contributions to the northward component of the magnetic perturbation B_x from FAC, Hall current and Pedersen current of Run-33n (1000 km/s, 50/cc). Total shows the sum of the three components. The panels from top to bottom indicate the variations taken at MLAT = 58, 60, and 62 when MLT = 3, respectively.

References

Akasofu, S.-I., & Meng, C.-I. (1969). A study of polar magnetic substorms. *Journal of Geophysical Research*, *74*(1), 293–313. https://doi.org/10.1029/JA074i001p00293

Allen, J., Sauer, H., Frank, L., & Reiff, P. (1989). Effects of the March 1989 solar activity. *Eos, Transactions American Geophysical Union*, *70*(46), 1479. https://doi.org/10.1029/89EO00409

Araki, T., Takeuchi, T., & Araki, Y. (2004). Rise time of geomagnetic sudden commencements-Statistical analysis of ground geomagnetic data-. *Earth, Planets and Space*, *56*(2), 289–293. https://doi.org/10.1186/BF03353411

Araki, T., Keika, K., Kamei, T., Yang, H., & Alex, S. (2006). Nighttime enhancement of the amplitude of geomagnetic sudden commencements and its dependence on IMF-Bz. *Earth, Planets and Space*, *58*(1), 45–50. https://doi.org/10.1186/BF03351912

Araki, T. (2014). Historically largest geomagnetic sudden commencement (SC) since 1868. *Earth, Planets and Space*, *66*(1), 1–6. https://doi.org/10.1186/s40623-014-0164-0

Araki, Tohru. (1994). *A Physical Model of the Geomagnetic Sudden Commencement*. (M. J. Engebretson, K. Takahashi, & M. Scholer, Eds.). Washington, D. C.: American Geophysical Union.

Araki, Tohru, Allen, J. H., & Araki, Y. (1985). Extension of a polar ionospheric current to the nightside equator. *Planetary and Space Science*, *33*(1), 11–16. https://doi.org/10.1016/0032-0633(85)90137-0

Bartels, J., Heck, N. H., & Johnston, H. F. (1939). The three-hour-range index measuring geomagnetic activity. *Terrestrial Magnetism and Atmospheric Electricity*, *44*(4), 411–454. https://doi.org/10.1029/TE044i004p00411

Boteler, D. (2015). The Evolution of Québec Earth Models Used to Model Geomagnetically Induced Currents. *IEEE Transactions on Power Delivery*, *30*(5), 2171–2178. https://doi.org/10.1109/TPWRD.2014.2379260

Boteler, D., & Jansen, B. (1993). Mapping the March 13 , 1989 , Magnetic Disturbance and its Consequences Across North America. In *Solar-Terrestrial Predictions Workshop, 1993* (pp. 57–70).

Boteler, D. H. (2019). A 21st Century View of the March 1989 Magnetic Storm. *Space Weather*, *17*(10), 1427–1441. https://doi.org/10.1029/2019SW002278

Boteler, D. H., & Pirjola, R. J. (2017). Modeling geomagnetically induced currents. *Space Weather*, *15*(1), 258–276. https://doi.org/10.1002/2016SW001499

Boudouridis, A., Lyons, L. R., Zesta, E., Weygand, J. M., Ribeiro, A. J., & Ruohoniemi, J. M. (2011). Statistical study of the effect of solar wind dynamic pressure fronts on the dayside and nightside ionospheric convection. *Journal of Geophysical Research: Space Physics*, *116*(10). https://doi.org/10.1029/2011JA016582

Burton, R. K., McPherron, R. L., & Russell, C. T. (1975). An empirical relationship between interplanetary conditions and Dst. *Journal of Geophysical Research*, *80*(31), 4204–4214. https://doi.org/10.1029/JA080i031p04204

Cagniard, L. (1953). BASIC THEORY OF THE MAGNETO-TELLURIC METHOD OF GEOPHYSICAL PROSPECTING. *GEOPHYSICS*, *18*(3), 605–635. https://doi.org/10.1190/1.1437915

Carter, B. A., Yizengaw, E., Pradipta, R., Halford, A. J., Norman, R., & Zhang, K. (2015). Interplanetary shocks and the resulting geomagnetically induced currents at the equator. *Geophysical Research Letters*, *42*(16), 6554–6559. https://doi.org/10.1002/2015GL065060

Carter, B. A., Yizengaw, E., Pradipta, R., Weygand, J. M., Piersanti, M., Pulkkinen, A., et al. (2016). Geomagnetically induced currents around the world during the 17 March 2015 storm. *Journal of Geophysical Research: Space Physics*, *121*(10), 10,496-10,507. https://doi.org/10.1002/2016JA023344

Cravens, T. E. (1997). *Physics of Solar System Plasmas*. Cambridge University Press. https://doi.org/10.1017/CBO9780511529467

Curto, J. J., Araki, T., & Alberca, L. F. (2007). Evolution of the concept of Sudden Storm Commencements and their operative identification. *Earth, Planets and Space*, *59*(11), i–xii. https://doi.org/10.1186/BF03352059

Dimmock, A. P., Rosenqvist, L., Welling, D. T., Viljanen, A., Honkonen, I., Boynton, R. J., & Yordanova, E. (2020). On the Regional Variability of d B /d t and Its Significance to GIC. *Space Weather*, *18*(8), 1–20. https://doi.org/10.1029/2020SW002497

Ebihara, Y., & Tanaka, T. (2015). Substorm simulation: Insight into the mechanisms of initial brightening. *Journal of Geophysical Research: Space Physics*, *120*(9), 7270–7288. https://doi.org/10.1002/2015JA021516

Ebihara, Y., Tanaka, T., & Kikuchi, T. (2014). Counter equatorial electrojet and overshielding after substorm onset: Global MHD simulation study. *Journal of Geophysical Research: Space Physics*, *119*(9), 7281–7296. https://doi.org/10.1002/2014JA020065

Ebihara, Yusuke, & Ejiri, M. (2003). Numerical simulation of the ring current: Review. *Space Science Reviews*, *105*(1–2), 377–452. https://doi.org/10.1023/A:1023905607888

Ebihara, Yusuke, & Tanaka, T. (2022). Where Is Region 1 Field-Aligned Current Generated? *Journal of Geophysical Research: Space Physics*, *127*(3), 1–15. https://doi.org/10.1029/2021JA029991

Ebihara, Yusuke, & Tanaka, T. (2023). Generation of Field-Aligned Currents During Substorm Expansion: An Update. *Journal of Geophysical Research: Space Physics*, *128*(2). https://doi.org/10.1029/2022JA031011

Ebihara, Yusuke, & Tanaka, T. (2024). Generation mechanism of Region 1 field-aligned current and energy transfer from solar wind to polar ionosphere. *Reviews of Modern Plasma Physics*, *8*(1), 20. https://doi.org/10.1007/s41614-024-00154-7

Ebihara, Yusuke, Lee, L., & Tanaka, T. (2020). Energy Flow in the Region 2 Field-Aligned Current Region Under Quasi-steady Convection. *Journal of Geophysical Research: Space Physics*, *125*(2). https://doi.org/10.1029/2019JA026998

Ebihara, Yusuke, Watari, S., & Kumar, S. (2021). Prediction of geomagnetically induced currents (GICs) flowing in Japanese power grid for Carrington-class magnetic storms. *Earth, Planets and Space*, *73*(1). https://doi.org/10.1186/s40623-021-01493-2

Echer, E., Gonzalez, W. D., & Tsurutani, B. T. (2011). Statistical studies of geomagnetic storms with peak Dst≤-50nT from 1957 to 2008. *Journal of Atmospheric and Solar-Terrestrial Physics*, *73*(11–12), 1454–1459. https://doi.org/10.1016/j.jastp.2011.04.021

Echer, E., Tsurutani, B. T., & Gonzalez, W. D. (2013). Interplanetary origins of moderate (-100 nT < Dst ≤ -50 nT) geomagnetic storms during solar cycle 23 (1996-2008). *Journal of Geophysical Research: Space Physics*, *118*(1), 385–392. https://doi.org/10.1029/2012JA018086

Engebretson, Mark J., Pilipenko, V. A., Steinmetz, E. S., Moldwin, M. B., Connors, M. G., Boteler, D. H., et al. (2021). Nighttime Magnetic Perturbation Events Observed in Arctic Canada: 3. Occurrence and Amplitude as Functions of Magnetic Latitude, Local Time, and Magnetic Disturbance Indices. *Space Weather*, *19*(3), 1–18. https://doi.org/10.1029/2020SW002526

Etemadi, A. H., & Rezaei-Zare, A. (2014). Optimal placement of GIC blocking devices for geomagnetic disturbance mitigation. *IEEE Transactions on Power Systems*, *29*(6), 2753–2762. https://doi.org/10.1109/TPWRS.2014.2309004

Fujii, I., Ookawa, T., Nagamachi, S., & Owada, T. (2015). The characteristics of geoelectric fields at Kakioka, Kanoya, and Memambetsu inferred from voltage measurements during 2000 to 2011. *Earth, Planets and Space*, *67*(1), 1–17. https://doi.org/10.1186/s40623-015-0241-z

Fujita, S., Tanaka, T., Kikuchi, T., Fujimoto, K., Hosokawa, K., & Itonaga, M. (2003a). A numerical simulation of the geomagnetic sudden commencement: 1. Generation of the field-aligned current associated with the preliminary impulse. *Journal of Geophysical Research: Space Physics*, *108*(A12), 1416. https://doi.org/10.1029/2002JA009407

Fujita, S., Tanaka, T., Kikuchi, T., Fujimoto, K., & Itonaga, M. (2003b). A numerical simulation of the geomagnetic sudden commencement: 2. Plasma processes in the main impulse. *Journal of Geophysical Research: Space Physics*, *108*(A12), 1417. https://doi.org/10.1029/2002JA009763

Fujita, S., Yamagishi, H., Murata, K. T., Den, M., & Tanaka, T. (2012). A numerical simulation of a negative solar wind impulse: Revisited. *Journal of Geophysical Research: Space Physics*, *117*(A9), 1–12. https://doi.org/10.1029/2012JA017526

Fujita, S., Fujii, I., Endo, A., & Tominaga, H. (2018). *Numerical modeling of spatial profiles of geomagnetically induced electric field intensity in and around Japan*.

Fujita, Shigeru, & Tanaka, T. (2006). Magnetospheric plasma processes during a sudden commencement revealed from a global MHD simulation (pp. 31–50). https://doi.org/10.1029/169GM05

Fujita, Shigeru, & Tanaka, T. (2022). Two current systems in the preliminary phase of sudden commencements in the magnetosphere. *Earth, Planets and Space*, *74*(1), 66. https://doi.org/10.1186/s40623-022-01624-3

Fukushima, N. (1976). Generalized theorem for no ground magnetic effect of vertical currents connected with Pedersen currents in the uniform conductivity ionosphere. *Report of Ionosphere and Space Research in Japan*, *30*, 35–40.

Fukushima, Naoshi. (1971). Electric Current Systems for Polar Substorms and Their Magnetic Effect Below and Above the Ionosphere. *Radio Science*, *6*(2), 269–275. https://doi.org/10.1029/RS006i002p00269

Gjerloev, J. W. (2012). The SuperMAG data processing technique. *Journal of Geophysical Research: Space Physics*, *117*(A9), 1–19. https://doi.org/10.1029/2012JA017683

Gonzalez, W. D., Joselyn, J. A., Kamide, Y., Kroehl, H. W., Rostoker, G., Tsurutani, B. T., & Vasyliunas, V. M. (1994). What is a geomagnetic storm? *Journal of Geophysical Research*, *99*(A4), 5771. https://doi.org/10.1029/93ja02867

Gosling, J. T., Asbridge, J. R., Bame, S. J., Hundhausen, A. J., & Strong, I. B. (1967). Discontinuities in the solar wind associated with sudden geomagnetic impulses and storm commencements. *Journal of Geophysical Research*, *72*(13), 3357–3363. https://doi.org/10.1029/JZ072i013p03357

Groom, R. W., & Bailey, R. C. (1989). Some effects of multiple lateral inhomogeneities in magnetotellurics. *Geophysical Prospecting*, *37*(January), 697–712.

Guo, S. X., Liu, L. G., Pirjola, R. J., Wang, K. R., & Dong, B. (2015). Impact of the EHV Power System on Geomagnetically Induced Currents in the UHV Power System. *IEEE Transactions on Power Delivery*, *30*(5), 2163–2170. https://doi.org/10.1109/TPWRD.2014.2381248

Hajra, R., Tsurutani, B. T., Echer, E., Gonzalez, W. D., & Gjerloev, J. W. (2016). Supersubstorms (SML < −2500 nT): Magnetic storm and solar cycle dependences. *Journal of Geophysical Research: Space Physics*, *121*(8), 7805–7816. https://doi.org/10.1002/2015JA021835

Hori, T., Shinbori, A., Nishitani, N., Kikuchi, T., Fujita, S., Nagatsuma, T., et al. (2012). Evolution of negative SI-induced ionospheric flows observed by SuperDARN King Salmon HF radar. *Journal of Geophysical Research: Space Physics*, *117*(A12), 1–13. https://doi.org/10.1029/2012JA018093

Iijima, T., & Potemra, T. A. (1976). The amplitude distribution of field-aligned currents at northern high latitudes observed by Triad. *Journal of Geophysical Research*, *81*(13), 2165–2174. https://doi.org/10.1029/JA081i013p02165

Itonaga, M., Yoshikawa, A., & Fujita, S. (2000). A wave equation describing the generation of field-aligned current, (1996), 503–507.

Kataoka, R. (2013). Probability of occurrence of extreme magnetic storms. *Space Weather*, *11*(5), 214–218. https://doi.org/10.1002/swe.20044

Kataoka, R., & Miyoshi, Y. (2006). Flux enhancement of radiation belt electrons during geomagnetic storms driven by coronal mass ejections and corotating interaction regions. *Space Weather*, *4*(9), 1–11. https://doi.org/10.1029/2005SW000211

Kataoka, R., & Ngwira, C. (2016). Extreme geomagnetically induced currents. *Progress in Earth and Planetary Science*, *3*(1). https://doi.org/10.1186/s40645-016-0101-x

Keller, K. A., Hesse, M., Kuznetsova, M., Rastätter, L., Moretto, T., Gombosi, T. I., & Dezeeuw, D. L. (2002). Global MHD modeling of the impact of a solar wind pressure change. *Journal of Geophysical Research: Space Physics*, *107*(A7), 1–8. https://doi.org/10.1029/2001JA000060

Kepko, L., McPherron, R. L., Amm, O., Apatenkov, S., Baumjohann, W., Birn, J., et al. (2015). Substorm Current Wedge Revisited. *Space Science Reviews*, *190*(1–4), 1–46. https://doi.org/10.1007/s11214-014-0124-9

Kikuchi, T., Hashimoto, K. K., Tomizawa, I., Ebihara, Y., Nishimura, Y., Araki, T., et al. (2016). Response of the incompressible ionosphere to the compression of the magnetosphere during the geomagnetic sudden commencements. *Journal of Geophysical Research: Space Physics*, *121*(2), 1536–1556. https://doi.org/10.1002/2015JA022166

Kikuchi, Takashi, Araki, T., Hashimoto, K. K., Ebihara, Y., Tanaka, T., Nishimura, Y., et al. (2022). Instantaneous Achievement of the Hall and Pedersen–Cowling Current Circuits in Northern and Southern Hemispheres During the Geomagnetic Sudden Commencement on 12 May 2021. *Frontiers in Astronomy and Space Sciences*, *9*(May), 1–11. https://doi.org/10.3389/fspas.2022.879314

Kivelson, M. G., & Christopher T. Russell. (1995). *Introduction to Space Physics*. Cambridge University Press.

Kotz, S., & Nadarajah, S. (2000). *Extreme Value Distributions: Theory and Applications*. London: Imperial College Press.

Kubota, Y., Kataoka, R., Den, M., Tanaka, T., Nagatsuma, T., & Fujita, S. (2015). Global MHD simulation of magnetospheric response of preliminary impulse to large and sudden enhancement of the solar wind dynamic pressure. *Earth, Planets and Space*, *67*(1), 94. https://doi.org/10.1186/s40623-015-0270-7

Le, G., Slavin, J. A., & Strangeway, R. J. (2010). Space Technology 5 observations of the imbalance of regions 1 and 2 field-aligned currents and its implication to the cross-polar cap Pedersen currents. *Journal of Geophysical Research: Space Physics*, *115*(A7), 1–14. https://doi.org/10.1029/2009JA014979

Lehtinen, M., & Pirjola, R. (1985). Currents produced in earthed conductor networks by geomagnetically-induced electric fields. *Annales Geophysicae*, *3*(4), 479–484.

Lesher, R. L., Byerly, R. T., & Porter, J. W. (1994). Sunburst - A Network of GIC Monitoring Systems. *IEEE Transactions on Power Delivery*, *9*(1), 128–137. https://doi.org/10.1109/61.277687

Liu, C. M., Liu, L. G., & Pirjola, R. (2009). Geomagnetically induced currents in the high-voltage power grid in China. *IEEE Transactions on Power Delivery*, *24*(4), 2368–2374. https://doi.org/10.1109/TPWRD.2009.2028490

Love, J. J., & Swidinsky, A. (2014). Time causal operational estimation of electric fields induced in the Earth's lithosphere during magnetic storms. *Geophysical Research Letters*, *41*(7), 2266–2274. https://doi.org/10.1002/2014GL059568

Lu, M., Nagarajan, H., Yamangil, E., Bent, R., Backhaus, S., & Barnes, A. (2018). Optimal Transmission Line Switching Under Geomagnetic Disturbances. *IEEE Transactions on Power Systems*, *33*(3), 2539–2550. https://doi.org/10.1109/TPWRS.2017.2761178

Madelaire, M., Laundal, K. M., Reistad, J. P., Hatch, S. M., & Ohma, A. (2022). Transient high latitude geomagnetic response to rapid increases in solar wind dynamic pressure. *Frontiers in Astronomy and Space Sciences*, *9*(August), 1–25. https://doi.org/10.3389/fspas.2022.953954

Matsushita, S. (1957). On sudden commencements of magnetic storms at higher latitudes. *Journal of Geophysical Research*, *62*(1), 162–166. https://doi.org/10.1029/JZ062i001p00162

Mayaud, P. N. (1975). Analysis of storm sudden commencements for the years 1868-1967. *Journal of Geophysical Research*, *80*(1), 111–122. https://doi.org/10.1029/ja080i001p00111

McPherron, R. L., Aubry, M. P., Russell, C. T., & Coleman, P. J. (1973). Satellite studies of magnetospheric substorms on August 15, 1968: 4. Ogo 5 magnetic field observations. *Journal of Geophysical Research*, *78*(16), 3068–3078. https://doi.org/10.1029/ja078i016p03068

McPherron, Robert L., & Chu, X. (2018). The Midlatitude Positive Bay Index and the Statistics of Substorm Occurrence. *Journal of Geophysical Research: Space Physics*, *123*(4), 2831–2850. https://doi.org/10.1002/2017JA024766

Meng, C.-I., & Akasofu, S.-I. (1969). A study of polar magnetic substorms: 2. Three-dimensional current system. *Journal of Geophysical Research*, *74*(16), 4035–4053. https://doi.org/10.1029/JA074i016p04035

Molinski, T. S. (2002). Why utilities respect geomagnetically induced currents. *Journal of Atmospheric and Solar-Terrestrial Physics*, *64*(16), 1765–1778. https://doi.org/10.1016/S1364-6826(02)00126-8

Moretto, T., Ridley, A. J., Engebretson, M. J., & Rasmussen, O. (2000). High-latitude ionospheric response to a sudden impulse event during northward IMF conditions. *Journal of Geophysical Research: Space Physics*, *105*(A2), 2521–2531. https://doi.org/10.1029/1999JA900475

Moriña, D., Serra, I., Puig, P., & Corral, Á. (2019). Probability estimation of a Carrington-like geomagnetic storm. *Scientific Reports*, *9*(1), 2393. https://doi.org/10.1038/s41598-019-38918-8

Nakamura, S., Ebihara, Y., Fujita, S., Goto, T., Yamada, N., Watari, S., & Omura, Y. (2018). Time Domain Simulation of Geomagnetically Induced Current (GIC) Flowing in 500-kV Power Grid in Japan Including a Three-Dimensional Ground Inhomogeneity. *Space Weather*, *16*(12), 1946–1959. https://doi.org/10.1029/2018SW002004

NERC. Screening Criterion for Transformer Thermal Impact Assessment Project 2013-03 (Geomagnetic Disturbance Mitigation) TPL-007-1 Transmission System Planned Performance for Geomagnetic Disturbance Events (2016).

Neubauer, F. M. (1980). Nonlinear standing Alfvén wave current system at Io: Theory. *Journal of Geophysical Research: Space Physics*, *85*(A3), 1171–1178. https://doi.org/10.1029/JA085iA03p01171

Newell, P. T., & Gjerloev, J. W. (2011). Evaluation of SuperMAG auroral electrojet indices as indicators of substorms and auroral power. *Journal of Geophysical Research: Space Physics*, *116*(A12), n/a-n/a. https://doi.org/10.1029/2011JA016779

Ngwira, C. M., Pulkkinen, A., Leila Mays, M., Kuznetsova, M. M., Galvin, A. B., Simunac, K., et al. (2013). Simulation of the 23 July 2012 extreme space weather event: What if this extremely rare CME was Earth directed? *Space Weather*, *11*(12), 671–679. https://doi.org/10.1002/2013SW000990

Ngwira, C. M., Sibeck, D., Silveira, M. V.D., Georgiou, M., Weygand, J. M., Nishimura, Y., & Hampton, D. (2018). A Study of Intense Local dB/dt Variations During Two Geomagnetic Storms. *Space Weather*, *16*(6), 676–693. https://doi.org/10.1029/2018SW001911

Nishida, A., & Jacobs, J. A. (1962). World-wide changes in the geomagnetic field. *Journal of Geophysical Research*, *67*(2), 525–540. https://doi.org/10.1029/JZ067i002p00525

Odstrcil, D. (2003). Modeling 3-D solar wind structure. *Advances in Space Research*, *32*(4), 497–506. https://doi.org/10.1016/S0273-1177(03)00332-6

Ogilvie, K. W., Burlaga, L. F., & Wilkerson, T. D. (1968). Plasma observations on Explorer 34. *Journal of Geophysical Research*, *73*(21), 6809–6824. https://doi.org/10.1029/JA073i021p06809

Ohtani, S., Nosé, M., Rostoker, G., Singer, H., Lui, A. T. Y., & Nakamura, M. (2001). Storm-substorm relationship: Contribution of the tail current to Dst. *Journal of Geophysical Research: Space Physics*, *106*(A10), 21199–21209. https://doi.org/10.1029/2000JA000400

Ohtani, Shinichi. (2022). New Insights From the 2003 Halloween Storm Into the Colaba 1600 nT Magnetic Depression During the 1859 Carrington Storm. *Journal of Geophysical Research: Space Physics*, *127*(9), 1–16. https://doi.org/10.1029/2022JA030596

Overbye, T. J., Shetye, K. S., Hutchins, T. R., Qiu, Q., & Weber, J. D. (2013). Power grid sensitivity analysis of geomagnetically induced currents. *IEEE Transactions on Power Systems*, *28*(4), 4821–4828. https://doi.org/10.1109/TPWRS.2013.2274624

Piersanti, M., & Villante, U. (2016). On the discrimination between magnetospheric and ionospheric contributions on the ground manifestation of sudden impulses. *Journal of Geophysical Research: Space Physics*, *121*(7), 6674–6691. https://doi.org/10.1002/2015JA021666

Piersanti, M., Di Matteo, S., Carter, B. A., Currie, J., & D'Angelo, G. (2019). Geoelectric Field Evaluation During the September 2017 Geomagnetic Storm: MA.I.GIC. Model. *Space Weather*, *17*(8), 1241–1256. https://doi.org/10.1029/2019SW002202

Pirjola, R. (2002). Review on the calculation of surface electric and magnetic fields and of geomagnetically induced currents in ground-based technological systems. *Surveys in Geophysics*, *23*(1), 71–90. https://doi.org/10.1023/A:1014816009303

Pulkkinen, A., Bernabeu, E., Eichner, J., Beggan, C., & Thomson, A. W. P. (2012). Generation of 100-year geomagnetically induced current scenarios. *Space Weather*, *10*(4), n/a-n/a. https://doi.org/10.1029/2011SW000750

Pulkkinen, A. A., Pirjola, R., & Viljanen, A. (2007). Determination of ground conductivity and system parameters for optimal modeling of geomagnetically induced current flow in technological systems. *Earth, Planets and Space*, *59*(9), 999–1006. https://doi.org/10.1186/BF03352040

Püthe, C., Manoj, C., & Kuvshinov, A. (2014). Reproducing electric field observations during magnetic storms by means of rigorous 3-D modelling and distortion matrix co-estimation. *Earth, Planets and Space*, *66*(1). https://doi.org/10.1186/s40623-014-0162-2

Samsonov, A. A., & Sibeck, D. G. (2013). Large-scale flow vortices following a magnetospheric sudden impulse. *Journal of Geophysical Research: Space Physics*, *118*(6), 3055–3064. https://doi.org/10.1002/jgra.50329

Samsonov, A. A., Sibeck, D. G., & Imber, J. (2007). MHD simulation for the interaction of an interplanetary shock with the Earth's magnetosphere. *Journal of Geophysical Research: Space Physics*, *112*(A12), 1–9. https://doi.org/10.1029/2007JA012627

Samsonov, A. A., Sibeck, D. G., & Yu, Y. (2010). Transient changes in magnetospheric-ionospheric currents caused by the passage of an interplanetary shock: Northward interplanetary magnetic field case. *Journal of Geophysical Research: Biogeosciences*, *115*(1), 1–12. https://doi.org/10.1029/2009JA014751

Shi, Q. Q., Hartinger, M. D., Angelopoulos, V., Tian, A. M., Fu, S. Y., Zong, Q.-G., et al. (2014). Solar wind pressure pulse-driven magnetospheric vortices and their global consequences. *Journal of Geophysical Research: Space Physics*, *119*(6), 4274–4280. https://doi.org/10.1002/2013JA019551

Al Shidi, Q., Pulkkinen, T., Toth, G., Brenner, A., Zou, S., & Gjerloev, J. (2022). A Large Simulation Set of Geomagnetic Storms—Can Simulations Predict Ground Magnetometer Station Observations of Magnetic Field Perturbations? *Space Weather*, *20*(11). https://doi.org/10.1029/2022SW003049

Shinbori, A., Tsuji, Y., Kikuchi, T., Araki, T., & Watari, S. (2009). Magnetic latitude and local time dependence of the amplitude of geomagnetic sudden commencements. *Journal of Geophysical Research: Space Physics*, *114*(4), 1–14. https://doi.org/10.1029/2008JA013871

Shiota, D., & Kataoka, R. (2016). Magnetohydrodynamic simulation of interplanetary propagation of multiple coronal mass ejections with internal magnetic flux rope (SUSANOO-CME). *Space Weather*, *14*(2), 56–75. https://doi.org/10.1002/2015SW001308

Sibeck, D. G. (1990). A model for the transient magnetospheric response to sudden solar wind dynamic pressure variations. *Journal of Geophysical Research*, *95*(A4), 3755. https://doi.org/10.1029/ja095ia04p03755

Siscoe, G., Crooker, N. U., & Clauer, C. R. (2006). Dst of the Carrington storm of 1859. *Advances in Space Research*, *38*(2), 173–179. https://doi.org/10.1016/j.asr.2005.02.102

Siscoe, G. L., Formisano, V., & Lazarus, A. J. (1968). Relation between geomagnetic sudden impulses and solar wind pressure changes-An experimental investigation. *Journal of Geophysical Research*, *73*(15), 4869–4874. https://doi.org/10.1029/JA073i015p04869

Siscoe, G. L., Crooker, N. U., Erickson, G. M., Sonnerup, B. U. Ö., Siebert, K. D., Weimer, D. R., et al. (2000). Global geometry of magnetospheric currents inferred from MHD simulations (pp. 41–52). https://doi.org/10.1029/GM118p0041

Song, Y. A. N., & Lysak, R. L. (2001). Towards a new paradigm: from a quasi-steady description to a dynamical description of the magnetosphere. *Space Science Reviews*, 273–292. https://doi.org/https://doi.org/10.1023/A:1005288420253

Stauning, P., & Troshichev, O. A. (2008). Polar cap convection and PC index during sudden changes in solar wind dynamic pressure. *Journal of Geophysical Research: Space Physics*, *113*(A8), 227. https://doi.org/10.1029/2007JA012783

Sun, T. R., Wang, C., Zhang, J. J., Pilipenko, V. A., Wang, Y., & Wang, J. Y. (2014). Journal of Geophysical Research : Space Physics The chain response of the magnetospheric and ground magnetic field to interplanetary shocks, 157–165. https://doi.org/10.1002/2014JA020754.Abstract

Takeuchi, T., Araki, T., Luehr, H., Rasmussen, O., Watermann, J., Milling, D. K., et al. (2000). Geomagnetic negative sudden impulse due to a magnetic cloud observed on May 13, 1995. *Journal of Geophysical Research: Space Physics*, *105*(A8), 18835–18846. https://doi.org/10.1029/2000JA900055

Tamao, T. (1964). A HYDROMAGNETIC INTERPRETATION OF GEOMAGNETIC SSC. *Rep. Ionosphere Space Res. Japan.*, *18*, 18–31.

Tanaka, T. (1994). Finite Volume TVD Scheme on an Unstructured Grid System for Three-Dimensional MHD Simulation of Inhomogeneous Systems Including Strong Background Potential Fields. *Journal of Computational Physics*, *111*(2), 381–389. https://doi.org/10.1006/jcph.1994.1071

Tanaka, T. (1995). Generation mechanisms for magnetosphere-ionosphere current systems deduced from a three-dimensional MHD simulation of the solar wind-magnetosphere-ionosphere coupling processes. *Journal of Geophysical Research*, *100*(A7), 12057. https://doi.org/10.1029/95JA00419

Tanaka, T., Ebihara, Y., Watanabe, M., Den, M., Fujita, S., Kikuchi, T., et al. (2017). Global simulation study for the time sequence of events leading to the substorm onset. *Journal of Geophysical Research: Space Physics*, *122*(6), 6210–6239. https://doi.org/10.1002/2017JA024102

Tanaka, T., Ebihara, Y., Watanabe, M., Den, M., Fujita, S., Kikuchi, T., et al. (2020). Reproduction of Ground Magnetic Variations During the SC and the Substorm From the Global Simulation and Biot-Savart's Law. *Journal of Geophysical Research: Space Physics*, *125*(2), 1–15. https://doi.org/10.1029/2019JA027172

Tanaka, Takashi. (2015). Substorm Auroral Dynamics Reproduced by Advanced Global Magnetosphere−Ionosphere (M–I) Coupling Simulation. In *Auroral Dynamics and Space Weather* (pp. 177–190). https://doi.org/10.1002/9781118978719.ch13

Tanskanen, E. I. (2009). A comprehensive high-throughput analysis of substorms observed by IMAGE magnetometer network: Years 1993–2003 examined. *Journal of Geophysical Research: Space Physics*, *114*(A5), n/a-n/a. https://doi.org/10.1029/2008JA013682

Thébault, E., Finlay, C. C., Beggan, C. D., Alken, P., Aubert, J., Barrois, O., et al. (2015). International Geomagnetic Reference Field: the 12th generation. *Earth, Planets and Space*, *67*(1), 79. https://doi.org/10.1186/s40623-015-0228-9

Tian, A. M., Shen, X. C., Shi, Q. Q., Tang, B. B., Nowada, M., Zong, Q. G., & Fu, S. Y. (2016). Dayside magnetospheric and ionospheric responses to solar wind pressure increase: Multispacecraft and ground observations. *Journal of Geophysical Research: Space Physics*, *121*(11), 813–830. https://doi.org/10.1002/2016JA022459

Tsurutani, B. T. (2003). The extreme magnetic storm of 1–2 September 1859. *Journal of Geophysical Research*, *108*(A7), 1268. https://doi.org/10.1029/2002JA009504

Tsurutani, Bruce T., & Lakhina, G. S. (2014). An extreme coronal mass ejection and consequences for the magnetosphere and Earth. *Geophysical Research Letters*, *41*(2), 287–292. https://doi.org/10.1002/2013GL058825

Vasyliunas, V. M. (2011). The largest imaginable magnetic storm. *Journal of Atmospheric and Solar-Terrestrial Physics*, *73*(11–12), 1444–1446. https://doi.org/10.1016/j.jastp.2010.05.012

Viljanen, A., Pulkkinen, A., Amm, O., Pirjola, R., & Korja, T. (2004). Fast computation of the geoelectric field using the method of elementary current systems and planar Earth models. *Annales Geophysicae*, *22*(1), 101–113. https://doi.org/10.5194/angeo-22-101-2004

Walker, A. D. . (2008). Ray Tracing of Magnetohydrodynamic Waves in Geospace Waves in Uniform Media. *URSI Radio Science Bulletin*, *325*(325), 24–35. https://doi.org/10.23919/URSIRSB.2008.7909583

Wang, C., Li, C. X., Huang, Z. H., & Richardson, J. D. (2006). Effect of interplanetary shock strengths and orientations on storm sudden commencement rise times. *Geophysical Research Letters*, *33*(14), L14104. https://doi.org/10.1029/2006GL025966

Watari, S., Nakamura, S., & Ebihara, Y. (2021). Measurement of geomagnetically induced current (GIC) around Tokyo, Japan. *Earth, Planets and Space*, *73*(1), 102. https://doi.org/10.1186/s40623-021-01422-3

Woodroffe, J. R., Morley, S. K., Jordanova, V. K., Henderson, M. G., Cowee, M. M., & Gjerloev, J. G. (2016). The latitudinal variation of geoelectromagnetic disturbances during large (Dst ≤ -100 nT) geomagnetic storms. *Space Weather*, *14*(9), 668–681. https://doi.org/10.1002/2016SW001376

Wright, A. N., & Southwood, D. J. (1987). Stationary Alfvénic structures. *Journal of Geophysical Research: Space Physics*, *92*(A2), 1167–1175. https://doi.org/10.1029/JA092iA02p01167

Yokoyama, N., & Kamide, Y. (1997). Statistical nature of geomagnetic storms. *Journal of Geophysical Research: Space Physics*, *102*(A7), 14215–14222. https://doi.org/10.1029/97JA00903

Yu, Y.-Q., & Ridley, A. J. (2011). Understanding the response of the ionosphere-magnetosphere system to sudden solar wind density increases. *Journal of Geophysical Research: Space Physics*, *116*(A4), n/a-n/a. https://doi.org/10.1029/2010JA015871

Yu, Y., & Ridley, A. J. (2009). The response of the magnetosphere-ionosphere system to a sudden dynamic pressure enhancement under southward IMF conditions. *Annales Geophysicae*, *27*(12), 4391–4407. https://doi.org/10.5194/angeo-27-4391-2009

Yu, Yiqun, & Ridley, A. J. (2008). Validation of the space weather modeling framework using ground-based magnetometers. *Space Weather*, *6*(5), n/a-n/a. https://doi.org/10.1029/2007SW000345

Yu, Yiqun, Ridley, A. J., Welling, D. T., & Tóth, G. (2010). Including gap region field-aligned currents and magnetospheric currents in the MHD calculation of ground-based magnetic field perturbations. *Journal of Geophysical Research: Space Physics*, *115*(8), 1–11. https://doi.org/10.1029/2009JA014869

Yu, Yiqun, Cao, J., Pu, Z., Jordanova, V. K., & Ridley, A. (2022). Meso-Scale Electrodynamic Coupling of the Earth Magnetosphere-Ionosphere System. *Space Science Reviews*, *218*(8). https://doi.org/10.1007/s11214-022-00940-0

Yue, C., Zong, Q. G., Zhang, H., Wang, Y. F., Yuan, C. J., Pu, Z. Y., et al. (2010). Geomagnetic activity triggered by interplanetary shocks. *Journal of Geophysical Research: Space Physics*, *115*(A5), n/a-n/a. https://doi.org/10.1029/2010JA015356

Zhang, J. J., Wang, C., & Tang, B. B. (2012). Modeling geomagnetically induced electric field and currents by combining a global MHD model with a local one-dimensional method. *Space Weather*, *10*(5), n/a-n/a. https://doi.org/10.1029/2012SW000772

Zhang, J. J., Wang, C., & Tang, B. B. (2013). Effect of the solar wind conditions on the ionospheric equivalent. https://doi.org/10.5194/angeo-31-489-2013

Zhang, J. J., Wang, C., Sun, T. R., Liu, C. M., & Wang, K. R. (2015). GIC due to storm sudden commencement in low-latitude high-voltage power network in China: Observation and simulation. *Space Weather*, *13*(10), 643–655. https://doi.org/10.1002/2015SW001263

Zhang, J. J., Yu, Y. Q., Wang, C., Du, D., Wei, D., & Liu, L. G. (2020). Measurements and Simulations of the Geomagnetically Induced Currents in Low-Latitude Power Networks During Geomagnetic Storms. *Space Weather*, *18*(8). https://doi.org/10.1029/2020SW002549

Zhang, T., & Ebihara, Y. (2022). Superposed Epoch Analyses of Geoelectric Field Disturbances in Japan in Response to Different Geomagnetic Activities. *Space Weather*, *20*(5). https://doi.org/10.1029/2021SW002893

Zhang, T., Ebihara, Y., & Tanaka, T. (2023). Nighttime Geomagnetic Response to Jumps of Solar Wind Dynamic Pressure : A Possible Cause of Québec Blackout in March 1989. https://doi.org/10.1029/2023SW003493

Zhou, X., & Tsurutani, B. T. (2001). Interplanetary shock triggering of nightside geomagnetic activity: Substorms, pseudobreakups, and quiescent events. *Journal of Geophysical Research: Space Physics*, *106*(A9), 18957–18967. https://doi.org/10.1029/2000JA003028

Zhou, Y., & Lühr, H. (2022). Initial Response of Nightside Auroral Currents to a Sudden Commencement: Observations of Electrojet and Substorm Onset. *Journal of Geophysical Research: Space Physics*, *127*(4), 1–14. https://doi.org/10.1029/2021JA030050

Zmuda, A. J., & Armstrong, J. C. (1974). The diurnal flow pattern of field-aligned currents. *Journal of Geophysical Research*, *79*(31), 4611–4619. https://doi.org/10.1029/JA079i031p04611

Publication List

Journal Papers

1. Zhang, T., & Ebihara, Y. (2022). Superposed epoch analyses of geoelectric field disturbances in Japan in response to different geomagnetic activities. Space Weather, 20, e2021SW002893. https:// doi.org/10.1029/2021SW002893.

2. Zhang, T., Ebihara, Y., & Tanaka, T. (2023). Nighttime geomagnetic response to jumps of solar wind dynamic pressure: A possible cause of Québec blackout in March 1989. Space Weather, 21, e2023SW003493. https://doi. org/10.1029/2023SW003493.

3. Zhang, T., Ebihara, Y., & Tanaka, T. (2024). Generation of field-aligned currents in response to sudden enhancement of solar wind dynamic pressure. JGR: Space Physics (under review).

Meeting Attendance

1. STE workshop 2021 (447th Symposium on Sustainable Humanosphere), oral presentation (online), GIE responses to magnetic storms and substorms during SC 23 (2021.03.04).

2. JpGU 2021, oral presentation (online), Variations of geoelectric field during geomagnetic storms and substorms (2021.06.05).

3. 1st GIC workshop 2022 (471st Symposium on Sustainable Humanosphere), oral presentation (online), Study on large-amplitude GIEs observed at Kakioka (2022.03.23).

4. ISSS-14 (2022), poster (online), MHD Simulation: responses of ionospheric currents and

ground electric field variations under different solar wind conditions (2022.09.14).

5. SGEPSS 2022, oral presentation (Kanagawa), MHD simulations of responses of ground magnetic field variations under different solar wind conditions and a case study of Quebec blackout (2022.11.04).

6. 2nd GIC workshop 2023 (483rd Symposium on Sustainable Humanosphere), oral presentation (online), Nighttime geomagnetic response to the jump of solar wind dynamic pressure (2023.03.22).

7. JpGU 2023, oral presentation (Chiba), Nighttime geomagnetic response to jumps of solar wind dynamic pressure: A possible cause of Québec blackout in March 1989 (2023.05.25).

8. SGEPSS 2023, oral presentation (Sendai), Nighttime geomagnetic response to jumps of solar wind dynamic pressure: A possible cause of Québec blackout in March 1989 (2023.09.25).

9. RISH KDK symposium 2023 (516th Symposium on Sustainable Humanosphere), oral presentation (online), Nighttime geomagnetic response to solar wind dynamic pressure pulse: A possible cause of Québec blackout in March 1989 (2024.03.05).

10. 3rd GIC workshop 2024 (518th Symposium on Sustainable Humanosphere), invited talk (online), Nighttime geomagnetic response to solar wind dynamic pressure pulse: A possible cause of Québec blackout on 13 March 1989 (2024.03.27).

11. AOGS 2024, oral presentation (Korea), Nighttime Geomagnetic Response to Solar Wind Dynamic Pressure Pulses (2024.06.28).